Investigation on Functionalized Ruthenium-Based Sensitizers to Enhance Performance and Robustness of Dye-Sensitized Solar Cells

PAR

Nuttapol POOTRAKULCHOTE

EPFL

ÉCOLE POLYTECHNIQUE
FÉDÉRALE DE LAUSANNE

Suisse
2012

Abstract

It has been increasingly aware to the world today that reserves of fossil fuels are limited and their use has serious environmental side effects. Encouraged by this realization was the evolution of the use of cleaner alternative energy, among which Dye-sensitized solar cells (DSCs) are potentially attractive candidates for the lower cost of producing devices which convert an abundant amount of energy from the sun into electricity. Dye-sensitizer in DSCs plays a crucial role as the chlorophyll in plants; to harvest solar light and transfer the energy via electron transfer to a suitable material (TiO_2 in this case) to produce electricity.

The topic of interest for this thesis is to further enhance the photovoltaic performance and the robustness of DSCs by tuning the optical properties of the dye-sensitizer (Ruthenium complex, in this case) using several strategies including an extension of the π-conjugation system, an introduction of antenna molecules and a modification of the Ru-complex structure. This work focuses on the DSC device fabrication and photovoltaic characterization in order to investigate more insight into structure-property-device performance relationship.

New benchmarks for high performance DSCs with ruthenium complex sensitizers with π-extension in their ancillary ligands were presented. The overall conversion efficiency of 9.6% and 8.5% have been achieved with Ru-based sensitizer containing ethylenedioxythiophene, using low-volatile electrolyte and solvent-free electrolyte, respectively. The Ru-sensitizer functionalized with hexylthio-bithiophene unit exhibited a conversion efficiency of 9.4% with low-volatile electrolyte. All these devices showed good stability under prolonged light soaking at 60 °C. Extending π-conjugation of the anchoring ligand with thiophene units in monoleptic Ru-sensitizer also yields an impressive conversion efficiency of 6.1% using 3-μm-thin mesoporous TiO_2 film in corporate with low-volatile electrolyte.

DSC devices based on ruthenium sensitizers functionalized with thienothiophene- and EDOT-conjugated bridge, together with carbazole moiety on the ancillary ligands were found efficient with conversion efficiencies of 9.4% and 9.6%, respectively, in presence of a volatile electrolyte. The carbazole-functionalized ruthenium-based DCSs also performed excellently in the stability test using a low-volatile electrolyte.

Furthermore, the Ru-complexes synthesized by click-chemistry in association with triazole-derivative moieties were successfully used as DCS sensitizers. DSC devices sensitized with these dyes provided the overall conversion efficiency close to 10% with volatile electrolyte. Further studies with solvent-free electrolyte showed notable device stability under extending full sunlight intensity at 60 °C.

The results presented here provide a fertile base for further investigation, which will focus on improving the spectral response of ruthenium dye-sensitizer to full sunlight by searching for new strategies to modify the sensitizer with more efficient functional groups. The target is to reach higher conversion efficiency of DSC devices while retaining their stability under standard reporting conditions.

Keywords: Alternative energy, renewable energy, dye-sensitized solar cells, photovoltaics, nanostructure, ruthenium sensitizer, ancillary ligand, anchoring ligand, π-conjugation, thiophene, carbazole, triazole

Résumé

Nous sommes aujourd'hui de plus en plus conscient que nos réserves mondiales de combustibles fossiles s'èpuisent. L'utilisation de ses ressources est limitée et va avoir de graves effets secondaires sur l'environnement. En connaissance de cause il s'agit de se concentrer sur l'utilisation d'énergie alternative. "Les cellules solaires à colorant" (Dye-sensitizted solar cells, DSCs) sont entre autres des candidates potentiellement intéressantes car elles convertissent une quantité abondante de d'énergie solaire en électricité avec un coût de fabrication minime. Le "colorant sensibilisant" (Dye-sensitizer) dans les DSCs joue un rôle crucial, au même titre que la chlorophylle des plantes, pour collecter la lumière solaire et transférer l'énergie à un matériel approprié (TiO_2, en ce cas) pour produire l'électricité.

L'intérêt du sujet de cette thèse est d'améliorer les performances photovoltaïques et la stabilité de DSC en adaptant les propriétés optiques du colorant sensibilisant (complexe de ruthénium (Ru), dans notre cas) par plusieurs stratégies ; une extension du système π-conjugaison, une introduction de molécules d'antenne et une modification de la structure de Ru-complexe. Cette thèse se concentre sur la fabrication et la caractérisation de cellules photovoltaïques, afin d'étudier et de mieux comprendre la relation de structure-propriété.

De nouveaux échantillons de ruthénium complexes-DSCs avec π-extension dans leurs "ligands auxilliaires" (ancillary ligands) ont été testés. Les rendements globaux de 9.6% et 8.5% ont été obtenus avec sensibilisant-Ru contenant le groupe d'éthylènedioxythiophène, en utilisant respectivement un électrolyte faiblement-volatile et un électrolyte sans solvant. Le sensibilisant-Ru fonctionnalisé avec le groupe hexylthio-bithiophène a montré un rendement global de 9.4% avec l'électrolyte faiblement-volatile. Tous les trois appareils ont montré une bonne stabilité à 60 °C sous une lumière solaire. L'extension de π-conjugaison du "ligand d'ancrage" (anchoring ligand) avec des unités thiophènes dans monoleptic sensibilisant-Ru a montré également un rendement global de 6.1% en utilisant une surface de TiO_2 de 3 μm d'épaisseur et avec un électrolyte faiblement-volatile.

Les cellules à colorant de sensibilisant-Ru fonctionnalisés avec le pont de thiénothiophène et EDOT en conjuguant le groupe de carbazole sur ses ligands auxilliaires ont prouvé leur efficacité avec des rendements de 9.4% et 9.6% en présence d'un électrolyte volatile. Les cellules fondées sur le carbazole et l'électrolyte faiblement-volatile ont également réalisé d'excellentes performances lors du test de stabilité à 60 °C.

On a réussi à utiliser les complexes de ruthénium synthétisés par "click-chemistry" en association des derivés de triazole, comme stabilisateurs. Les cellules photovoltaïques fonctionnalisées avec ce complexe ont montré un rendement de près de 10% avec l'électrolyte volatile. D'autres études avec l'électrolyte sans solvant ont montré une stabilité remarquable de ce complexe sous la lumière solaire à 60 °C.

Les résultats présentés ici assurent une base de travail fertile et pleine de promesse vers une recherche plus approfondie, basée sur l'amélioration de la réponse spectrale à la lumière solaire de sensibilisant ruthénium en cherchant de nouvelles stratégies afin de modifier le sensibilisant avec des groupes fonctionnels plus efficaces. L'objectif est d'atteindre un rendement global plus élevé des cellules solaires à colorant, tout en conservant une bonne stablité sous les conditions standards exigés.

Les mots-clés : l'énergie de substitution, l'énergie renouvelable, les cellules solaires à colorant, photovoltaïques, nanostructure, sensibilisant ruthénium, le ligand auxilliaire, le ligand d'ancrage, la π-conjugasion, thiophène, carbazole, triazole

บทคัดย่อ

โลกในปัจจุบันกำลังตื่นตัวเรื่องผลกระทบต่อสิ่งแวดล้อมของการใช้พลังงานจากเชื้อเพลิงถ่านหิน (fossil fuel) และสภาวะขาดแหล่งผลิตพลังงานนี้ที่จะมาถึงในอนาคตอันใกล้ งานเร่งด่วนในขณะนี้คือการหาแหล่งพลังงานทางเลือกอื่นที่สะอาดและใช้ได้ไม่มีวันหมดเพื่อทดแทนเชื้อเพลิงถ่านหิน เซลล์พลังแสงอาทิตย์แบบสีย้อมไวแสง (Dye-sensitized solar cells, DSC) เป็นทางเลือกหนึ่งที่น่าสนใจเนื่องจาก DSC มีต้นทุนการผลิตต่ำเมื่อเทียบกับเซลล์พลังแสงอาทิตย์เชิงพาณิชย์แบบอื่นที่ใช้กันอยู่ในปัจจุบัน สีย้อมไวแสง (Dye-sensitizer) ถือเป็นส่วนประกอบที่สำคัญที่สุดใน DSC เพราะเป็นส่วนที่ดูดซับแสงอาทิตย์เพื่อเปลี่ยนเป็นพลังงานไฟฟ้า เปรียบเสมือนคลอโรฟิลล์ในใบพืชดูดซับแสงแดดเพื่อสร้างอาหารและพลังงานให้กับต้นไม้

งานวิจัยนี้มีวัตถุประสงค์เพื่อเพิ่มประสิทธิภาพเชิงไฟฟ้า (photovoltaic performance) และความเสถียร (robustness) ให้กับ DSC โดยการปรับปรุงคุณสมบัติการดูดซับแสงของสีย้อมไวแสง (ที่มีส่วนประกอบหลักคือสารประกอบเชิงซ้อนของธาตุ ruthenium, Ru) ให้ดีขึ้นด้วยเทคนิคทางเคมีหลายประการ เช่น การเพิ่มหน่วย π-conjugation ในระบบ, การเติมหมู่ฟังก์ชั่น (functional group) ที่ช่วยดูดซับแสง หรือการเปลี่ยนโครงสร้างทางเคมีของสีย้อมไวแสง เป็นต้น งานวิจัยนี้จะมุ่งเน้นเรื่องการประกอบเซลล์ทดสอบที่ใช้สีย้อมดังกล่าว, การทดสอบสมบัติเชิงแสงและเชิงไฟฟ้าของเซลล์ทดสอบ ตลอดจนการวิเคราะห์และสรุปผลของโครงสร้างทางเคมีของสีย้อมไวแสงที่มีต่อสมบัติเชิงแสงและเชิงไฟฟ้าของ Ru-DSC

จากการทดสอบพบว่า Ru-DSC ที่ประกอบขึ้นจากสีย้อมที่เติมหน่วยโมเลกุล ethylenedioxythiophene เข้าไปเชื่อมต่อกับส่วน ancillary ligand ให้ประสิทธิภาพการเปลี่ยนพลังงานแสงอาทิตย์เป็นพลังงานไฟฟ้า (conversion efficiency) สูงถึง 9.6% เมื่อใช้ร่วมกับอิเล็กโทรไลต์ระเหยยาก (low-volatile electrolyte) และ 8.5% เมื่อใช้ร่วมกับอิเล็กโทรไลต์ไม่ระเหย (solvent-free electrolyte) ขณะเดียวกันเซลล์สีย้อมไวแสงที่ปรับปรุงด้วยการเติมหน่วยโมเลกุล hexylthio-bithiophene ให้ประสิทธิภาพ 9.4% เมื่อใช้ร่วมกับอิเล็กโทรไลต์ระเหยยาก ผลการทดสอบระบุว่าเซลล์ทดสอบทั้งสามเซลล์ผ่านการทดสอบความเสถียรในสภาวะแสงจ้า (light soaking) ที่ 60 °C เป็นเวลา 1000 ชั่วโมง นอกจากนี้ยังพบว่าเซลล์ทดสอบ Ru-DSC ที่มีขนาดความหนาของฟิล์ม TiO$_2$ 3 μm และใช้สีย้อมที่เติมหน่วยโมเลกุล thiophene เข้าไปเชื่อมต่อกับส่วน anchoring ligand ให้ประสิทธิภาพ 6.1% เมื่อใช้ร่วมกับอิเล็กโทรไลต์ระเหยยาก

การปรับปรุงโครงสร้างทางเคมีของสีย้อมไวแสงด้วยการเพิ่มหมู่ฟังก์ชั่น carbazole เข้าไปเชื่อมต่อกับส่วน ancillary ligand โดยมีหน่วยโมเลกุล thienothiophene และหน่วยโมเลกุล EDOT เป็นสะพานเชื่อม (conjugated bridge) สามารถทำให้เซลล์ทดสอบที่ย้อมด้วยสีย้อมไวแสงที่ประกอบด้วยสะพานเชื่อมทั้งสองแบบนี้ ให้ประสิทธิภาพสูงถึง 9.4% และ 9.6% ตามลำดับเมื่อใช้ร่วมกับอิเล็กโทรไลต์ระเหยง่าย และเมื่อทดสอบเพิ่มโดยใช้อิเล็กโทรไลต์ระเหยยาก พบว่าเซลล์ทดสอบผ่านการทดสอบในสภาวะแสงจ้าได้ดี

นอกจากนี้ยังได้มีการทดสอบ Ru-DSC ที่ใช้สีย้อมไวแสงที่เพิ่มหมู่ฟังก์ชั่น triazole เข้าไปในโครงสร้าง โมเลกุลหลักด้วยเทคนิคที่เรียกว่า "Click Chemistry" ซึ่งทำได้ทั้ง (1) เพิ่ม triazole เข้าไปเชื่อมต่อกับส่วน ancillary ligand และ (2) เพิ่ม triazole เข้าไปเป็นส่วนหนึ่งของ chelating ligand จากผลการทดสอบพบว่า หมู่ฟังก์ชั่น triazole ให้ประสิทธิภาพแก่เซลล์ทดสอบใกล้เคียง 10% เมื่อใช้ร่วมกับอิเล็กโทรไลต์ระเหยง่าย และเซลล์ทดสอบที่ใช้ร่วมกับอิเล็กโทรไลต์ไม่ระเหยยังสามารถผ่านการทดสอบความเสถียรในสภาวะแสงจ้า ได้ดีอีกด้วย

ผลงานวิจัยนี้ถือเป็นก้าวสำคัญในงานวิจัยเซลล์แสงพลังอาทิตย์แบบสีย้อมไวแสง โดยการมีส่วนร่วมใน การศึกษาแนวทางใหม่เพื่อปรับปรุงโครงสร้างทางเคมีของสารประกอบเชิงซ้อน ruthenium ของสีย้อมให้มี ประสิทธิภาพการดูดซับแสงที่สูงขึ้น อันจะนำไปสู่เป้าหมายหลักคือผลักดันให้ประสิทธิภาพเชิงไฟฟ้าของ DSC เพิ่มสูงมากขึ้น แต่ในขณะเดียวกันยังสามารถรักษาระดับความเสถียรแม้จะทดสอบในสภาวะแสงจ้า หรือใช้งานจริงในสภาวะแสงแดดธรรมชาติ

คำหลัก: พลังงานทางเลือก, พลังงานทดแทน, เซลล์สุริยะ, เซลล์พลังแสงอาทิตย์, วัสดุนาโน, สีย้อมไวแสง, โฟโตโวลตาอิก, รูทีเนียม, ไทโอฟีน, คาร์บาโซล, ไตรอะโซล, ancillary ligand, anchoring ligand, π-conjugation

Contents

Chapter 1

Introduction

1.1   Motivation

As of today, the world population exceeded 7 billion with a growth rate of 1.1% by 2011. [1] The global primary energy demand is projected to expand by almost 60% from 2002 to 2030 with an average increase of 1.7% per year. Demands will reach 16.5 billion tons of oil equivalent (toe) in 2030 compared to 10.3 billion toes in 2002. [2] As one might expect, fossil fuels will continue to dominate global energy use. They will account for around 85% of the increase in world primary demand over 2002–2030. The problem is, fossil fuels are non-renewable. They are limited in supply and will one day be depleted. There is no escaping this conclusion.

Besides, the use of fossil fuels has serious environmental side effects. [3] Burning fossil fuels creates carbon dioxide, the number one greenhouse gas contributing to global warming. Combustion of these fossil fuels is considered to be the largest contributing factor to the release of greenhouse gases into the atmosphere. In the 20th century, the average temperature of Earth rose 1 degree Fahrenheit (1 °F). The impact of global warming on the environment is extensive and affects many areas. Air pollution is also a direct result of the use of fossil fuels, resulting in smog and the degradation of human health and plant growth.

Encouraged by this realization was the evolution of the use of *'cleaner'* alternative sources of energy, among which solar cells are potentially attractive candidates, akin to the fact that the amount of solar energy that reaches the earth every minute is equivalent

to the amount of energy the world's population consumes in a year. [4] The challenge is to effectively convert solar power into electricity by constructing *'solar cell'* converters which exploit the photovoltaic effect existing at semiconductor junctions. The most current commercial solar cells today are silicon-based which deploy solar-energy conversion efficiencies of 18–25%. [5] However, the construction and installation costs of silicon based solar cells are relatively high.

The invention of the *Dye-sensitized solar cells* (DSC) has opened new prospects to overcome this drawback, for its lower cost of producing devices. [6] Over two decades after the first DSC has been introduced, several new areas have been explored in the field of materials development, *i.e.* mesoporous nanocrystalline layers [7–10], scattering layers [11, 12], counter electrodes [13, 14], sensitization strategies [15–17], as well as the concept of using non-volatile electrolytes [18, 19], in order to increase cell efficiency and stability. The fundamental understanding of working principles has been successfully established through agency of electrical and optical modeling and advanced characterization techniques. [20–22] The highest record overall conversion efficiency of 12.3% under standard AM 1.5 G sunlight has been reached by porphyrin-sensitized TiO_2 using Cobalt(II/III)-based electrolyte. [23]

In my country Thailand, the forwarding economic development has resulted in growing electricity consumption by the commercial and residential sectors. Currently, however, the country still relies heavily on imported oil and the threat always exists that oil prices could go skyward. Petroleum products account for about 57% of commercial energy consumption in Thailand. Diesel and gasoline power 72% of transport. Alternative energy sources in coming years especially solar power become desirable, given the country is both sunny and has large areas of land unsuitable for other uses. Toward this direction, DSC is likely to be a "new hope" technology considering its lower investment costs compared to conventional photovoltaic (PV) technologies.

1.2 Basic photovoltaics principles

Photovoltaics (PV), the conversion of sunlight into electrical power, gets its name from the process of converting light (photons) to electricity (voltage), which is called the PV effect. Traditional PV cells or solar cells (first-generation) are made from silicon, are usually p-n junction solar cells, and generally are the most efficient. Second-generation solar cells are called thin-film solar cells because they are made from amorphous silicon or

non-silicon materials such as cadmium telluride (CdTe). Thin film solar cells use layers of semiconductor materials only a few micrometers thick. Third-generation solar cells will be based on nanostructures. An important advantage for nanostructured solar cells is that they can be used to incorporate new physical mechanisms that allow an efficiency greater than that of a one-junction solar cell. Nanostructured solar cells offer several advantages for solar cells including: (1) the ability to exceed a single junction solar cell efficiency by implementing new concepts, (2) the ability to overcome practical limitations in existing devices, such as tailoring the material properties of existing materials or using nanostructures to overcome constraints related to lattice matching, and (3) the potential for low-cost solar cell structures using self-assembled nanostructures. Today, thousands of people power their homes and businesses with individual solar PV systems. Utility companies are also using PV technology for large power stations.

Dye-sensitized solar cells can be considered to be a technology between the second- and the third-generation PV cells. It has the potential to become a third-generation technology utilizing the nanoscale properties of the device as a PV material to convert the sunlight into electrical energy.

1.2.1   Solar energy

As mentioned previously, the amount of solar energy that reaches the earth every minute is equivalent to the amount of energy the world's population consumes in a year. The power density from the sun outside the earth's atmosphere is given by the solar constant 1353 ± 21 W m^{-2}, dropping to approximately 1000 W m^{-2} on average at the earth surface attenuated by absorption in the atmosphere. Figure 1.1 compares the extra-terrestrial solar spectrum; *Air mass* 0 (AM 0) to the standard terrestrial AM 1.5 spectrum, which is used as a standard reference for solar cell efficient measurement.

The Air Mass (AM) is the ratio of the path length of the sun light shining through the atmosphere when the sun is at a given angle θ the zenith, to the path length when the sun is at its zenith. This relation can be approximated by $AM = \frac{1}{cos\theta}$. The standard test condition; AM 1.5G, corresponds to a solar incident angle of 48 degrees relative to the normal surface.

On the other hand, the extraterrestrial solar spectrum (AM 0) can be closely modeled as a 6000 K blackbody spectrum subject to the generalized Planck equation [24] as
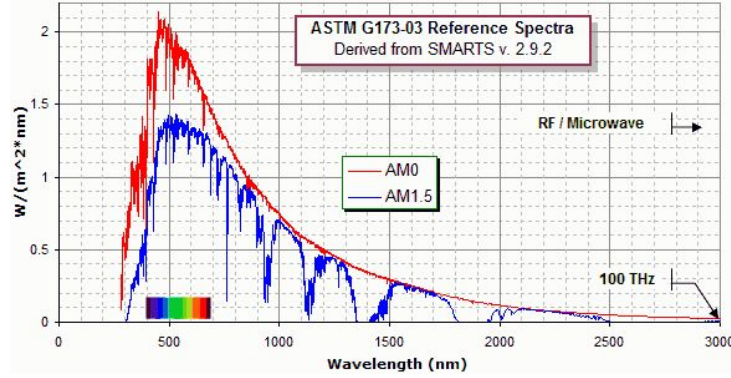
Figure 1.1: The extraterrestrial AM 0 or 6000K blackbody spectrum compared with terrestrial AM 1.5 spectrum.

following:

$$n(E, T, \mu) = \epsilon(E)\, \frac{2\pi}{c^2 h^3}\, \frac{E^2}{\exp\frac{E-\mu}{k_B T} - 1} \tag{1.1}$$

where n is the photon flux as a function of energy E, $\epsilon(E)$ is an energy-dependent emissivity, μ is the photon chemical potential and T is absolute temperature. For a blackbody, $\epsilon = 1$ and $\mu = 0$ for all energy levels. The total energy density from the sun can be obtained by

$$\int_0^\infty E\, n(E, T)\, \mathrm{d}E = \sigma T^4 \,, \tag{1.2}$$

where σ is the Stefan-Boltzman constant ($\sigma = 2\pi^5 k^4 / 15 c^2 h^3 = 5.650400 \times 10^{-8}$ J s^{-1} m^{-2} K^{-4}). When $T = T_{sun} = 6000$K, equation 1.1 describtes the photon flux at the surface of the sun and 1.2 the energy density at the surfact of the sun. On earth we receive sunlight from the solar disc subtending only a fraction of the earth-hemisphere that is visible to the solar cells, thus a dilution factor of $f_\omega = 2.16 \times 10^{-5}$ must be considered in order to calculate the photon flux and energy density on earth. [25]

1.2.2   Semiconductor solar cells

Solar cells are based on the idea of the photovoltaic effect, where an electron can be excited across the band gap by absorbing a single photon of sufficient energy. Figure

1.2a shows the radiative generation process in a semiconductor solar cell. Any incoming photon (1) with an energy E < E_g will not have enough energy to excite an electron across the band gap, the solar cell is transparent to these photons and their energy is wasted. A photon with energy E = E_g (2) will have just enough energy to excite an electron across the band gap and into the conduction band creating an electron-hole pair. A photon with E > E_g (3) will be excited high into the conduction band and will quickly relax back to the band-gap edge via many phonon interactions. The difference in energy between the band gap energy and the photon energy is lost in the form of heat. Figure 1.2b outlines additional losses associated with the recombination of electrons and holes in a semiconductor solar cell. Radiative recombination (4) occurs as an electron in the conduction band drops down across the band gap to the valence band and recombines with a hole, losing energy in the form of an emitted a photon. The *Shockley-Read-Hall* (SRH) recombination (5) occurs when an electron recombines with a hole via defect impurity states in the semiconductor. [26, 27]

(a) Generation   (b) Recombination
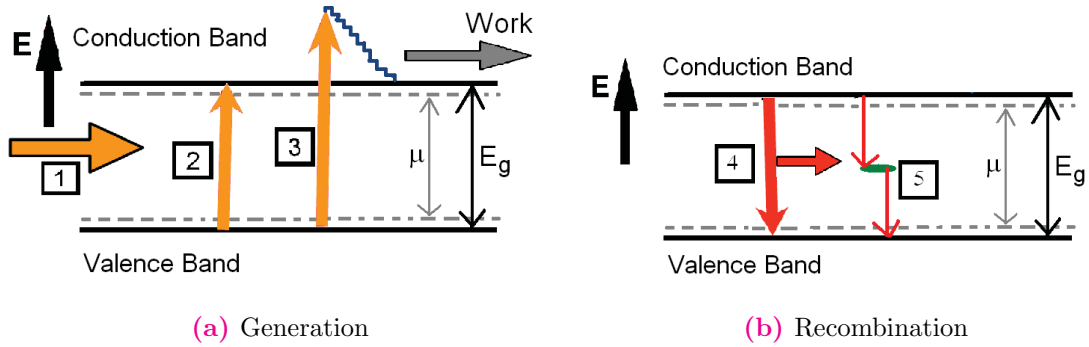
Figure 1.2: An outline of the a) generation and b) radiative recombination processes in a semiconductor solar cell with band gap energy E_g.

Quasi-Fermi levels

A Fermi level describes the electron energy at which 50% occupancy is attained. For an intrinsic semiconductor in equilibrium, the Fermi energy is given by

$$E_f = \frac{E_c + E_v}{2} + \frac{3k_B T}{4} \ln \frac{m_h}{m_e} , \qquad (1.3)$$

where E_c and E_v are the energy levels of the conduction and valence bands respectively, k_B is Boltzmann's constant, T is the temperature and m_h and m_e are the effective masses of the holes and electrons respectively.

At room temperatures and lower the second term is small hence the Fermi energy lies very close to the center of the band gap. When an impurity is introduced to an intrinsic semiconductor the Fermi energy must shift to ensure charge neutrality. When a donor state is introduced with an energy level close to the conduction band (n-type), the Fermi energy will shift towards the conduction band. When a acceptor state is introduced with an energy close to the valence band(p-type), the Fermi energy will shift down towards the valence band.

A single Fermi level is sufficient to describe a solar cell in equilibrium. However when the cell is illuminated and/or a voltage bias is applied it is no longer in equilibrium. *Quasi-Fermi levels* describe the occupancy of the conduction and valence band individually when the electron and hole populations are in respective equilibrium, but not in equilibrium with each other. The dashed lines on figure 1.3 indicate the quasi-Fermi levels of the conduction and valence band with an applied bias V. The separation of the quasi-Fermi levels is μ which is equal to the applied forward bias V at the terminals when E is measured in eV. [24]
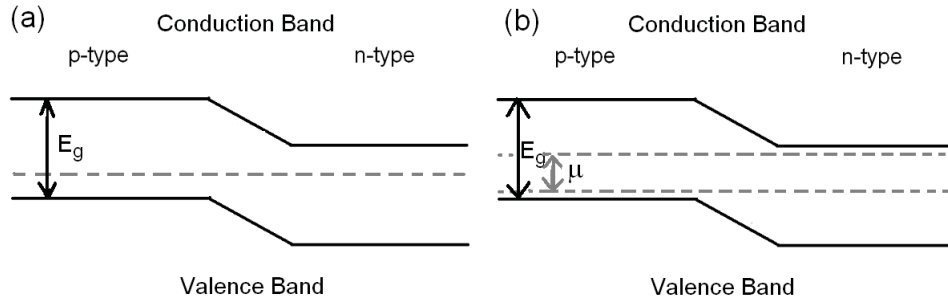
Figure 1.3: Energy levels for a p-n junction; (a) in equilibrium and (b) with an applied bias (V) resulting in a separation of quasi-Fermi levels μ equals to V.

P-n junction solar cell

Semiconductor solar cells require some form of built in asymmetry that will allow useful power to be extracted before electrons and holes recombine. The majority of solar cells consist of a *p-n junction* to allow high carrier mobility and current to only flow in one direction. When there is an abrupt transition from p-type doping to n-type doping the electrons and holes will diffuse to form a region of lower electron and hole concentration

known as the *depletion region.* The depletion region width (w) is given by

$$w^2 = \frac{2\epsilon_s k_B T_{cell}}{e^2} \ln\left[\frac{N_A N_D}{n_i^2}\left(\frac{1}{N_A} + \frac{1}{N_D}\right)\right],\tag{1.4}$$

where ϵ_s is the permittivity of the material, k is Boltzmann's constant, T_{cell} is the temperature of the cell, e is an elementary charge, N_A and N_D are the acceptor and donor densities, respectively (*i.e.* the p-type and n-type doping densities), and n_i is the intrinsic density of states which is given by

$$n_i = \left(\sqrt{N_c N_v}\right) e^{\frac{-E_g}{2k_B T_{cell}}}$$

where $N_c = 2\left(\frac{2\pi m_e^* k_B T_{cell}}{h^2}\right)^{\frac{3}{2}}$ and $N_v = 2\left(\frac{2\pi m_h^* k_B T_{cell}}{h^2}\right)^{\frac{3}{2}}$ are the density of states in the conduction band and the valence band, respectively, E_g is the band gap, m_e^* and m_h^* are the effective electron and hole masses, respectively.

1.2.3 The semiconductor-electrolyte interface

When a semiconductor is placed in contact with an electrolyte, electric current initially flows across the junction until electronic equilibrium is reached, where the Fermi energy of the electrons in the solid (E_F) is equal to the redox potential of the electrolyte (E_{redox}), as shown in the figure 1.4. The transfer of electric charge produces a region on each side of the junction where the charge distribution differs from the bulk material, and this is known as the space-charge layer. On the electrolyte side, this corresponds to the familiar electrolytic double layer, that is, the compact (Helmholtz) layer followed by the diffuse(Gouy-Chapman) layer. On the semiconductor side of the junction the nature of the band bending depends on the position of the Fermi level in the solid. If the Fermi level of the electrode is equal to the flat band potential, there is no excess charge on either side of the junction and the bands are flat (1.4a). If electrons accumulate at the semiconductor side one obtains an accumulation layer (1.4b). If, however, they deplete from the solid into the solution, a depletion layer is formed, leaving behind a positive excess charge formed by immobile ionized donor states (1.4c). Finally, electron depletion can go so far that their concentration at the interface falls below the intrinsic level (1.4d). As a consequence, the semiconductor is p-type at the surface and n-type in the bulk, corresponding to an inversion layer.
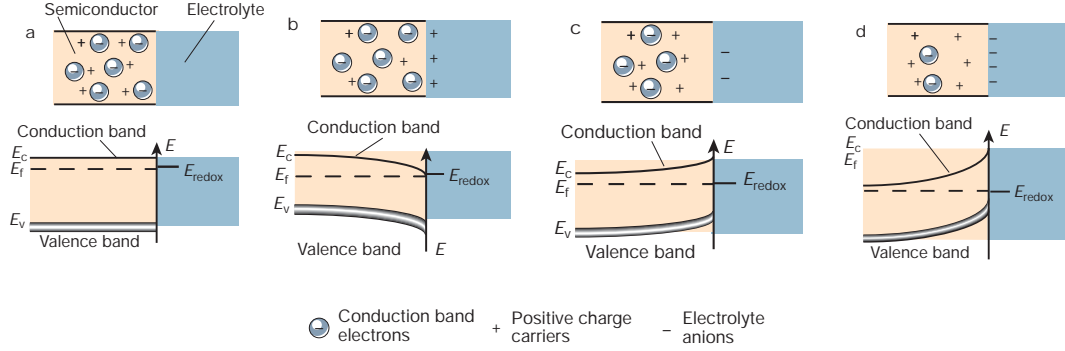
Figure 1.4: Schematic showing the electronic energy levels at the interface between and n-type semiconductor and the electrolyte containing a redox couple.

1.2.4   Electron-hole generation and recombination

The photocurrent generated by the sunlight in a solar cell can be calculated by considering the generalized Planck equation (see equation 1.1). Recall that solar cells cannot be treated as a blackbody thus the generalized Planck equation needs to be modified by including a term describing the absorptivity of the solar cell, $\alpha(E)$ in order to model a "grey body".

$$\int_0^\infty \alpha(E)\, n(E,T,\mu)\, \mathrm{d}E \tag{1.5}$$

As discussed in section 1.2.2, any photon with energy $E < E_g$ will not have enough energy to be absorbed by the solar cell and hence $\alpha(E) = 0$ for $E < E_g$. Assuming the device has a quantum efficiency of 1 for energies $E > E_g$ (*i.e.* 100% of photons with $E > E_g$ will be absorbed by the solar cell), $\alpha(E) = 1$ for $E > E_g$. The chemical potential of a blackbody is $\mu = 0$. Thus, the total number of photons from the sun absorbed by a solar cell per unit area per second will be

$$f_\omega \int_{E_g}^\infty n(E,T_{sun},0)\, \mathrm{d}E \;, \tag{1.6}$$

where f_ω is a dilution factor (see equation 1.2). In an ideal solar cell one photon produces one electron-hole pair, thus equation 1.6 can be multiplied by the elementary

charge (e) to obtain the current density generated in a solar cell,

$$J_{abs}(E) = \frac{2ef_\omega\pi}{c^2h^3} \int_{E_g}^{\infty} \frac{E^2}{\exp\left(\frac{E}{k_BT_{sun}}\right) - 1} \, \mathrm{d}E \; , \tag{1.7}$$

where E is measured in electron-volts (eV). This integral has no easy analytical solution and must be evaluated numerically.

Similarly, the radiative recombination rates can be calculated using a grey body approach. Only photons with energy E > E_g will be emitted from the solar cell as no electronic states exist within the band gap. The emissivity $\alpha(E)$ = 0 for E < E_g and $\alpha(E)$ = 1 for E > E_g. A solar cell will emit radiation over all angles and the intensity is dependant on its temperature T_{cell}. In this case, the chemical potential μ is equal to the applied bias V at terminals (see page 5). The photon flux emitted from a solar cell per unit area is thus given by

$$f_\omega \int_{E_g}^{\infty} n(E, T_{cell}, V) \, \mathrm{d}E \; . \tag{1.8}$$

The current density loss due to electron-hole radiative recombination can be calculated by multiplying equation 1.8 by the charge of an electron,

$$J_{rad}(E, V) = \frac{2e\pi}{c^2h^3} \int_{E_g}^{\infty} \frac{E^2}{\exp\left(\frac{E-V}{k_BT_{cell}}\right) - 1} \, \mathrm{d}E \; . \tag{1.9}$$

1.3 Photovoltaic market overview

Cost-efficiency analysis

Till today, the highest-efficiency solar cells known are crystalline-silicon (c-Si) multi-junction cells based on GaAs and related group III-V materials. These cells are expensive for large-scale applications, but are usually used at the focus of mirrors or lenses that concentrate the solar light by a factor of 50–1000. A multi-junction cell[1] with a large number of cells in the stack can theoretically approach 68.5% efficiency. [28]

However, continuously increasing demand for photovoltaic (PV) modules and the need for low-cost PV options have stretched these advantages to the limits and have exposed some inherent disadvantages of c-Si technology, such as the scarcity of feedstock material, costly processing of materials and device fabrication steps. These, in turn, restrict the potential of Si wafer technology and it appears difficult to achieve PV module production costs below $1/Watt, which is considered essential for cost-competitive generation of solar electricity. The PV module cost depends on the total manufacturing cost of the module per square area and the conversion efficiency. Figure 1.5 gives an estimate of achievable cost with c-Si technology and comparison with projected achievable costs with other PV technologies. It is generally agreed that c-Si technology would not be able to meet the low-cost targets, whereas thin-film and nanostructured technologies have the potential to provide a viable alternative in the near future.

PV market

Surprisingly, the PV market today grows at very high rates (30-40%), similar to that of the telecommunication and computer sectors. World PV production in 2009 increased to 22.9 GW [29] as illustrated in figure 1.6. This became possible owing to technology cost reduction and market development, reflecting the increasing awareness of the versatility, reliability, and economy of PV electric supply systems. Major market segments served by this industry comprise consumer applications, remote industrial systems, developing countries, and grid-connected systems. Of particular interest is the strong differential

---

[1]The multi-junction cell is the stack of p-n junction cells (see page 6) in the order of their band gaps, with the cell with the largest band gap at the top. Light is automatically filtered as it passed through the stack, ensuring that it is absorbed in the cell that can convert it most efficiently.
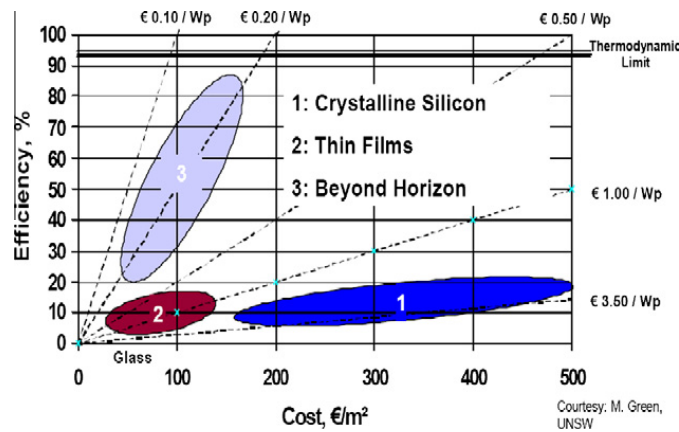
Figure 1.5: Cost versus efficiency analysis for first-generation (1), second-generation (2) and third-generation (3) photovoltaic technologies. Figure courtesy of M. Green/University of New South Wales.

growth rate in rural applications, which now accounts for nearly half of the total PV market. The second largest market is industrial applications.
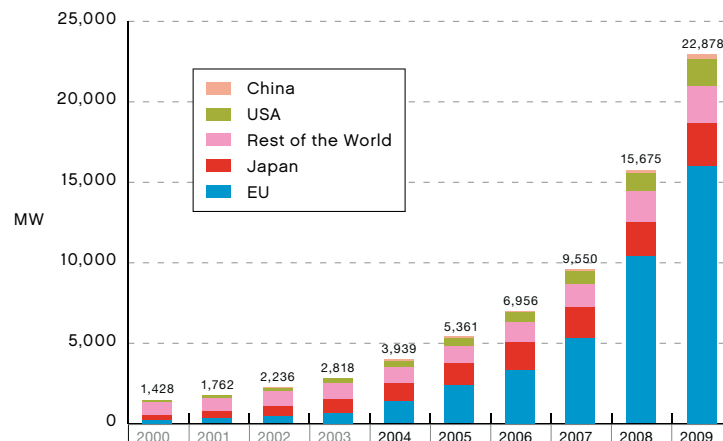
Figure 1.6: Historical development of world cumulative PV power installed in main geographies. [29]

PV applications are progressively finding their markets mainly in the European Union (mostly Germany), Japan, United States and China as shown in figure 1.6 for PV market in 2009. In terms of technology, crystalline silicon (c-Si) and polycrystalline silicon (pc-Si) wafers are the main materials for the world PV industry. [30] At the present, over 80% of the world PV industry is based on c-Si and pc-Si wafer technologies. The CdTe technology is growing sufficiently fast, while thin-film CIGS and amorphous silcon (a-Si) based PV production is still in the beginning stages, despite the remarkable results of R&D many years ago. This may be due to difficulties between laboratory and large-

scale production technologies. Several new multi-megawatt thin-film plants are ready for production of these types of solar cells, and their contribution to the world PV market might be significantly expanded in a near future.

1.4 Dye-sensitized solar cells

Background

Historically, photoelectrochemical cells have been developed as an alternative to the conventional solid-state p-n junction photovoltaics for the conversion of solar energy into electricity. [31, 32] The use of coordination compounds, such as $[Ru(bpy)_3]^{2+}$, as light absorbers, was one of the first approaches to convert low-energy starting materials into high-energy products in homogeneous cells. Semiconductors in mesoporous membrane type film with a high surface area led to an efficient light absorption by attached sensitizers and resulted in intensely colored photoanodes. Solar cells employing such photoanodes presented astonishing results, with photo-response 1000 times higher for the nanostructured electrode. [33, 34] In the early 1990s the development of extremely rough TiO_2 and an efficient sensitizer led to photoelectrochemical solar cells recognized as an efficient device for conversion of solar energy into electricity. [35] In this approach, attached dyes, rather than the semiconductor itself, are the absorbing species. They inject electrons into the semiconductor conduction band upon excitation. These electrons are then collected at a conducting surface, generating photocurrent. As a result of this advance, the development of low-cost, efficient photochemical solar cells became possible.

DSC operating principle

A dye-sensitized solar cell can be considered as a hybrid version of photogalvanic cells and solar cells based on semiconductor electrodes. The cell consists of a dye-coated semiconductor electrode and a counter electrode arranged in a sandwich configuration and the inter-electrode space is filled with an electrolyte containing a redox mediator (A/A^-). In this study, a polypyridine complex of Ruthenium as the dye sensitizer, TiO_2 as the semiconductor and iodide/triiodide as the redox mediator. The key reactions taking place in a dye-sensitized photoelectrochemical solar cell are shown in figure 1.7a.
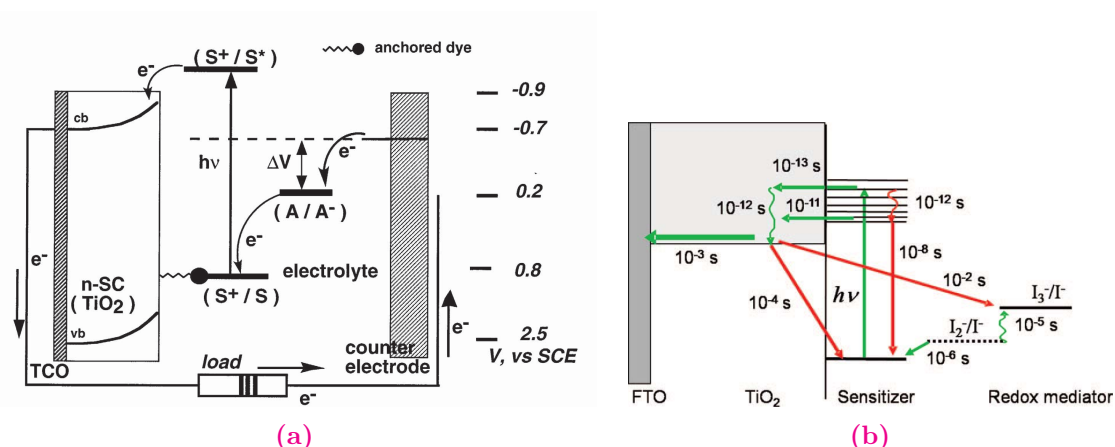
Figure 1.7: a) A schematic of working principle of dye-sensitized electrochemical photo-voltaic cell [36]. b) The kinetic data for the different electron transfer processes taking place at the oxide/dye/electrolyte (TiO$_2$ /Ru-sensitizer/iodide-triiodide) interface for DSC under working conditions (standard 1 sun) [37].

The photoexcitation of the dye sensitizer by visible light forms an electronically excited state that undergoes electron-transfer quenching, injecting electrons into the conduction band of the semiconductor: $S^* \longrightarrow S^+ + e_{cb}^-$. The oxidized dye is subsequently reduced back to the ground state (S) by the electron donor (A$^-$) present in the electrolyte filling the pores: $S^+ + A^- \longrightarrow S + A$. The electrons in the conduction band collect at the back collector electrode and subsequently pass through the external circuit to arrive at the counter electrode where they effect the reverse reaction of the redox mediator: $A + e^- \longrightarrow A^-$ at the counter electrode.

The net effect of visible light irradiation is regeneration of the dye, the redox mediator and the driving of electron through the external circuit. The process thus leads to direct conversion of sunlight to electricity. If above cited reactions alone take place, the solar cell will be stable, delivering photocurrents indefinitely. The maximum obtainable photovolt-age will be the difference between the Fermi level (conduction band) of the semiconductor under illumination and the redox potential of the mediating redox couple.

Different time scale for electron transfer processes

The kinetics of different electron-transfer processes are summarized in figure 1.7b. The electron injection from Ru-sensitizer into the TiO$_2$ conduction band is taken place in femto-seconds up to 150 ps [38], compared with decay of excited state of the dye to the

ground state, which is given by the excited state lifetime of the dye, typically 20–60 ns for Ru-based DSCs [33]. The regeneration of the oxidized dye by the electron donor (iodide in electrolyte, in this study) is in the microsecond time domain. For a turnover number, that is, the cycle life of the sensitizer in the DSC device, to be above 10^8, which is required for a DSC lifetime of 20 years in outdoor conditions, the lifetime of oxidized dye must be >100 s if the regeneration time is 1 μs [39].

The back-electron-transfer process (recombination via dye) from the conduction band of TiO_2 to the oxidized sensitizer occurs on a microsecond to millisecond time scale, due to the electron density in the semiconductor and thus the light intensity. Recombination of electron in TiO_2 via acceptors in electrolyte (triiodide, in this study) is normally referred to as the "*electron lifetime*", which is very long (1-20 ms under 1-sun light intensity) for iodide/triiodide system compared with other redox system used in DSC, explaining the success of this redox couple.

1.5   Ruthenium sensitizer

The use of ruthenium pyridyl complexes as sensitizer in DSC now has more than thirty years of development history. In 1977 Clark and Sutin [40] had already used a tris-bipyridyl ruthenium complex to sensitize titanium dioxide to sub-band gap illumination but in solution only. Charge transfer could only occur after diffusion of the ion to the semiconductor, so the efficiency of the sensitization was very low. By 1980 the idea of chemisorption of the dye through an acid carboxylate group bonding to the metal oxide surface has been established so that the sensitizer was immobilized and it formed the required monomolecular film on the semiconductor substrate which facilitated charge transfer by electron injection. [41] An anatase form of TiO_2 became more dominant as a substrate for the chemisorption of sensitizing dyes for its advantageous photochemical and photoelectrochemical properties, being a low-cost, widely available, nontoxic and biocompatible material, and as such is even used in health care products and domestic applications such as paint pigmentation. The objective had also evolved to concentrate on photovoltaic devices rather than on photosynthesis. In 1991 the remarkable success of sensitized electrochemical solar cell was announced with the conversion efficiency of 7.1% under solar illumination, a synergy of structure substrate roughness, dye photochemistry, counterelectrode kinetics and electrolyte redox chemistry. [42] That improvement has continued progressively since then, now more than 11%. [43]

The choice of ruthenium (Ru) (II) metal is interesting for a number of reasons: (1) its octahedral geometrical structure allows extending of specific ligands in a controlled manner; (2) the photophysical, photochemical and the electrochemical properties of Ru (II) complexes can be tuned in a predictable way; (3) it possesses stable and accessible oxidation states from I to IV; (4) it forms very inert bonds with imine nitrogen centers. [44, 45]

Requirements of the sensitizers

An optimum Ruthenium sensitizers should exhibit an excited-state oxidation potential of at least -0.9V vs. SCE in order to inject electrons efficiently into the TiO_2 conduction band. The ground-state oxidation potential should be about 0.5 V vs. SCE, in order to be regenerated rapidly via electron donation from the electrolyte (iodide/triiodide redox system or a hole conductor). A significant decrease in electron injection efficiencies will occur if the excited- and ground-state redox potentials are lower than these values. Too low LUMO level of sensitizer is not useful for the charge injection into the TiO_2 conduction band can no longer occur. Similarly, too high t_{2g} level (or HOMO, the *highest occupied molecular orbital*) of sensitizer is not useful because it may raise problems associated with regeneration of the sensitizer by electron donation when the HOMO level becomes close to the redox potential of the redox couple. Various ruthenium (II) complexes are primarily employed as sensitizers, with anchoring groups such as carboxylic acid, dihydroxy, and phosphonic acid on the pyridine ligands. [46, 47]

The optimized sensitizer for DSCs should fulfill demanding conditions as follow:

⋆ The excited state of the sensitizer must be higher in energy than the conduction band edge of the semiconductor in order to inject electrons directionally

⋆ The ground state redox potential of the sensitizer should be sufficiently high that it can be regenerated rapidly via electron donation from the electrolyte or a hole conductor

⋆ The molecular extinction coefficient of the sensitizer should be high over the whole absorption spectrum to absorb most of the light

⋆ The sensitizer must be firmly grafted onto the semiconductor oxide surface, and inject electrons into the conduction band with a quantum yield of unity

⋆ The sensitizer should be soluble in some solvent for adsorption on TiO_2 surface and should not be desorbed by the electrolyte solution

⋆ The sensitizer should be stable enough to sustain at least 10^8 redox turnovers under illumination, corresponding to about 20 years of exposure to natural sunlight

Formation of Ru complexes

A formation of Ru complexes can be visualized as an electronic attraction between positive charged metal ion and negative charged ions or the negative ends of the dipoles of neutral ligands. A metal ion or atom can act as a discrete center about which a set of ligands is arranged in a definite way and donates an electron pair to the central metal atom. The number of ligands per metal center is generally either four or six, with others being rare. In an octahedral ligand field, the five degenerate d-orbitals split into degenerate t_{2g} (d_{xy}, d_{xz}, d_{yz}) and e_g $(d_{x^2-y^2}, d_{z^2})$ sets of orbitals. The splitting value increases by 40% as one moves from the first row $(3d)$ to the second $(4d)$ and third $(5d)$ raw transition ions. [48]

The lowest-energy state of Ru-complex is three-fold symmetric and is best described by the symmetry label D_3 as shown in Figure 1.8. Based on the Franck-Condon principle, immediately following excitation the initial excited state ought to possess the same structural symmetry as the ground state. [49] Thus, the initial, Franck-Condon excited state formed via a Metal-to-ligand charge transfer (MLCT) transition[2] in Ru-complex could consist of a delocalized electronic wavefunction on all three bipyridine (bpy) ligands each formally possessing 1/3 of an electronic charge.

An electronic transition from metal t_{2g} orbitals to empty ligand orbitals without spin change allowed, is called a singlet-singlet optical transition. The allowed transitions are identified by large extinction coefficients. The transition with spin change is called singlet-triplet optical transition, which are forbidden and are usually associated with a small extinction coefficient. However, the excited singlet state may also undergo a spin flip, resulting in an excited triplet state. This process is called intersystem crossing (ICS). Demas and colleagues have shown that intersystem crossing to a manifold of relaxed, MLCT

---

[2]The **metal-to-ligand charge transfer (MLCT)** of $d\pi$ coordination compounds have emerged as the most efficient for solar harvesting and sensitization of wide-bandgap semiconductor materials. As the name implies, light absorption promotes an electron from the Metal d orbitals to the Ligand π^* orbitals, $d(\pi) \longrightarrow \pi^*$.
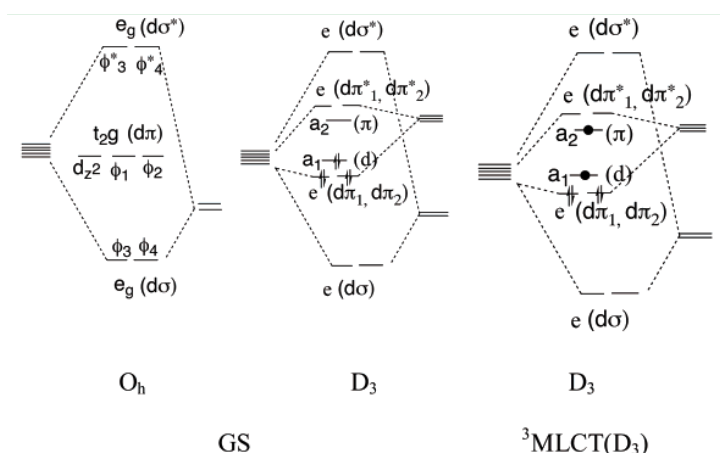
Figure 1.8: Molecular-orbital diagrams for Ru-complexes in their ground state with GS-O_h) octahedral, O_h symmetry; or GS-D_3) reduced D_3 symmetry, like for Ru(bpy)$_3{}^{2+}$. Also shown are excited-state molecular-orbital diagrams for: ^{3}MLCT-D_3) the initial, Franck-Condon excited state formed under the ground-state D_3 symmetry [50].

excited states occurs with a quantum yield near unity in fluid solution as shown in Figure 1.9. [51] Although not formally triplet or singlet in nature, the predominantly triplet character of the lowest-energy excited state and singlet character of the initial Franck-Condon state rationalizes why the transition between them is often termed intersystem crossing.
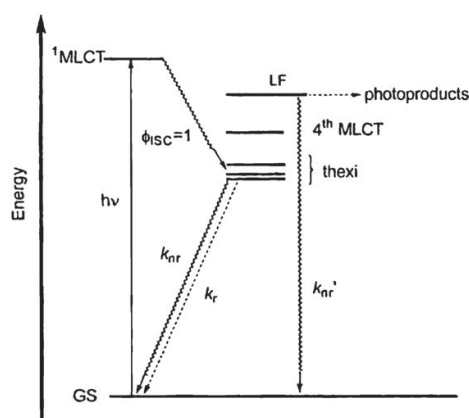
Figure 1.9: A Jablonski-type energy diagram for Ru(bpy)$_3{}^{2+}$ illustrating its manifold of thermally equilibrated excited states, *i.e.* the THEXI-state. The quantum yield for intersystem crossing, ϕ_{ISC}, is approximately unity [52].

To release high energy from excited state, the Ru complexes can undergo either radiative or nonradiative de-excitation. The other potential deactivation pathways are donation of an electron (called oxidative quenching, eq. 1.10) or the capture of electron (reductive quenching, eq. 1.11) or transfer of its energy to other molecules or solvent (eq. 1.12).

$$D^* + Q \quad \rightarrow \quad D^+ + Q^- \tag{1.10}$$

$$D^* + Q \quad \rightarrow \quad D^- + Q^+ \tag{1.11}$$

$$D^* + Q \quad \rightarrow \quad D + Q^* \tag{1.12}$$

Figure 1.10 shows the Lennard-Jones potential energy wells illustrating the relative electronic and vibrational energies and lifetimes for Ru(bpy)$_3$$^{2+}$. The processes include (1) Excitation from the ground-state to the Franck-Condon (FC) state, (2) relaxation of the FC state and fluorescence (520 nm), the lifetime of which is determined by the rate of ISC, ca. <300 fs, (3) to the vibrationally hot ^{3}MLCT state followed by (4) vibrational cooling to the THEXI-^{3}MLCT state (complete by 20 ps), which itself undergoes (5) both non-radiative and radiative relaxation with a lifetime of 400–1000 ns. The lifetime of the ^{1}MLCT excited state of Ru(bpy)$_3$$^{2+}$ was 45 ± 15 fs, which describes the true singlet-to-triplet intersystem crossing to the vibrationally "hot" triplet manifold of states as shown in step 3 of Figure 1.9.
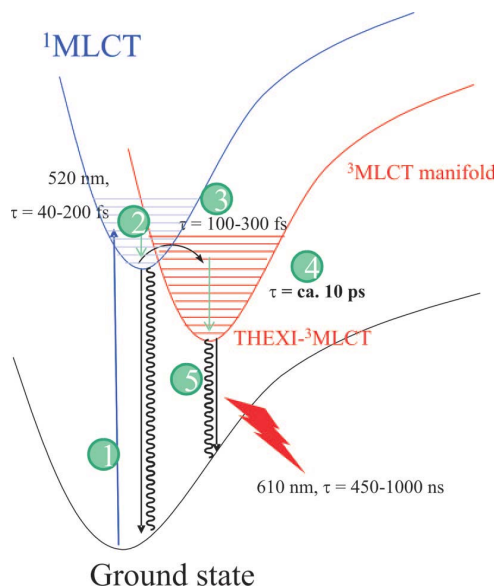
Figure 1.10: Overview of processes following the excitation of Ru(bpy)$_3$$^{2+}$ to the Franck-Condon state [53].

1.6   Thesis objectives

This thesis aims to explore new sensitization strategies to further enhance DSC performance and robustness by obtaining the novelty of Ru-sensitizers with functionalized units that red-shift the spectral response and simultaneously retard the charge recombination between injected electrons from the photo-excited sensitizer into photoelectrode and triiodide present in the electrolyte. Four strategies will be presented in following chapters. In chapter 3, the effect of extending π-conjugation system on the ancillary ligand will be studied through the three novel heteroleptic amphiphilic sensitizers; *i.e.* (a) 3,4-ethylenedioxythiophene unit, (b) hexylthio-bithiophene unit and (c) the combination of hexylthio-bithiophene unit in the ancillary ligand and a vinyl-conjugation in the anchoring ligand.

Furthermore, we will see in chapter 4 the effect of extended conjugation length of anchoring groups by attaching thiophene units on both homoleptic and amphiphilic heteroleptic ruthenium sensitizers. Chapter 5 will discuss the effect of carbazol hole-transport moiety linked to the ancillary ligand by the thienothiophene- and the EDOT-conjugated bridges. In chapter 6, the performance of novel ruthenium sensitizers having their ancillary ligands functionalized with three different triazole derivatives; *i.e.* (a) hexyl-triazolyl group, (b) with hexylphenyl-triazolyl group and (c) with 4-triethyleneglycol-substituted phenyl triazolyl group will be investigated. In addition, chapter 6 will also present the performance of ruthenium sensitizers functionalized with chelating bidentate triazolyl-pyridine ligands. Finally, an in-depth study of optical characteristics of DSC sensitized with the promising dye **B11**, in comparison with **B12** and **Z907** to show the effect of functionalized groups on DSC's optical properties, is discussed in chapter 7.

The primary goal of this research is to provide a base for further investigation on functionalized ruthenium complexes that can be used successfully and effectively as light-absorbing agent for DSCs. In addition, this research assists to gain more insight into the relationships between the ruthenium complex structures, their properties and the photovoltaic performance of DSC devices corresponding to those molecules. The ultimate target is to reach higher conversion efficiency of DSC while retaining their stability under standard reporting conditions.

Bibliography

[1] http://www.census.gov.

[2] International Energy Agency (IEA). World energy outlook, 2004. Paris:OECD/IEA.

[3] Antonio Zecca and Luca Chiari. Fossil–fuel constraints on global warming. *Energy Policy*, 38:1–3, 2010.

[4] http://www.eere.energy.gov/topics/solar.html.

[5] M. A. Green, K. Emery, and W.Warta Y. Hishikawa. Solar cell efficiency tables (version 36). *Progress in Photovoltaics: Research and Applications*, 18:346–352, 2010.

[6] Brian O'Regan and Michael Grätzel. A low-cost, high-efficiency solar cell based on dye-sensitized colloidal films. *Nature*, 353:737, 1991.

[7] M. Späth, P. M. Sommerling, J. A. M. van Roosmalen, et al. Reproducible manufacturing of dye-sensitized solar cells on a semi-automated baseline. *Progress in Photovoltaics: Research and Applications*, 11:207–220, 2003.

[8] K. Tennakone, J. Bandara, P. K. M. Bandaranayake, et al. Enhanced efficiency of a dye-sensitized solar cell made from mgo-coated nanocrystalline SnO_2 . *Japanese Journal of Applied Physics*, 40:L732–L734, 2001.

[9] A. N. M. Green, E. Palomares, S. A Haque, et al. Charge transport versus recombination in dye-sensitized solar cells employing nanocrystalline TiO_2 and SnO_2 films. *Journal of Physical Chemistry B*, 109:12525–12533, 2005.

[10] T. Y. Lee, P. S. Alegaonkar, and J.-B. Yoo. Fabrication of dye sensitized solar cell using TiO_2 coated carbon nanotubes. *Thin Solid Films*, 515:5131–5135, 2007.

[11] S. Hore, P. Nitz, C. Vetter, et al. Scattering spherical voids in nanocrystalline TiO_2 -enhancement of efficiency in dye-sensitized solar cells. *Chemical Communications*, pages 2011–2013, 2005.

[12] S. Hore, C. Vetter, R. Kern, et al. Influence of scattering layers on efficiency of dye-sensitized solar cells. *Solar Energy Materials and Solar Cells*, 90:51176–1188, 2006.

[13] P. J. Li, J. H. Wu, J. M. Lin, et al. Improvement of performance of dye-sensitized solar cells based on electrodeposited-platinum counter electrode. *Electrochimica Acta*, 53:4161–4166, 2008.

[14] T. N. Murakami and M. Grätzel. Counter electrodes for dsc: Application of functional materials as catalysts. *Inorganica Chimica Acta*, 361:572–580, 2008.

[15] P. Wang, S. M. Zakeeruddin, J. E. Moser, et al. Stable new sensitizer with improved light harvesting for nanocrystalline dye-sensitized solar cells. *Advanced Materials*, 16:1806, 2004.

[16] Md. K. Nazeeruddin, C. Klein, P. Liska, and M. Grätzel. Synthesis of novel ruthenium sensitizers and their application in dye-sensitized solar cells. *Coordination Chemistry Reviews*, 249:1460–1467, 2005.

[17] P. Wang, C. Klein, R. H. Baker, et al. A high molar extinction coefficient sensitizer for stable dye-sensitized solar cells. *Journal of the American Chemical Society*, 127:808–890, 2005.

[18] Y. Bai, Y. Cao, J. Zhang, et al. High-performance dye-sensitized solar cells based on solvent-free electrolytes produced from eutectic melts. *Nature Materials*, 7:626, 2008.

[19] D. Shi, Y. Cao, N. Pootrakulchote, et al. New organic sensitizer for stable dye-sensitized solar cells with solvent-free ionic liquid electrolytes. *Journal of Physical Chemistry C*, 112:17478–17485, 2008.

[20] S. A. Haque, E. Palomares, B. M. Cho, et al. Charge separation versus recombination in dye-sensitized nanocrystalline solar cells: the minimization of kinetic redundancy. *Journal of the American Chemical Society*, 127:3456–3462, 2005.

[21] M. Penny, T. Farrel, and C. Please. A mathematical model for interfacial charge transfer at the semiconductor-dye-electrolyte interface of a dye-sensitised solar cell. *Solar Energy Materials and Solar cells*, 92:311–23, 2008.

[22] U. Würfel, J. Wagener, and A. Hinsch. Spatial electron distribution and its origin in the nanoporous TiO_2 network of a dye solar cell. *Journal of Physical Chemistry B*, 109:20444–20448, 2005.

[23] A. Yella, H.-W. Lee, H. N. Tsao, C. Y. Yi, et al. Porphyrin-sensitized solar cells with cobalt (II/III)-based redox electrolyte exceed 12 percent efficiency. *Science*, 334:629, 2011.

[24] P. Würfel. The chemical potential of radiation. *Journal of Physics C: Solid States Physics*, 15:3967–3985, 1982.

[25] Alexis de Vos. *Endoreversible Thermodynamics of Solar Energy Conversion*. Clarendon Press, 1992.

[26] W. Shockley and Jr. W. T. Read. Statistics of the recombinations of holes and electrons. *Physics Reviews*, 87:835–842, 1952.

[27] R. N. Hall. Electron-hole recombination in germanium. *Physics Reviews*, 87:387, 1952.

[28] I. Tobias and A. Luque. Ideal efficiency of monolithic, series-connected multijunction solar cells. *Progress in Photovoltaics: Research and Applications*, 10:323–329, 2002.

[29] European Photovoltaic Industry Association (EPIA). Global market outlook for photovoltaics until 2014, 2010.

[30] Maycock, p.d., 2010. pv news, v.29, n5.

[31] J. S. Connolly. *Photochemical conversion and storage of solar energy Volume 1980*. Academic Press, New York, 1981. and references herein.

[32] M. Grätzel. *Energy resources through photochemistry and catalysis*. Academic Press, New York, 1983. and references herein.

[33] A. Hagfeldt and M. Grätzel. Molecular photovoltaics. *Accounts of Chemical Research*, 33:269–277, 2000.

[34] A. Kay and M. Grätzel. Artificial photosynthesis. 1. Photosensitization of titania solar cells with chlorophyll derivatives and related natural porphyrins. *Journal Physical Chemistry*, 97:6272–6277, 1993.

[35] M. Grätzel. Photoelectrochemical cells. *Nature*, 414:338, 2001.

[36] K. Kalyanasundaram and M. Grätzel. Application of functionalized transition metal complexes in photonics and optoelectronic devices. *Coordination Chemistry Reviews*, 177:347–414, 1998.

[37] A. Hagfeldt, G. Boschloo, L. Sun, et al. Dye-sensitized solar cells. *Chemical Reviews*, 110:6595–6663, 2010.

[38] S. E. Koops, B. C. O'Regan, P. R. F. Barnes, and J. R. Durrant. Parameters influencing the efficiency of electron injection in dye-sensitized solar cells. *Journal of the American Chemical Society*, 131:4808–4818, 2009.

[39] P. Wang, B. Wenger, R. Humphry-Baker, et al. Charge separation and efficient light energy conversion in sensitized mesoscopic solar cells based on binary ionic liquids. *Journal of the American Chemical Society*, 127:6850–6856, 2005.

[40] W. D. K. Clark and N. Sutin. Spectral sensitization of n-type TiO_2 electrodes by polypyridineruthenium(II) complexes. *Journal of the American Chemical Society*, 99:4676, 1977.

[41] M. P. Dare-Edwards, J. B. Goodenough, A. Hamnett, et al. Sensitization of semiconducting electrodes with Ruthenium–based dyes. *Faraday Discussions of the Chemical Society*, 70:285, 1980.

[42] B. O'Regan and M. Grätzel. A low–cost, high–efficiency solar cell based on dye–sensitized colloidal TiO_2 films. *Nature*, 353:737, 1991.

[43] C. Y. Chen, M. Wang, J. Y. Li, N. Pootrakulchote, et al. Highly efficient light-harvesting ruthenium sensitizer for thin-film dye-sensitized solar cells. *ACS Nano*, 3(10):3103, 2009.

[44] J. J. Rack and Harry B. Gray. Spectroscopy and electrochemistry of *mer*-$[RuCl_3(dmso)(tmen)]$. dimethylsulfoxide is sulfur-bonded to Ru(II), Ru(III), and Ru(IV). *Inorganic Chemistry*, 38:2, 1999.

[45] H. Taube. Electron transfer between metal complexes – a retrospective view. *Angewandte Chemie International Edition in English*, 23:329, 1999.

[46] Hyunwoong Park, Eunyoung Bae, Jae-Joon Lee, et al. Effect of the anchoring group in Ru-bipyridyl sensitizers on the photoelectrochemical behavior of dye-sensitized TiO_2 electrodes: carboxylate versus phosphonate linkages. *Journal of Physical Chemistry B*, 110:8740–8749, 2006.

[47] K. Hara, H. Sugihara, Y. Tachibana, et al. Dye-sensitized nanocrystalline TiO_2 solar cells based on Ruthenium (II) phenanthroline complex photosensitizers. *Langmuir*, 17:5992–5999, 2001.

[48] D. M. Roundhill. *Photochemistry and photophysics of metal complexes*. Plenum Press New York and London, 1994.

[49] Edward U. Condon. Nuclear motions associated with electron transitions in diatomic molecules. *Physics Review*, 32:858–872, 1928.

[50] F. Alary, J.-L. Heully, L. Bijeire, et al. Is the ^{3}MLCT the only photoreactive state of polypyridyl complexes? *Inorganic Chemistry*, 46:3154–3165, 2007.

[51] J. N. Demas and D. G. Taylor. On the intersystem crossing yields in Ruthenium(II) and Osmium(II) photosensitizers. *Inorganic Chemistry*, 18:3177–3179, 1979.

[52] Hartmut Yersin and Erich Gallhuber. On the lowest excited states of [Ru(bpy)3](PF6)2 single crystals. *Journal of the American Chemical Society*, 106:6582–6586, 1984.

[53] W. Henry, C. G. Coates, C. Brandy, et al. The early picosecond photophysics of Ru(II) polypyridyl complexes: A tale of two timescales. *Journal of Physical Chemistry A*, 112:4357–4544, 2008.

Chapter 2

Experimental methods

2.1 Materials

2.1.1 Substrates

The substrate of the photoelectrode serves as collector for the photogenerated current and has therefore to be well conducting. It must also form an ohmic contact with the dye-sensitized semiconductor layer, but should show a large overvoltage for reduction of the redox electrolyte in order to minimize the dark current. In this work, highly fluorine-doped transparent conducting oxide (TCO) film deposited on glass plate obtained from either Nippon Sheet Glass, Japan (NSG) or Pilkington (TEC) were used as glass substrates, having parameters as listed in Table 2.1.

Glass code	Resistance ($\Omega/\square$)	T550 (%)[a]	Thickness (mm)
NSG 10	~10	90	4
TEC 7	7	80	3
TEC 15	15	82	2.3

[a]Transmission at 550 nm

Table 2.1: Specific parameters of the conductive glass used for fabricating DSC devices.

2.1.2   Colloidal TiO$_2$ pastes

Two types of TiO$_2$ pastes having nanocrystalline–TiO$_2$ (20 nm) and mricrocrystalline–
TiO$_2$ (400 nm) particles were used respectively as the transparent and the light-scattering
layers of the photoanode. The TiO$_2$ (20 nm) paste was made by adding acetic acid into
titanium iso-propoxide and stirred to achieve a complete hydrolysis reaction. A white
precipitate formed during reaction was heated and peptized in a presence of nitric acid,
then kept stirring in a hot titanium autoclave for colloid to grow hydrothermally. The
colloid was then redispersed by sonication and cencentrated by rotary-evaporator. Ethyl
cellulose and terpineol was then added to the centrifuged and washed material to obtain
a homogeneous paste. Detailed preparation of 20nm particle size TiO$_2$ is mentioned
elsewhere. [1, 2] The TiO$_2$ (400 nm) paste was prepared by CCIC, Japan.

2.1.3   Preparation of mesoporous TiO$_2$ photoanode

The NSG 10 glass (Section 2.1.1) was cleaned with detergent in an ultrasonic bath and
rinsed with water and ethanol, then immersed into a 40 mM aqueous TiCl$_4$ solution
at 70 °C for 30 min to produce a thin compact layer of TiO$_2$ on the FTO surface to
prevent charge recombination via the FTO to the electrolyte in the assembled device.
The colloidal TiO$_2$ paste of 20 nm sized particles was then screen-printed onto the FTO
in consecutive steps using 90T screen (Estal Mono, Schweiz Seidengazefabrik AG Thal),
with an intermediate drying at 125 °C between each screen-printing, to obtain the desired
film thickness (generally between 5–10 μm). In many cases, two additional layers of 400
nm sized particles were screen-printed on the transparent layer to obtain a 4–5 μm thick
scattering layer. The electrodes were gradually heated and sintered at to 500 °C for 15
min to fuse all TiO$_2$ together. The final TiO$_2$ "double layer" was treated again with a
TiCl$_4$ solution. Before using, the TiO$_2$ electrode was sintered at 500 °C for 30 min. After
cooling to about 80 °C, the electrode was immersed into a dye solution for ~ 16 h for
sensitization. The TiO$_2$ films typically had a circular (~0.28 cm²) geometry.

2.1.4   Preparation of counter electrode

Counter electrodes were prepared by thermal decomposition of platinum precursor on
conducting glass either TEC 7 or TEC 15. A little hole was sandblasting-drilled through

the glass in order to fill in the electrolyte during the assembly step. A few drops of 5–10 M hexachloroplatinic (IV) acid hexahydrate (H_2PtCl_6) in anhydrous isopropanol was spread onto the conducting glass surface, dried in air, and heated at ~400 °C for 15 min. The same procedure might be repeated one more time after cooling down the platinized conducting glass for a few minutes to ensure the homogenity of platinum.

2.1.5 Sensitizers

All ruthenium complexes used in this study as well as providers are listed in Appendix A. The compound molecules were received in solid form and all dye-sensitizer solutions were prepared in LPI. In general, the dye solution (0.3 mM) is prepared in a mixed solvent of acetonitrile and *tert*-butyl alcohol (volume ratio 1:1). For sensitizers with high absorption coefficient, 10% of Dimethyl sulfoxide (DMSO) may be added into the solvent for a better solubility.

The molecular structures of each sensitizer were presented in corresponding sections as well as summarized in Appendix A.

2.1.6 Coadsorbents

Cografting of dye sensitizers with amphiphilic molecules containing carboxylate or phosphonate groups have been reported previously to enhance the stability and the efficiency of the DSCs. [3–7] In this study we use three coabsorbents; bis(3,3-dimethylbutyl)phosphonic acid (DINHOP), 4-Guanidinobytyric acid (GBA) and $3\alpha,7\alpha$-dihydroxy-5β-colic acid (Cheno). Figure 2.1 displays molecular structures of these three coadsorbent molecules. If coadsorbent is used in device fabrication, it is added into the dye solution before photoanode sensitization.

DINHOP. DINHOP is one of the amphiphile molecules that contains phosphonic acid as an anchoring group and two neohexyl groups on the other end. When added into the dye solution to sensitize the TiO_2 film, DINHOP binds to titanium ions at the surface of titania via the phosphinate group. The binding is much stronger than that of alphatic carboxylic acids, [8] which is good for the long term stability of DSCs employing phospinates as anchoring groups for coadsorbents or even the sensitizer itself. The two neohexyl groups serve both as insulators and hydrophobic umbrellas protecting the TiO_2 surface from

(a) DINHOP   (b) GBA

(c) Cheno
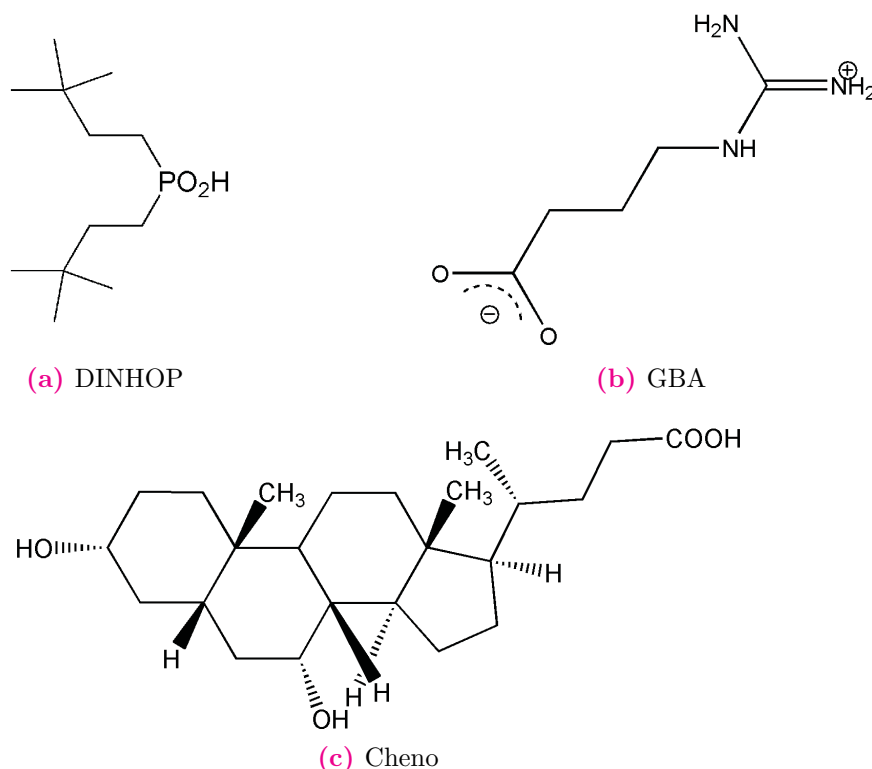
Figure 2.1: Molecular structure of coadsorbents

being approached by water and the oxidized form of the redox mediator. M. Wang and co-workers [8] reported that a presence of DINHOP in as coadsorbent in DSC retards the interfacial electron recombination with triiodide, increases the power output of the DSC devices, as well as shows outstading stability under prolonged light soaking at 60 °C.

GBA. The main effect of GBA-coadsorption is to block the electron recapture by the redox electrolyte, allowing higher electron concentrations in the mesoscopic TiO_2 film and thus a remarkably higher V_{oc} to be reached under illumination without suffering significant current penalty, enhancing the total power conversion efficiency of DSCs. Previous studies [9] revealed that this increase in photovoltage is generated from the negative shift of the quasi-Fermi level $(_nE_F)$ of TiO_2 nanocrystals, as well as the inhibition of charge transfer from electrons in TiO_2 to the triiodide in the electrolyte primarily resulting from the shielding of surface traps due to the addition of GBA as coadsorbent.

Cheno. A. J Frank and co-workers [10] found that the addition of chenodeoxycholate not only shifts the TiO_2 conduction band edge to negative potentials, but also accelerates the rate of recombination. The net effect of these opposing phenomena is to produced a

higher photovoltage. Although the chenodeoxycholate is also found significantly reducing the dye-loading of sensitizers on TiO_2 surface, it has only a modest effect on the short-circuit photocurrent.

2.1.7   Electrolyte

Fundamental electrolytes were prepared by dissolving/mixing different components in the solvent. Based on the volatility of the solvent, electrolytes were classified as: volatile acetonitrile-based electrolyte; non-volatile MPN-based electrolyte; and solvent-free, ionic liquid electrolyte. [11, 12] Detailed composition of electrolytes are listed in Appendix B. The electrolytes used in this work were prepared by Dr. S. M. Zakeeruddin.

2.2   Device fabrication

To fabricate the DSC test device, the sensitized photoanode (Section 2.1.3) was rinsed with acetonitrile and then assembled with the counter electrode (Section 2.1.4). Both glasses were separated by a 25-μm-thick Surlyn hot melt ring (Dupont, USA) and sealed by heating press. The internal space was evacuated and filled with electrolyte (Section 2.1.7) through the little hole by using a vacuum pump. The hole was subsequently sealed by a round Surlyn sheet and covered by a thin glass to avoid the leakage of the electrolyte. Finally, a solder (Cerasolza, Asahi Glass) was applied on each side of the FTO electrodes to reduce the series resistance of the device and ensure a good electrical contact with measurement cables. In general, up to 4 devices were fabricated for each experimental variable change in order to make the opportune statistics. A sketch of DSC device with a picture of finished test device are shown in figure 2.2.

Loss of light reflection from photoanode glass was reduced by applying a self–adhesive fluorinated polymer anti-reflecting film (ARKTOP, Asahi Glass). The film serves simultaneously as UV cut-off filter below 380 nm, which is a critical degradation factor for the stability of DSC. [13] Detailed study of effect of light scattering, $TiCl_4$ treatment and the anti–reflecting film are described somewhere else. [14]
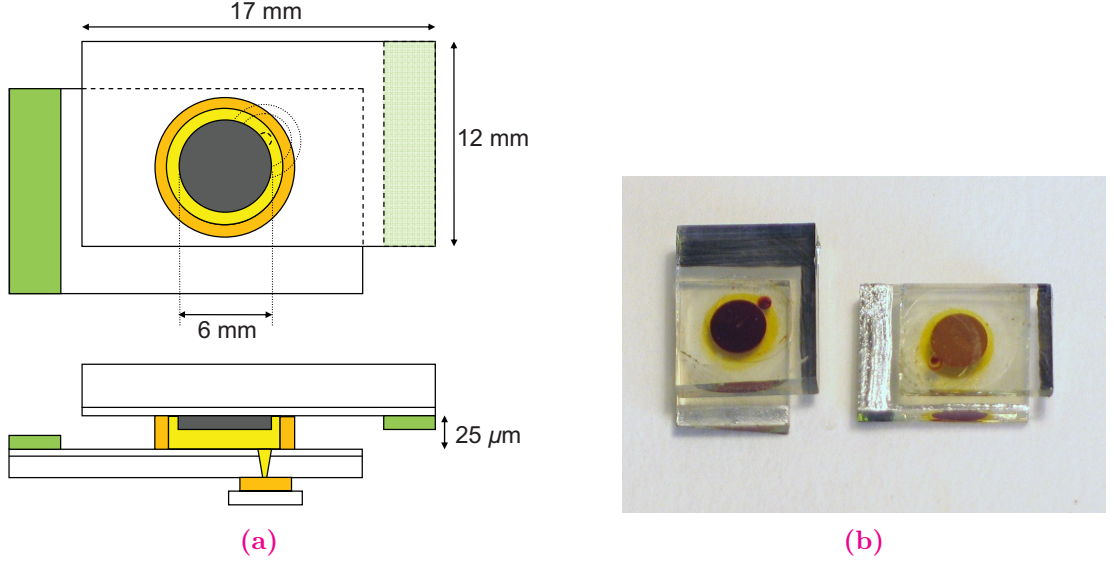
Figure 2.2: A sketch of DSC device and a picture of fabricated ones used for photovoltaic tests

2.3   Measurement and characterization

The basic photovoltaic characteristics of DSC are measured under steady-state conditions where the charge density does not change with time. The rate of photo–generated charges is equivalent to the sum of the rate of charges being transported into the DSC volume element and the rate of charges recombining with redox media in electrolyte.

2.3.1   Current-voltage (J-V) Characterization

J-V Characteristics. Figure 2.3 illustrates an equivalent electric circuit that describes the characteristics of a solar cell. In the dark, the applied voltage bias generates a *dark current* that flows in the direction opposite to that of the photocurrent which is generated under illumination. For an ideal diode, the dark current I_{dark} relates to voltage by

$$I_{dark} = I_s \left(e^{\frac{qV}{k_B T}} - 1 \right), \tag{2.1}$$

where I_s is the saturation current of diode (typically 10^{-7}–10^{-9} A), V is the applied voltage on the terminals of the cell and q is the elementary charge. Under light irradiation,

the photocurrent is generated by

$$I = I_{ph} - I_{dark} = I_{ph} - I_s \left(e^{\frac{qV}{mk_BT}} - 1 \right),$$ (2.2)

where I_{ph} is the photocurrent subject to irradiation intensity. An ideality factor, m, is added to the numerator term to describe the weaker dependence of dark current on voltage in case of non-ideal devices ($m = 1$ for an ideal device). A shunt resistance R_{shunt} may arise from charge recombination in the photoactive layer and induce a shunting current I_{shunt}. From Figure 2.3, the series resistance R_{series} includes the contact resistance at interfaces, the bulk resistance, and the sheet resistance of the transparent electrodes. The total measured current becomes

$$I = I_{ph} - I_{dark} - I_{shunt} = I_{ph} - I_s \left(e^{\frac{V}{mk_BT}} - 1 \right) - \frac{V + IR_{series}}{R_{shunt}},$$ (2.3)
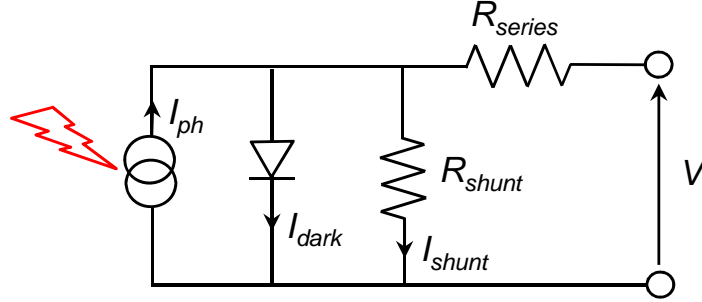
Figure 2.3: An electrical circuit equivalent to a solar cell.

The *Open-circuit voltage* (V_{oc}) is measured when the circuit is broken or no external load is connected. Under this condition, there is no external current flows between the two terminals *i.e.* $I = 0$ and $V = V_{oc}$. If we neglect the shunt and series resistances ($R_{shunt} \to \infty$ and $R_{series} \to \infty$), from equation 2.3 we obtain

$$I_{ph} = I_s \left(e^{\frac{V}{mk_BT}} - 1 \right),$$

or

$$V_{oc} = \frac{mk_BT}{q} \ln \left(\frac{I_{ph}}{I_s} + 1 \right) \cong \frac{mk_BT}{q} \ln \left(\frac{I_{ph}}{I_s} \right) \qquad \text{at} \quad I = 0.$$ (2.4)

Note that V_{oc} increases logarithmically with photocurrent and light intensity.

The *short-circuit current* (I_{sc}) is measured under condition when the applied voltage is zero. Again from equation 2.3 we obtain

$$I_{sc} = I_{ph} \qquad \text{at} \quad V = 0, \tag{2.5}$$

which increases linearly with the light intensity.

A typical J-V curve of a solar cell is shown in Figure 2.4. By convention, the applied bias voltage is positive, and the measured solar cell measurement is negative.
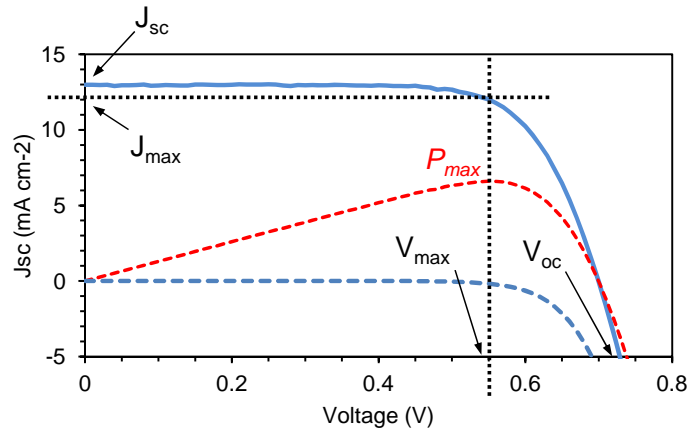
Figure 2.4: A typical J-V curve under illumination (solid blue line) and in the dark (dash blue line). The red line is a power curve indicates the P_m and corresponding J_m and V_m.

The *solar to electric power conversion efficiency* (η); the key performance of a solar cell device, is the percentage of power converted from absorbed light to electrical energy and collected, when DSC device is connected to an electrical circuit. To simplify the measurement, a *Fill factor (FF)* is defined as

$$FF = \frac{V_m J_m}{J_{sc} V_{oc}}, \tag{2.6}$$

where J_{sc} is the integral photocurrent density, V_{oc} is the open-circuit photovoltage. Typically, Fill factor of DSC ranges from 0.6 to 0.8 subject to a device. The FF value depends also on the shunt and series resistances. A high performance solar cell requires

a minimum R_{series} but maximum R_{shunt} in order to maximize FF.

Finally, the solar to electric power conversion efficiency (η) is calculated from the ratio of the maximum extractable power point $P_m = V_m J_m$ to the incident solar power (P_{in}), *i.e.*

$$\eta = \frac{P_m}{P_{in}} = \frac{V_m I_m}{P_{in}} = \frac{J_{sc} V_{oc} FF}{P_{in}} \tag{2.7}$$

Measurement setup. The DSC device (Figure 2.2) was measured at standard test condition with the incident light given by a solar simulator (100 mW/cm²) using 450W Xenon lamp (LOT Oriel, USA) which is matched to the AM 1.5G sunlight irradiation (see section 1.2.1). The spectral output of the Xenon lamp was calibrated with a reference silicon photodiode equipped with an IR cut-off filter (Schott K113, Texpax Sunlight Filter, Präzisions Glas & Optik GmbH, Germany) to reduce the mismatch in the region of 350–750 nm between the simulated and the natural solar spectrum. The current and voltage were measured and controlled by a Keithley 2400 digital source meter (Keithley, USA). The incident light intensity was varied by wavelength-neutral wire mesh attenuators. In most cases, the measurements have been done under dark condition, with 10% attenuated, 50% attenuated, and a full light intensity for each device. A metal mask having an aperture of 0.159 cm² was applied onto the DSC device in order to specify an exact illuminating area.

2.3.2   Incident photon-to-current conversion efficiency (IPCE)

The Incident Photon to Current Conversion Efficiency (IPCE), also known as an External Quantum Efficiency (EQE), is one of the key parameters of quantitative characterization of the solar cell performance for the fact that IPCE shows the spectral response of solar cells to various incident wavelengths. IPCE is defined as a ratio of photoelectrons ($N_{electron}$) to incident photons (N_{photon}), or

$$IPCE = \frac{N_{electron}}{N_{photon}} = \frac{q\frac{N_{electron}}{s}}{q\frac{N_{photon}}{s}} = \frac{I_{ph}\,[amp]}{q\frac{N_{photon}}{s}}. \tag{2.8}$$

On the other hand, the incident power [in unit of Watt] can be derived as

$$P_{in}[Watt] \rightarrow P_{in}\left[\frac{Joule}{s}\right] = \frac{N_{photon}}{s}\,h\,\upsilon = \frac{N_{photon}}{s}\,\frac{hc_0}{\lambda}, \tag{2.9}$$

where h is Planck's constant and c_0 is the speed of light. Combining equation 2.8 and equation 2.9, we obtain

$$
\begin{aligned}
IPCE(\lambda) &= \frac{I_{ph}\,[amp]}{qP_{in}\,\frac{\lambda}{h\,c_0}} \\[2mm]
&= \frac{I_{ph}}{P_{in}} \cdot \frac{hc_0}{q} \cdot \frac{1}{\lambda} \\[2mm]
&= \frac{I_{ph}}{P_{in}} \cdot \frac{1240}{\lambda\,(nm)} \cdot 100\%.
\end{aligned}
\tag{2.10}
$$

We can also determine the short-circuit current density (J_{sc}) of the test device from any given incident photon flux $\phi(\lambda)$ in unit of [m^{-2} nm^{-1} s^{-1}] by

$$J_{sc} = \int q\ IPCE(\lambda)\ \phi(\lambda)\ \mathrm{d}\lambda, \tag{2.11}$$

where q is an elementary charge.

IPCE can be expressed into a product of three components [15, 16] *i.e.* (1) the light harvesting efficiency, LHE(λ), for photons of at a given wavelength (λ), which depends on the spectral and photophysical properties of the sensitizers, (2) the quantum yield, ϕ_{inj}, for electron injection from the excited state sensitizer to the conduction band of TiO$_2$, which depends on the redox potential and the electron recombination lifetime, and (3) the electron collection efficiency, η_{coll}, which depends on the structure and morphology of TiO$_2$ layer.

Measurement setup. An incident light for IPCE measurement is given by a 300 W Xenon arc lamp (ILC Technology) and is modulated with a chopper at frequency 1–4 Hz, then is focused through a Gemini-180 double monochromator (Jobin Yvon Ltd., UK). Before measuring, the monochromatic incident light having an intensity ~ 0.1 mW cm^{-2}

(0.1% sun) is calibrated using a silicon photodiode in order to match the spectral response to those of absorption spectra of the sensitizers. The DSC device (Figure 2.2) with a metal mask having a circular aperture of 0.159 cm² was exposed to this monochromatic light for measurement. The photocurrent generated by the light is measured under short-circuit condition with a lock-in amplier (SR 830, Standford Research Systems). In most cases, an additional DC white light bias from light-emitting diodes with an intensity of 1–100 mW cm⁻² is applied to ensure a linear spectral response of the testing devices.

2.3.3   Photovoltage and Photocurrent Transient Spectroscopy

Electron transport through the TiO_2 film of DSC continues to be the subject of intense debate for the fact that the photocurrent response is surprisingly slow, with rise times ranging from milliseconds to seconds depending on light intensity. The transport is believed to be driven by the concentration gradient of electrons in the conduction band of the TiO_2 film[1]. There are various kinetic processes involved; *e.g.* electron injection, electron recombination and sensitizer regeneration, which take place at different time scales (millisecond to second time range). To characterize this individual time-dependent processes of DSC device, the phototransient spectroscopy is applied.

Most data on electron transport has been interpreted using the multiple trapping (MT) model [18], where the motion of photo-injected electrons through a well defined conduction band with minimum energy E_C is interrupted by a series of trapping and detrapping events. A large concentration of trap states exists within the TiO_2 film [19] and these traps are filled under illumination up to quasi-Fermi level energy $(_nE_F)$. The position of $_nE_F$ relative to the redox level $(E_{F,redox})$ is determined by the conduction-band electron density n_c in terms of the thermal energy k_BT where k_B is the Boltzmann constant and T the absolute temperature by

$$_nE_F - E_{F,redox} = k_BT \ln\left(\frac{n_c}{n_{c0}}\right), \tag{2.12}$$

where n_{c0} is the value of n_c when $_nE_F = E_{F,redox}$, *i.e.* in the dark. Thus, the traps fill as the illumination intensity increases. The detrapping time τ_d from a trap of energy E_T depends exponentially on how far the trap level is below the conduction band, so the

---

[1]Based on the assumption that the electrical field in the bulk of the nanostructure electrode is negligible as a consequence of screening effect by the high ionic strength electrolyte [17]

further $_nE_F$ is from the conduction band, the longer the electron take to detrap and the slower the transport. Thus τ_d relates closely to n_c.

The concept of phototransient measurement is to apply a light perturbation of small amplitude onto a test device under various light biases and probe its voltage and current decay kinetics to characterize the n_c in the TiO_2 film. Light bias with strong intensity generates a lot of charges in TiO_2 film, causing the $_nE_F$ level lies close to the TiO_2 conduction band and all trap states below $_nE_F$ are filled. The τ_d is small. However, at low light bias intensity, only little charge is transported into TiO_2 and the $_nE_F$ level lies far from the conduction band (*i.e.* close to redox energy level). The τ_d in this case is large, the measured recombination and transport rates are low.

Experimental data from the charge extraction techniques [20] has shown that the trap energy distribution (also known as *Density of State* (DOS) distribution) at given energy E is of the form

$$\frac{\partial n_t}{\partial E} = g(E) = \frac{N_{t,0}}{k_B T_0} \exp\left(\frac{E - E_C}{k_B T_0}\right), \tag{2.13}$$

where $N_{t,0}$ is the total density of trapped states per unit volume[2]. T_0 (in unit of temperature) is the characteristic parameter that reflects the width of the trap energy distribution function below the edge of TiO_2 conduction band (E_C). A high value of T_0 implies a broad DOS. Equation 2.13 suggests that tailing from the conduction-band electron states, the density of the traps are high for states that energetically locate near the conduction band and low for deep traps locating far away.

The total density of trapped electrons (n_t) is obtained by integrating $g(E)$ between the limits $E = E_{F,redox}$ and E_C;

$$n_t = \int_{E_{F,redox}}^{E_C} g(E)\, f(E)\, \mathrm{d}E \,, \tag{2.14}$$

where $f(E)$ is the Fermi-Dirac distribution function of energy level E at finite tem-

---

[2]Only surface trap state is considered in this study. [21]

perature T which is defined as [18, 22]

$$f(E) = \frac{1}{1 + \exp\left(\frac{E -_n E_F}{k_B T}\right)} \ , \tag{2.15}$$

Because the density of trapped electrons (n_t) in the TiO$_2$ medium is much larger than that of free electron (n_c) present in the conduction band when $E_C -_n E_F \gg k_B T$, the total electron density n_{total} ($n_{total} = n_c + n_t$) is essentially equal to n_t. [23]

Experimentally, the total charge density n_T in the TiO$_2$ film during the flash light perturbation is probed by the charge extraction technique. [24] In brief, the test device is set to short-circuit in the dark and then switched to open-circuit by the same time the white light bias is turned on for various time delays (100 μs – 1 s). Electrons are photoinjected from excited stated sensitizer to TiO$_2$ film during the illumination. The light bias is subsequently shut off and the decay of photovoltage due to recombination process is recorded. The voltage decay carries on until the controller switches back to short-circuit condition and the number of photoinjected electrons is measured. The charge extraction process is repeated by varying the time delay to obtain the extracted charge as a function of the open-circuit voltage (V_{oc}). Thus, the n_T is obtained by

$$n_T = \frac{\triangle Q}{e\, d\, (1 - p)} \ , \tag{2.16}$$

where $\triangle Q$ is the number of photoinjected electrons per active surface area (in unit of C cm^{-2}) which is determined by integrating the photocurrent transient at short-circuit generated by the perturbation flash light, d the TiO$_2$ film thickness, p the film porosity and e an elementary charge.

As the transient voltage decay follows a pseudo single exponential form with time delay, the *electron lifetime* τ_n can be extracted from an exponential of the form

$$V(t) = V_0 - A_0 \exp\left(-\frac{t - t_0}{\tau_n}\right) \ , \tag{2.17}$$

where V_0, A_0 and t_0 are fitting coefficients. The *recombination rate constant*, k_{rec} is related to the electron lifetime as $k_{rec} = \tau_n^{-1}$. Similarly, one can measure the transient current decay and extract the τ_c from an analogous exponential form similar to equation 2.17. The lifetime τ_c depends on both recombination rate constant (k_{rec}) and *transport rate*

constant, k_{trans}, at the quasi-Fermi level fixed by the white light bias, $\tau_c^{-1} = k_c = k_{trans} + k_{rec}$. An *effective diffusion coefficient*, D_{eff}, can thus determined from the relationship [25]

$$D_{eff} = \frac{d^2 \, k_{trans}}{2.47} \, , \tag{2.18}$$

where d is the TiO$_2$ film thickness.

Finally, an effective diffusion length L_{eff} is given by

$$L_{eff} = \sqrt{\frac{D_{eff}}{k_{rec}}} \, . \tag{2.19}$$

Measurement setup. The transient response of the DSC device (Figure 2.2) is measured both galvanostatically and potentiostatically as a function of white light steady-state bias at various intensities and a superimposed small red light perturbation pulse is provided by light-emitting diodes (LEDs) controlled by Keithley 2602 source meter with a 40 μs response time. The transient current decay is measured at short-circuit under variable applied voltage bias (potentiostatic mode). The transient voltage decay is achieved at open-circuit using a measured applied voltage driven by an applied bias current (galvano-static mode). The perturbation light source was set to an appropriate low level for the voltage decay kinetics to be monoexponential ($\sim$ 0.05 s square pulse width, 100 ns rise and fall time).

2.3.4   Electrochemical Impedance Spectroscopy (EIS)

The EIS measurement is another technique to measure the current response to the application of an AC voltage as a function of the frequency. [26] An important advantage of EIS over other techniques is the possibility to apply an AC voltage with small amplitudes to perturb the systems. To measure EIS, the test device is perturbed an external potential bias with a harmonically modolated small-amplitude voltage, $\triangle U = U_A \, e^{i\omega t}$. An small voltage perturbation causes a current flow $\triangle I = I_A \, e^{i(\omega t - \theta)}$ with a phase delay by angle θ. The impedance of the device is given by

$$Z = \left| \frac{\triangle U}{\triangle I} \right| = \left| \frac{U_A}{I_A} \right| e^{i\theta} \tag{2.20}$$

An equivalent circuit elements used to fit the impedance measurement is shown in Figure 2.5. [27, 28] Note that R_s is the series resistance, R_{TCO} and C_{TCO} are the charge-transfer resistance, for the reduction of tri-iodide at the uncovered part of the FTO and the corresponding electrolytic double-layer capacitance, R_{CO} and C_{CO} are the resistance and the interface capacitance at the FTO-TiO$_2$ contact, Z_w is the Nernst diffusion (Warburg) impedance of the redox species, and R_{CE} and C_{CE} are the charge-transfer resistance and capacitance at the counter electrode/redox electrolyte interface, R_t is electron transfer through TiO$_2$ film, R_{ct} are charge transfer resistance related to TiO$_2$ /redox electrolyte interface recombination, and C_μ is the total capacitance of the nanoparticles. [29, 30]
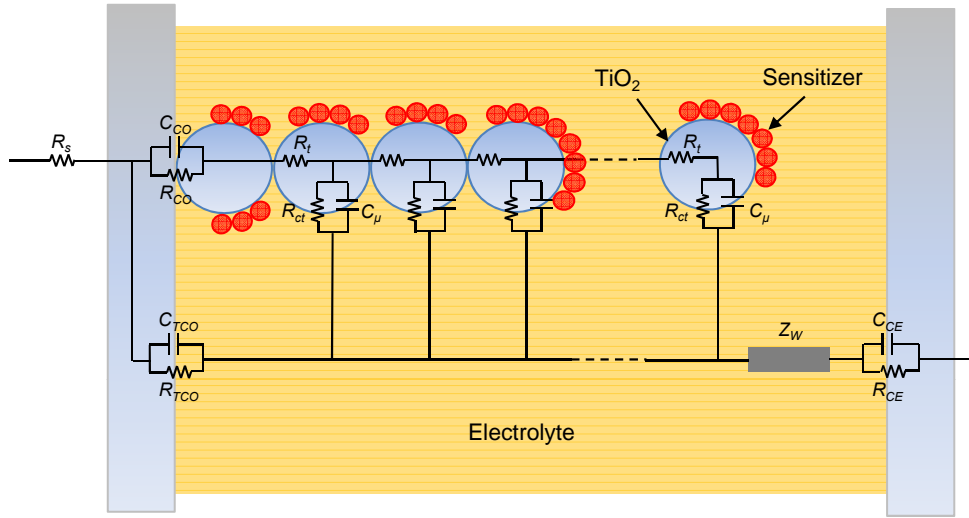
Figure 2.5: An Equivalent circuit for fitting the impedance measurement on the DSC.

When a small forward bias is applied, electrons are injected from FTO into the TiO$_2$ film (characterized by R_{CTO} and C_{CTO}) and then transferred to adjacent particles with a resistance of R_t. Some of these electrons recombine with the oxidized species in electrolyte which is characterized by R_{ct} and C_μ. The R_{CTO} is usually large due to the irreversibility of iodide/tri-iodide redox couple on FTO glass. The diffusion of Iodide ions is described by a Warburg impedance (Z_w). Regeneration of iodide ions at the counter electrode is characterized by R_{CE} and C_{CE}.

The experimental data are fitted empirically to obtain characteristic parameters of the test device *i.e.* R_t, R_{ct} and C_μ. From these parameters, the *electron lifetime* (τ_n), the *diffusion coefficient* (D_n) and *electron diffusion length* (L_n) can be calculated by

$$\tau_n \;\; = \;\; R_{ct}\,C_\mu \;, \tag{2.21}$$

$$D_n \;\; = \;\; \frac{d^2}{R_t\,C_\mu} \;, \tag{2.22}$$

$$L_n \;\; = \;\; \sqrt{D_n\,\tau_n} \;\; = \;\; d\,\sqrt{\frac{R_{ct}}{R_t}} \;, \tag{2.23}$$

where d is the thickness of nanoporous TiO$_2$ film.

Measurement Setup. The EIS measurement was performed with an Autolab Frequency Analyzer setup equipped with the Autolab PGSTAT 30 (Eco Chemie B.V., Utrecht, The Netherlands) and the Frequency Response Analyzer Module. The DSC test device (Figure 2.2) was set to various forward voltage biases ranging from -0.85 – -0.1 V and the frequency range 0.02 Hz – 1 MHz with an oscillation potential amplitude of 10 mV at 20 °C. The photoanode of DSC device was connected to working electrode, and the counter electrode to the auxilary electrode and the reference electrode. The impedance experiment was conducted under open-circuit condition, either in the dark or submerged to an illumination at fixed intensity (normally 50% of full sun, supplied by white light emitting diode). The obtained impedance spectra were fitted with the Z-view software (version 2.8d, Scribner Associates, Inc.).

2.4   Long-term stability test

For any new photovoltaic technology, passing a long-term stability test is very critical to assess its potential for large scale application. However, for every new system it is not practical to make a large solar panel for 10 or 20 years outdoor evaluation, because innovative materials and device concepts are now being actively pursued and an impressive improvement in the performance of low-cost excitonic solar cells have been seen in the past years. Hence, we submitted our cells covered with a UV absorbing polymer film (see section 2.2) to the 1000 h accelerated testing at 60 °C, in a solar simulator with a light intensity of 100 mW cm^{-2}. Note that the total contribution of UV photons to the standard AM 1.5 G solar emission is relatively small. UV light leads to direct band-edge excitation of TiO$_2$ nanocrystals, generating valence-band holes, which in turn may attack some organic materials in the device. Note that this reaction can be partially suppressed

by the hole capture with iodide ions. Therefore, in our light soaking experiments UV light is avoided by employing an anti-reflection coating material.

Experiment setup. In this experiment, we characterize the robustness of DSC device under prolonged light soaking and moderate thermal stress. After measured its initial values (Section 2.3), the DSC test device was maintained under open-circuit condition ($I = 0$) in the visible light irradiation at 100 mW cm^{-2} light intensity (CPS Sun Simulator, ATLAS GmbH). The temperature was controlled at approx. 60 °C by circulating cooling water. The anti-reflecting sheet (ARKTOP, Asahi Glass) was used to protect the sensitizing part of DSC from UV degradation. The J-V characteristics of the device was re-measured every week up to 6 weeks (1000 hours) to follow up the long-term stability of the device under this condition.

Bibliography

[1] S. Ito, T. N. Murakami, P. Compte, et al. Fabrication of thin film dye sensitized solar cells with solar to electric power conversion efficiency over 10%. *Thin Solid Films*, 516:4613–4619, 2008.

[2] P. Wang, S. M. Zakeeruddin, P. Compte, et al. Enhance the performance of dye-sensitized solar cells by co-grafting amphiphilic sensitizer and hexadecylmalonic acid on TiO$_2$ nanocrystals. *Journal of Physical Chemistry B*, 107:14336–14341, 2003.

[3] P. Wang, S. M. Zakeeruddin, R. Humphry-Baker, et al. Molecular scale interface engineering of TiO$_2$ nanocrystal: Improving the efficiency and stability of dye-sensitized solar cells. *Journal Physical Chemistry B*, 107:14336–14341, 2003.

[4] P. Wang, S. M. Zakeeruddin, P. Comte, et al. Enhance the performance of dye-sensitized solar cells by co-grafting amphiphilic sensitizer and hexadecylmalonic acid on TiO$_2$ nanocrystals. *Journal Physical Chemistry*, 15:2101, 2003.

[5] S. Rühle, M. Greenshtein, S.-G. Chen, et al. Molecular adjustment of the electronic properties of nanoporous electrodes in dye-sensitized solar cells. *Journal Physical Chemistry B*, 109:18907–18913, 2005.

[6] N. Kopidakis, N. R. Neale, and A. J. Frank. Effect of an adsorbent on recombination and band-edge movement in dye-sensitized tio2 solar cells: Evidence for surface passivation. *Journal Physical Chemistry B*, 110:12485–12489, 2006.

[7] A. Kay and M. Grätzel. Artificial photosynthesis. 1. Photosensitization of titania so-
    lar cells with chlorophyll derivatives and related natural porphyrins. *Journal Physical
    Chemistry*, 97:6272–6277, 1993.

[8] M. Wang, X. Li, H. Lin, et al. Passivation of nanocrystalline TiO_2 junctions by
    surface adsorbed phosphinate amphiphiles enhances the photovoltaic performance of
    dye sensitized solar cells. *Dalton Transactions*, pages 10015–10020, 2009.

[9] Z. Zhang, S. M. Zakeeruddin, B. C. O'Regan, et al. Influence of 4-guanidinobutyric
    acid as coadsorbent in reducing recombination in dye-sensitized solar cells. *Journal
    of Physical Chemistry B*, pages 21818–21824, 2005.

[10] N. R. Neale, N. Kopidakis, J. van de Lagemaat, et al. Effect of a coadsorbent on
     the performance of dye-sensitized solar cells: Shielding versus band-edge movement.
     Journal of Physical Chemistry B, pages 23183–23189, 2005.

[11] D. Kuang, C. Klein, Z. Zhang, et al. Stable, high-efficiency ionic-liquid-based meso-
     scopic dye-sensitized solar cells. *Small*, 12:2094–2102, 2007.

[12] Yu Bai, Yiming Cao, Jing Zhang, et al. High-performance dye-sensitized solar cells
     based on solvent-free electrolytes produced from eutectic melts. *Nature Materials*,
     7:626, 2008.

[13] H. Pettersson and T. Gruszecki. Long–term stability of low–power dye–sensitized
     solar cells prepared by industrial methods. *Solar Energy Materials & Solar Cells*,
     70:203–212, 2001.

[14] S. Ito, T. N. Murakami, P. Comte, et al. Fabrication of thin film dye sensitized solar
     cells with solar to electric power conversion efficiency over 10%. *Thin Solid Films*,
     516:4613–4619, 2008.

[15] Michael Grätzel. Solar energy conversion by dye-sensitized photovoltaic cells. *Inor-
     ganic Chemistry*, 44:6841–6851, 2005.

[16] K. Kalyanasundaram and M. Grätzel. Applications of functionalized transition metal
     complexes in photonic and optoelectronic devices. *Coordination Chemistry Review*,
     77:347–414, 1998.

[17] Laurence M. Peter. Dye-sensitized nanocrystalline solar cells. *Physical Chemistry
     Chemical Physics*, 9:2630–2642, 2007.

[18] N. Kopidakis, K. D. Benkstein, J. van de Lagemaat, and A. J. Frank. Temperature dependence of the electron diffusion coefficient in electrolyte-filled TiO_2 nanoparticle films: Evidence against multiple trapping in exponential conduction-band tails. *Physical Review B*, 73:045326, 2006.

[19] M. Bailes, P. J. Cameron, K. Lobato, and L. M. Peter. Determination of the density and energetic distribution of electron traps in dye-sensitized nanocrystalline solar cells. *Journal of Physical Chemistry B*, 109:15429–15435, 2005.

[20] P. E. de Jongh and D. Vanmaekelbergh. Trap-limited electronic transport in assemblies of nanometer-size TiO_2 particles. *Physical Review Letters*, 77(16):3427, 1996.

[21] J. Bisquert, A. Zaban, M. Greenshtein, and I. M. Sero. Determination of rate constants for charge transfer and the distribution of semiconductor and electrolyte electronic energy levels in dye-sensitized solar cells by open-circuit photovoltage decay method. *Journal of the American Chemical Society*, 126:13550–13559, 2004.

[22] Jenny Nelson. Continuous-time random-walk model of electron transport in nanocrystalline TiO_2 electrodes. *Physical Review B*, 59(23):15374, 1999.

[23] J. van de Lagemaat and A. J. Frank. Effect of the surface-state distribution on electron transport in dye-sensitized TiO_2 solar cells: Nonlinear electron-transport kinetics. *Journal of Physical Chemistry B*, 104:4292–4294, 2000.

[24] N. W. Duffy, L. M. Peter, R. M. G. Rajapakse, et al. A novel charge extraction method for the study of electron transport and interfacial transfer in dye sensitised nanocrystalline solar cells. *Electrochemistry Communication*, 2:658–662, 2000.

[25] P. R. F. Barnes, A. Y. Anderson, S. E. Koops, et al. Electron injection efficiency and diffusion length in dye-sensitized solar cells derived from incident photon conversion efficiency measurements. *Journal of Physical Chemistry C*, 113:1126–1136, 2009.

[26] M. J. Ross and K. R. William. *Impedance Spectroscopy: Emphasizing Solid Materials and Systems.* John Wiley & Sons: New York, 1987.

[27] Q. Wang, S. Ito, M. Grätzel, et al. Characteristics of high efficiency dye-sensitized solar cells. *Journal of Physical Chemistry B*, 110:25210–25221, 2006.

[28] J. Bisquert, M. Grätzel, Q. Wang, and F. F. Santiago. Three-channel transmission line impedance model for mesoscopic oxide electrodes functionalized with a conductive coating. *Journal of Physical Chemistry B*, 110:11284–11290, 2006.

[29] J. Bisquert, G. G. Belmonte, F. F. Santiago, and A. Compte. Anomalous transport effects in the impedance of porous film electrodes. *Electrochemistry Communications*, 1:429–435, 1999.

[30] Juan Bisquert. Influence of the boundaries in the impedance of porous film electrodes. *Physical Chemistry Chemical Physics*, 2:4185–4192, 2000.

Chapter 3

Effect of the extended π-conjugation on the ancillary ligand

3.1   Introduction

After O'Regan and Grätzel first reported a dye-sensitized solar cell using Ru complexes as a photosensitizer in 1991 [1], numerous sensitizers have been prepared, and their performance has been tested. A conversion efficiency of up to 11% was achieved by using *cis*-di(thiocyanato)bis(2,2'-bipyridyl-4,4'-dicarboxylate)ruthenium(II) (N3) as a photosensitizer. [2,3] However, the conversion efficiency of DSCs is still lower than that of the silicon-based photovoltaic cells. To obtain a high conversion efficiency, optimization of the short-circuit photocurrent (J_{sc}) and open-circuit potential (V_{oc}) of the cell is essential. The value of V_{oc} depends on the edge of conduction band in TiO_2 and the redox potential of ioidide/triiodide, otherwise J_{sc} is related to the interaction between TiO_2 and the sensitizer as well as the absorption coefficient of the sensitizer. The conduction band of TiO_2 was known to have a Nernstian dependence on pH. [4] Thus, the molecular engineering of the ruthenium complexes for achieving the highest efficiency was attempted to increase the molar absorption coefficient of the complexes.

4,4'-Dicarboxylic acid-2,2'-bipyridine (dcbpy) has been considered as the optimal anchoring ligand in Ru sensitizers. [5] Finding new metal-complex sensitizers with higher conversion efficiency was achieved by modifying one of the anchoring ligands as described in the other chapter (See chapter 4). However, the hydrophilic terminal of Ru-sensitizer

proved unsatisfactory in permitting DSC devices to achieve robust stability and higher photovoltaic performance. This drawback has been successfully addressed with significant improvement through the embodiment of two well-known heteroleptic ruthenium dyes, **Z907** [6, 7] and **Z910** [8]. Furthermore, the replacement of one of the dcbpy anchoring ligands with a highly conjugated ancillary ligand has been reported previously to increase the absorption coefficient and therefore the photocurrent density of the sensitizers. [9–12]

Extending the π-conjugation of the ancillary ligands by incorporating electron-rich thiophene derivatives in the heteroleptic ruthenium complexes has been proved to enhance significantly the light harvesting capacity. [13–16] In this chapter, we report a new heteroleptic ruthenium sensitizers; **C103** [17]; featuring 3,4-ethylenedioxythiophene unit in its ancillary ligand; **B11** [18] which contains hexylthio-bithiophene unit in its ancillary ligand, and **B19** which combines both hexylthio-bithiophene unit in its ancillary ligand and a vinyl-conjugation in its anchoring ligand. The molecular structures of the three sensitizers are shown in figure 3.1.
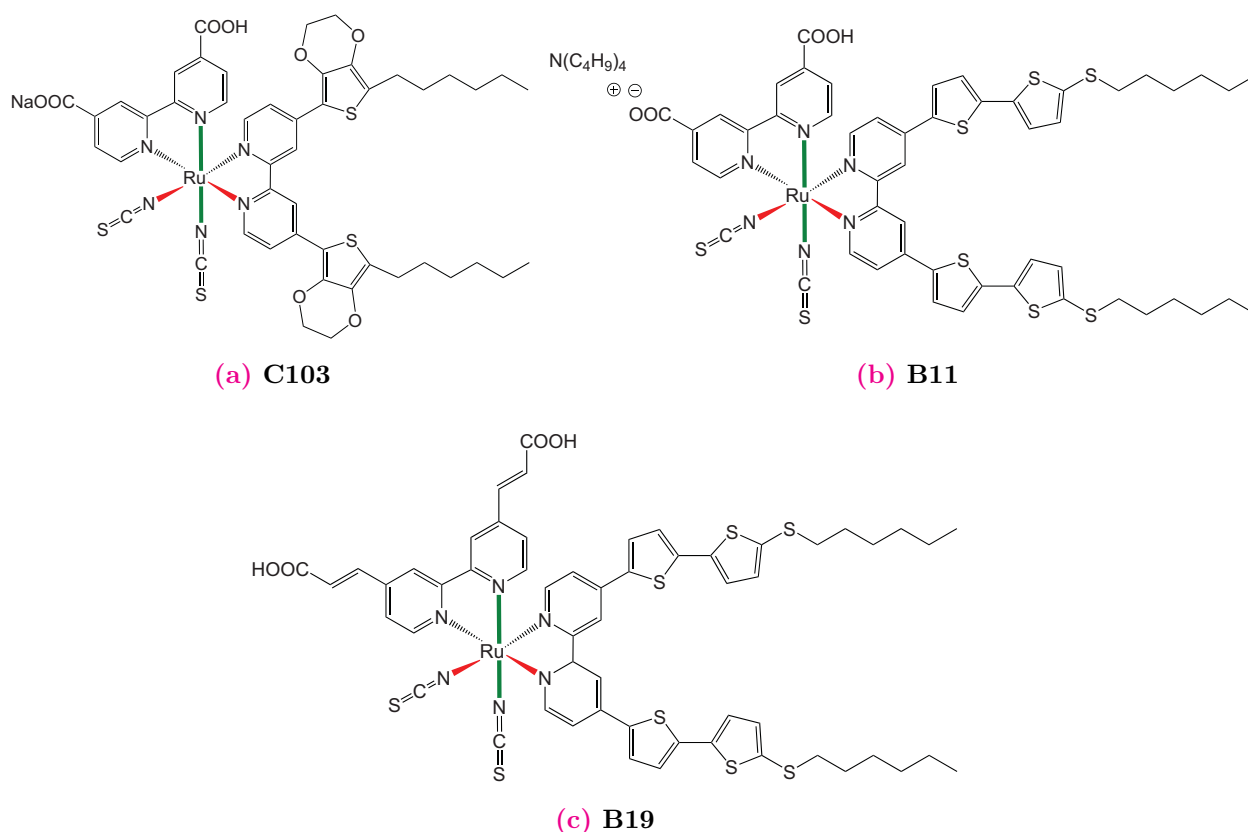

(a) **C103**

(b) **B11**

(c) **B19**

Figure 3.1: Molecular structures of sensitizers **C103**, **B11** and **B19**.

3.2   Photophysical and electrochemical studies

The electronic absorption spectra of **C103**, **B11** and **B19** are displayed in figure 3.2. From figure 3.2a, the spectrum of **C103** has two intense absorption bands at 307 and 365 nm in the UV region and the characteristic metal-to-ligand charge-transfer transition (MLCT) absorption bands in the visible region. In DMF, the low energy MLCT transition absorption peaks at 550 nm, which is 24 nm red-shifted compared to that of standard sensitizer **Z907** (See section 4). The measured peak molar extinction coefficient (ϵ) is 1.88×10^4 M^{-1} cm^{-1}, which is significantly higher than the corresponding values for the standard Z907 (1.22×10^4 M^{-1} cm^{-1}). [6] Excitation of the low energy MLCT transition of the **C103** sensitizer in DMF produces an emission centered at 800 nm. The measured negative offset of its LUMO (-0.81 V vs NHE) relative to the conduction band edge (-0.50 V vs NHE) of TiO_2 provides the thermodynamic driving force for charge generation. The formal redox potential ($\phi^0(S^+/S)$) of the **C103** sensitizer is 0.90 V vs. NHE, which is 0.50 V higher than that of the iodide/triiododide couple employed in the electrolyte, supplying ample driving force for efficient dye regeneration and thus net charge separation (See support information of [17]).
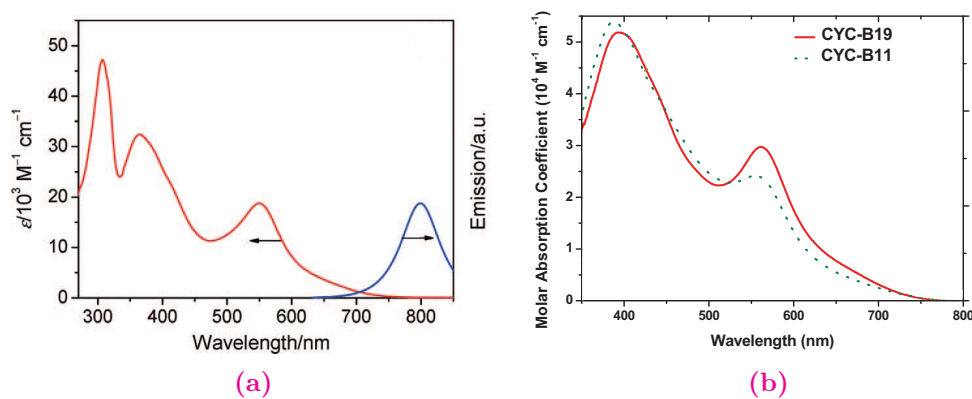
Figure 3.2: a) Electronic absorption and emission spectra of **C103** sensitizer dissolved in DMF and b) Electronic absorption spectra of **B11** and **B19** dissolved in DMF and anchored on transparent TiO_2 films with thickness ~8 μm.

From figure 3.2b, **B11** shows three absorption bands centered at 305, 388 and 554 nm, respectively. The band at 305 nm is assigned to the overlap of intraligand π-π* transitions of anchoring and ancillary ligands. Another band centered at 388 nm also contains two components: the π-π* transition of the ancillary ligand and one of the MLCT transitions. The molar absorption coefficient (ϵ) of the lower energy MLCT band centered at 554 nm is 2.42×10^4 M^{-1} cm^{-1}. This significant augmentation of the MLCT absorption cross section

is attributed to the hexylthio-bithiophene unit action in increasing both the electron donating ability and extension of the π-conjugation to the bipyridyl ancillary ligand. This is primarily because the third row, electron rich sulfur atom has the greater radial orbital extension in its bonding compared to the second row element such as carbon. Inserting a sulfur atom between the thiophene ring and alkyl substituent may result in an increase of the electronic transition dipole moment and, therefore, the absorption coefficient of the MLCT band. [11] This result reveals that the light-capturing ability of the high molar extinction coefficient ruthenium dyes can be further enhanced by careful design of the electron donating segments. [19]

B19 dissolved in DMF displays two intense absorption bands centered at 393 nm and 562 nm, respectively as shown in figure 3.2b. The former band is assigned to the overlap of intra-ligand π-π^* transitions of auxiliary ligand and one of the MLCT bands. The second peak with a λ_{max} at 562 nm and a remarkably high ϵ of 2.97×10^4 M^{-1}cm^{-1} is attributed to MLCT transition associated most intensively with the incident photon-to-current conversion efficiency (IPCE) of the cell based on **B19** in this lower energy range. Promisingly, the low-energy MLCT band of **B19** is red-shifted compared to that of **B11** and its transition intensity enhanced by ~23%. This implies that the elongation of the conjugation length on the anchoring ligand may be a remedy for reinforcing the spectral response of the ruthenium-coordinated sensitizer. When **B19** is anchored onto the surface of transparent TiO$_2$ film, a slight blue-shift (~11 nm) of MLCT band is observed along with a change in the absorption profile, indicating that the **B19** on TiO$_2$ film undergoes a conformational change induced by the de-protonation in self-assembly process. Despite the absorption bands centered around 550 nm of both dyes have a similar intensity, **B19** anchored on TiO$_2$ film is able to harvest more red and blue light more than the **B11** dye molecule.

To investigate the energetics of the driving force for electron injection from photo-excited dye into the conduction band of TiO$_2$ and the regeneration of oxidized dye via electron donation from the iodide/triiodide redox couple, square-wave voltammetry combined with the absorption threshold were utilized to determine the energy levels of the ground and excited states for **B11** and **B19**. As shown in figure 3.3, the ground state potential of **B19** dissolved in DMF is 0.97 V vs NHE (-5.47 eV vs vacuum), which is close to that of **B11** and more positive than the redox potential of the iodide/triiodide couple used in the liquid electrolyte. Interestingly, the oxidation potential of **B19** adsorbed on the transparent TiO$_2$ film is shifted cathodically by 0.15 V compared to that measured in DMF. On the other hand, the oxidation potential of **B11** adsorbed on TiO$_2$ film is only

slightly higher (0.02 V) than that measured in DMF as displayed also in figure 3.3. The optical transition energy, E_{0-0}, of **B19** determined from its absorption onset measured in DMF is 1.57 eV. Neglecting entropy changes during the excitation, the excited-state redox potential, $\phi^0(S^+/S^*)$, is -0.60 V vs NHE (-3.90 eV vs vacuum), which is slightly more positive than that of **B11** (-0.62 V vs NHE; -3.88 eV vs vacuum).

When the two sensitizers are anchored on the surface of TiO$_2$, the optical transition energy, E_{0-0}, of **B19** and **B11** shift to 1.51 eV and 1.55 eV, yielding the excited-state redox potential of two dyes to be -0.39 V vs NHE (-4.11 eV vs vacuum) and -0.57 V vs NHE (-3.93 eV), The excited state potentials of the two sensitizers obtained in DMF are more negative than the conduction band of TiO$_2$ (ca. -0.3 V vs NHE; -4.2 eV) [20], benefiting electron injection from these excited states to TiO$_2$ film.
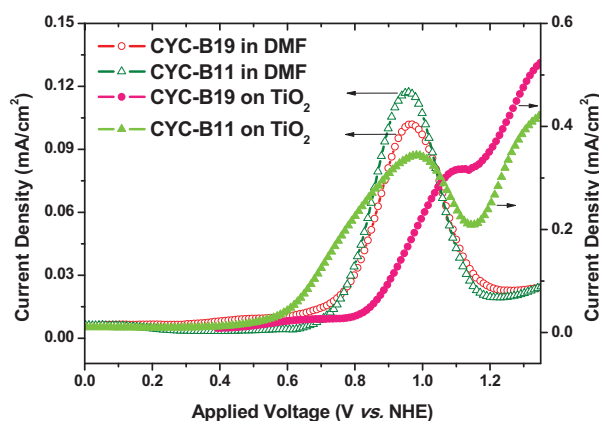
Figure 3.3: Square-wave voltammaograms of dye molecules, B11 and B19 in DMF and on transport TiO$_2$ film, respectively Supporting electrolyte: 0.1 M TBAPF$_6$ Potential step increment: 10 mV; frequency: 25 Hz.

3.3 Photovoltaic performance

3.3.1 C103 sensitizer

To evaluate the performance of this novel sensitizer, the test devices; device A and device B, have been prepared following the standard device fabrication (section 2.2). A solution containing **C103** (300 μm) and 3α,7α-dihydroxy-5β-cholic acid coadsorbent (300 μM) (Cheno, see figure 2.1c) in a mixture of acetonitrile and *tert*-butanol (volume ratio: 1/1) was used. Device A and device B were fabricated using low-volatile MPN-based electrolyte

(Z946), and solvent-free ionic liquid electrolyte (Z952), respectively.

The photocurrent action spectrum of device A with a low-volatility electrolyte is shown in figure 3.4a. The IPCE exhibits a high plateau of over 70% from 410 to 670 nm, reaching a maximum of 91% at 570 nm. As shown in figure 3.4b, under standard AM 1.5 G condition, the short-circuit photocurrent density (J_{sc}), open-circuit photovoltage (V_{oc}), and fill factor (FF) of device A with a low-volatility, MPN-based electrolyte are 17.51 mA cm^{-2}, 771 mV, and 0.71, respectively, yielding an overall conversion efficiency (η) of 9.6%. The overlap intergral of the IPCE curve with the standard global AM 1.5 G solar emission spectrum generates a J_{sc} of 17.47 mA cm^{-2}, indicating that there is very small spectral mismatch between our solar simulator and the standard AM 1.5 G sunlight. At various lower incident light intensities, overall power conversion efficiencies (table 3.1) are even higher, reaching up to 10.0%.
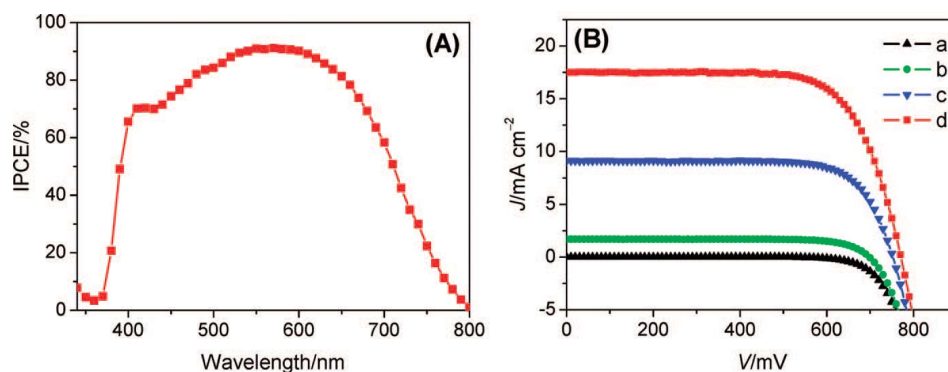
Figure 3.4: (A) Photocurrent action spectrum of device A employing the **C103** sensitizer in conjugation with a low-volatility electrolyte. (B) J-V characteristics measured (a) in dark and (b-d) under an irradiance of AM 1.5 G sunlight attenuated to different light intensities with various metal meshes. (b) 9.4 mW cm^{-2}; (c) 51.3 mW cm^{-2}; (d) 99.8 mW cm^{-2}. The aperture area of metal mask: 0.158 cm^2. A UV-absorbing anti-reflection film is covered on the cell during measurements.

More importantly, the photovoltaic parameters (J_{sc}, V_{oc}, FF, and η of device B with a solvent-free ionic liquid electrolyte under AM 1.5 G sunlight are 15.93 mA cm^{-2}, 710 mV, 0.747, and 8.5%, respectively. Under a low light intensity of 9.4 mW cm^{-2} attenuated by metal mesh, a very impressive efficiency of 9.1% has been reached. This new record efficiency for a solvent-free DSC will promote considerably the practical application of flexible devices, which are frequently operated under reduced light intensities and for which ionic liquids are the electrolytes of choice. Note that using the same TiO$_2$ film and electrolyte, it was previously reported that cell with the **Z907** dye gives a J_{sc} of 14.26 mA cm^{-2} under the AM 1.5G full sunlight [21] which proves the merit of better light

harvesting capacity of this new **C103** sensitizer.

Device	P_{in} (mW cm^{-2})	V_{oc} (mV)	J_{sc} (mA cm^{-2})	FF	η (%)
A	9.4	700	1.7	0.77	9.7
	51.3	760	9.1	0.74	10.0
	99.8	771	17.5	0.71	9.6
B	9.4	645	1.6	0.81	9.1
	51.3	688	8.6	0.78	8.9
	99.8	710	15.9	0.75	8.5

Table 3.1: Detailed photovoltaic parameters of device A and B made with **C103** as sensitizer and Cheno as coadsorbent (1/1 volume ratio), measured under different incident light intensities (P_{in}: Incident power intensity). The cell area tested with a metal mask: 0.158 cm^2.

3.3.2 B11 sensitizer

Some preliminary photovoltaic experiments were conducted to evaluate the performance of the **B11** dye using an acetronitrile-based electrolyte (Z960) and a low-volatile MPN-based electrolyte (Z946), respectively. The DSC test devices were fabricated and characterized as described in chapter 2. Ultrathin and transparent TiO$_2$ films of only 5 μm thickness were used in initial studies to fabricate photovoltaic devices, rendered possible by the enhanced optical cross section of **B11**. The photovoltaic parameters J_{sc}, V_{oc}, FF, and η, of the thin film cell based on **B11** in conjunction with a low-volatility electrolyte (Z946) are 16.1 mA cm^{-2} 0.714 V, 0.69, and 7.9%, respectively (see table 3.2). In the presence of dineohexyl bis-(3,3-dimethyl-butyl)-phosphinic acid (DINHOP, see section 2.1.6) as a coadsorbent (4:1 molar ratio in the dye solution), the photovoltaic parameters are 15.5 mA cm^{-2} 0.732 V, 0.73, and 8.2%. DINHOP has been demonstrated as an effective coadsorbent for reducing the dark current. [22]

It is very encouraging to obtain such a high efficiency with a thin transparent TiO$_2$ film (5 μm) using MPN-containing low-volatility electrolyte (Z946). These results clearly reveal the advantages of the ruthenium dyes with high molar extinction coefficient. In DSCs, the thickness of the TiO$_2$ film plays a vital role on the cell performance. By using a TiO$_2$ double layer film 8+5 μm (8 μm thick of 20 nm TiO$_2$ particle as working layer plus 5 μm thick of 400 nm TiO$_2$ particle as scattering layer), the efficiency of devices

with the low-volatility electrolyte (Z946) was further increased to 9.4% (table 3.2. At lower light intensity of 50 mW cm^{-2}, the efficiency of the device was as high as 9.8%. Figure 3.5a (curve B) presents the photocurrent density voltage characteristic curve of an acetonitrile-based electrolyte (Z960) DSC under standard AM 1.5G simulated sunlight (100 mW cm^{-2}) illumination. The **B11**-sensitized cell provides a J_{sc} of 20.05 mA cm^{-2}, a V_{oc} of 0.743 V and a *FF* of 0.77, yielding an η of 11.5%. The IPCE spectrum (as shown in figure 3.5b) shows a plateau of over 80% from 460 to 685 nm with the maximum of 95% at 580 nm. Considering the light absorption and scattering loss by the conducting glass, the maximum efficiency for absorbed photon-to-collected electron conversion efficiency is close to unity over a broad spectral range. The J_{sc} agrees with the value calculated from the overlap integral of the IPCE spectrum with standard AM 1.5 G solar emission spectrum showing that the spectral mismatch of simulated sunlight is less than 2%. To the best of our knowledge this is the highest efficiency published for a volatile electrolyte containing DSC.
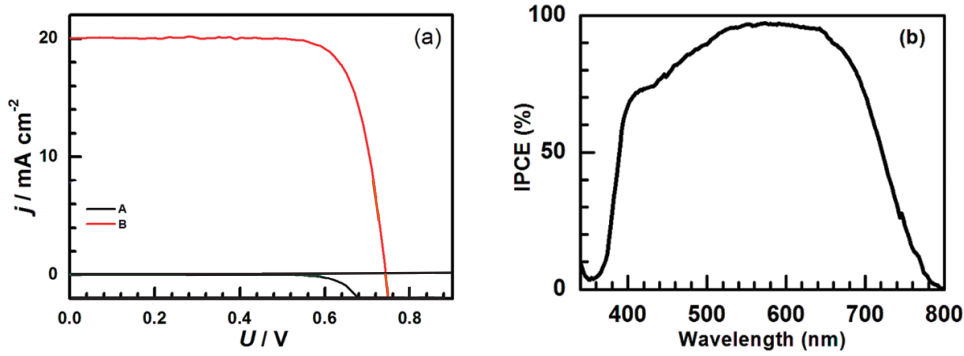
Figure 3.5: a) *J-V* characteristics of DSC device based on **B11** with Z960 electrolyte on 8+5 μm thick double layer TiO$_2$ film (cell area 0.158 cm^2), measured in the dark (curve A) and under an illumination of the AM 1.5 G full sunlight intensity (100 mV cm^{-2}) (curve B). b) IPCE spectrum of the same device.

3.3.3   B19 sensitizer

To explore the potential of **B19** sensitizer, the DSC test devices have been fabricated using 8-μm-thick transparent TiO$_2$ films in corporation with a volatile acetronitrile-based electrolyte with modified lithium iodide (LiI) concentrations. Device A used an electrolyte Z959 (see Appendix B for a composition of this electrolyte). Device B, C and D were fabricated by using Z959 electrolyte with the addition of 0.05 M, 0.1 M and 0.2 M LiI, respectively. The characteristic *J-V* curves of four devices sensitized with **B19**, measured

Device	TiO$_2$ thickness (μm)	V_{oc} (mV)	J_{sc} (mA cm^{-2})	FF	η (%)
B11	5	714	16.1	0.69	7.9
B11 + DINHOP (4:1)	5	732	15.5	0.73	8.2
B11	8 + 5	686	18.0	0.68	8.4
B11 + DINHOP (4:1)	8 + 5	704	18.3	0.73	9.4

Table 3.2: Detailed photovoltaic parameters of **B11**-sensitized devices of varying film thicknesses in the presence and absence of DINHOP as coadsorbent, using low-volatile electrolyte (Z946), under full sunlight intensity.

under the illumination of air mass 1.5 global (AM 1.5G) simulated sunlight (100 mW cm^{-2}) are displayed in figure 3.6a, and the detailed photovoltaic parameters are collected in table 3.3. When the concentration of lithium iodide increases, the short-circuit current density (J_{sc}) of device enhances progressively from 14.7 to 17.0 mA cm^{-2}; meanwhile the open-circuit voltage (V_{oc}) and fill factor (FF) decrease slightly. Among these transparent devices, the best conversion efficiency of 8.4% is reached by device C. The corresponding IPCE spectra of the four devices presented in figure 3.6b show a broad spectral response in the range from 450 nm to 650 nm, obtaining a maximum efficiency of 67%, 80%, 85% and 89% for devices A, B, C and D, respectively. These results substantiate that the electron injection from photo-excited **B19** to the conduction band of TiO$_2$ occurs moderately even though the driving potential for electron injection is small.
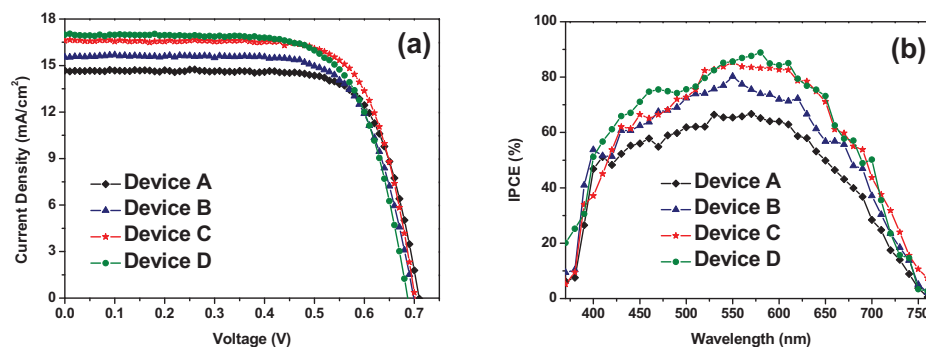
Figure 3.6: a) J-V characteristic curves of transparent devices sensitized with **B19** with various concentrations of lithium iodide: 0 M (device A); 0.05 M (device B); 0.1 M (device C) and 0.2 M (device D), respectively measured under AM 1.5 G simulated sunlight illumination (100 mW cm^{-2}). b) The corresponding IPCE spectra of devices. (Thickness of TiO$_2$ film: 8 μm; cell active area tested with a mask: 0.158 cm^2).

Figure 3.7 displays the relative evolution of IPCE values for devices monitored at 450

Device	Electrolyte	V_{oc} (mV)	J_{sc} (mA cm^{-2})	FF	η (%)
A	Z959	710	14.7	0.74	7.7
B	Z959+0.05 M LiI	699	15.5	0.72	7.8
C	Z959+0.10 M LiI	702	16.6	0.72	8.4
D	Z959+0.20 M LiI	686	17.0	0.70	8.1

Table 3.3: Detailed photovoltaic parameters of **B19**-sensitized devices with various concentration of LiI in electrolyte, measured under AM 1.5 G simulated sunlight (100 mW cm^{-2}).

nm, 560 nm and 700 nm, respectively following an increase of lithium iodide concentration in the electrolyte. In the blue light region (450 nm), the monochromatic conversion efficiency of device D is improved by ca. 27% when 0.2 M LiI is added. Such a magnitude of improvement can be achieved easily in the green light (560 nm). Moreover, the enhancement in the red light (700 nm) regions is nearly proportional to the concentration of lithium ions added into the electrolyte. In other words, the effects of lithium ions on the enhancement of J_{sc} value are energy-dependent, which is associated with the fact that introduction of lithium ions in electrolytes leads to a downward shift of the conduction band of TiO$_2$ thereby favouring the injection of relatively low energetic electrons harvested by **B19**. [23–25]
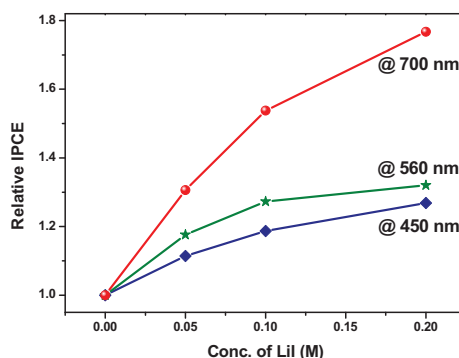
Figure 3.7: Evaluation of IPCE values of **B19**-sensitized devices monitored at 450 nm, 560 nm and 700 nm, respectively, as a function of LiI concentration.

To appraise the benefits of MLCT enhancement in **B19**, another device sensitized by **B11** (device E) was fabricated under the same device conditions as those employed in device C. Device E, sensitized by **B11** yields a J_{sc} of 16.3 mA cm^{-2}, a V_{oc} of 0.712 V and a FF of 0.72, providing also a conversion efficiency of 8.4% equal to that of device C. The corresponding IPCE spectra of two devices (C and E) are shown in figure 3.8. Device C

sensitized by **B19** can convert photons into electricity more efficiently than the devices sensitized by **B11**, especially in the red light region. The higher J_{sc} by the **B19**-sensitized device C reveals that the enhancement evidently stems from the molecular modification on the anchoring ligands for ruthenium sensitizers. In addition to the J_{sc}, the V_{oc} is also a critical photovoltaic parameter responsible for overall conversion efficiency. It is known that the V_{oc} of a DSC is determined intrinsically by the potential difference between the quasi-Fermi level of TiO$_2$ and the redox potential of the electrolyte. Furthermore, the V_{oc} will be affected by a shift of TiO$_2$ conduction band edge [26] as well as the degree of electron recombination. [27, 28]
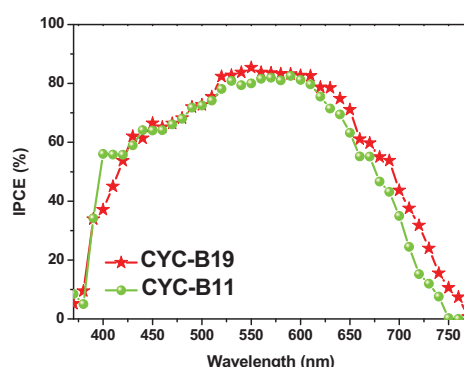
Figure 3.8: IPCE spectra of devices sensitized by **B19** (device C) and **B11** (device E), respectively, using 8-μm-thick TiO$_2$ film; cell active area: 0.159 cm^2.

In order to examine the influence of the lithium ion concentration on the V_{oc}, the transient measurements were carried out on devices A to D. Figure 3.9a depicts the V_{oc} of devices A to D as a function of chemical capacitance indicating that the open circuit voltage decreases with an increase in the concentration of lithium ion increases, a finding consistent with a lowering of the conduction band energy of the TiO$_2$ induced by lithium ions. [24] Under the assumption that the energetic distributions of surface trap states and bulk states of TiO$_2$ remain unchanged, as LiI increased from 0 to 0.2 M a decrease of V_{oc} by ca. 20 to 60 mV could be expected at such high chemical capacitance as indicated in figure 3.9a. However, as shown in figure 3.6a and table 3.3, the observed V_{oc} variation is actually in the range of 8 to 24 mV. This relatively small shift suggests that the interfacial back reaction of the electron injected into TiO$_2$ with the triiodide in the electrolyte is retarded as the concentration of lithium ion raises. [29, 30] Figure 3.9b displays the plots of recombination lifetime of devices versus photo-induced charge density for the four devices. At the same photo-induced charge density, the recombination lifetime is enhanced with an increase of lithium ion concentration in the electrolyte. These results support the observation that higher concentrations of lithium ions do lead to a better

screening of the negative charges inside the TiO_2 matrix against the electrolyte thereby reduce the charge recombination.
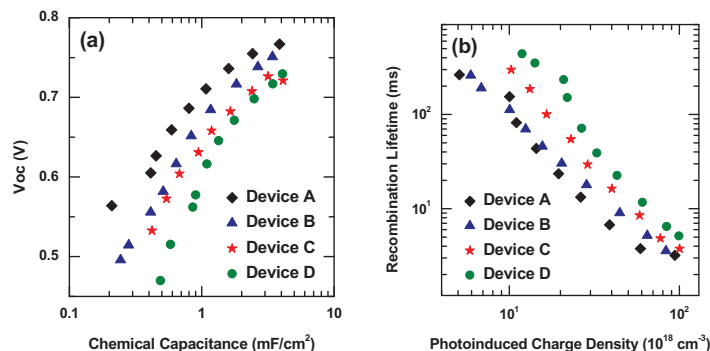

Figure 3.9: Transient photoelectrical measurement of devices based on **B19** with various concentration of lithium iodide. a) V_{oc} of devices as a function of chemical capacitance (C_μ) and b) recombination lifetime of devices as a function of photo-induced charge density.

3.4   Long-term stability

For any new photovoltaic technology, passing a long-term stability test is very critical to assess its potential for largescale application. As presented in figure 3.10, both **C103** devices with a low-volatility electrolyte (device A) and a solvent-free ionic liquid electrolyte (device B) showed good stability when subjected to the accelerating test in a solar simulator under full sunlight (100 mW cm^{-2}) at 60 °C by retainting 91% and 94% of their initial efficiencies of 9.6% and 8.4%, respectively, after 1000 h test period (see subsection 3.3.1). Such an impressively stable performance implies the robustness of **C103** itself as well as the sensitized-heterojunction interface.

The **B11**-based device in association with a low volatility electrolyte (see subsection 3.3.2) was also used to evaluate the preliminary stability of the **B11** sensitizer under the same visible-light soaking. The photovoltaic parameters J_{sc}, Voc, FF, and η of the cell varied only slightly from the initial values as shown in figure 3.10. The value of the efficiency retained 93% of its initial value after 1000 h light soaking, a small drop of 62 mV in V_{oc} being compensated by an increase in the J_{sc} values.

This is the first time such high efficiency DSCs have passed preliminary stability tests, which should considerably encourage the surging investigations on various nanostructured solar cells. Note that a cell showing a similar stability with the **Z907** dye has a 7.7% initial

efficiency. [21] Overall, our systematic experiments have suggested that it is important to employ amphiphilic sensitizers like **Z907**, **C103** and **B11** to achieve a stable DSC.
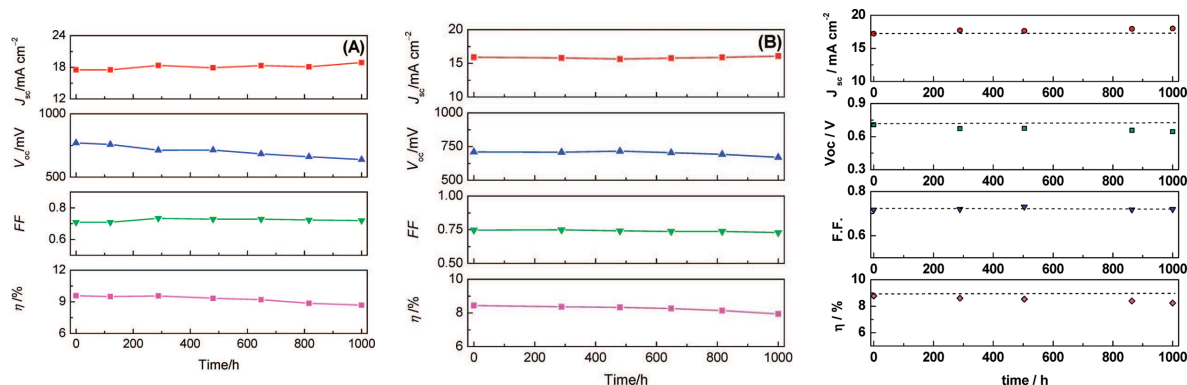

Figure 3.10: Evaluation of the photovoltaic parameters for the device based on **C103** using 7+5 μm TiO$_2$ double layer film with (a) a low-volatility electrolyte (Z946) (device A), and (b) a solvent-free ionic liquid electrolyte (Z952) (device B), in a presence of Cheno (1:1 molar ratio) as coadsorbent during the successive full sunlight soaking (100 mW cm^{-2}) at 60 °C. (c) Detailed photovoltaic parameters measured under the same visible light soaking for the device based on 8+5 μm TiO$_2$ double layer film sensitized with **B11** in the presence of DINHOP (4:1 molar ratio) as coadsorbent and low-volatile electrolyte (Z946).

Details of the electron recombination dynamics between the photoinjected electrons at the TiO$_2$ and the oxidized electrolyte in various **B11**-sensitized devices was investigated by employing transient photovoltage measurements, also known as V_{oc} decays (See section 2.3.3). Figure 3.11a illustrates the extracted charge density versus open-circuit voltage plot for the fresh and aged devices. The open-circuit voltage is lower for the aged device at all charge densities examined (ca. 74 mV difference at a charge density of 0.94×10^{18} cm^{-3}). The differences in voltage may be due to; (a) a shift on the TiO$_2$ conduction band with respect to the redox potential of electrolytes or (b) difference in the dye-sensitized heterojunction interfacial recombination reaction. Figure 3.11b shows the recombination lifetime for various devices. Following the increase of the extracted charge density from the TiO$_2$ film, the recombination lifetimes (τ_e) become shorter due to the higher electron density at the TiO$_2$ and larger driving forces for the interfacial recombination. Clearly, the trend of the charge recombination lifetime of the various devices is well in agreement with that of the measured photocurrent densities (see section 3.3.2). The recombination lifetime in the fresh and aged device exhibits only minor differences, showing an almost complete independence with respect to the time of light soaking.

The V_{oc} of the DSC is determined by the potential difference between the quasi-Fermi

level of the electrons at the TiO_2 film and the redox potential of the electrolyte. The former is related to the electron steady-state concentration under illumination, which depends on the energy offset between the Fermi level and the conduction band potential (see section 2.3.3). Thus, we conclude that the lower observed V_{oc} of the aged device (at identical electron densities as those measured in the fresh device) is most likely related to a *positive shift* (vs NHE) of the TiO_2 conduction band potential following light soaking, since the electron lifetimes measured for both fresh and aged devices are very close. The positive shift (vs NHE) of conduction band potential may originate from the photoinduced proton intercalation into the titania close to the TiO_2 surface, during the long-term light soaking test. [31–33]
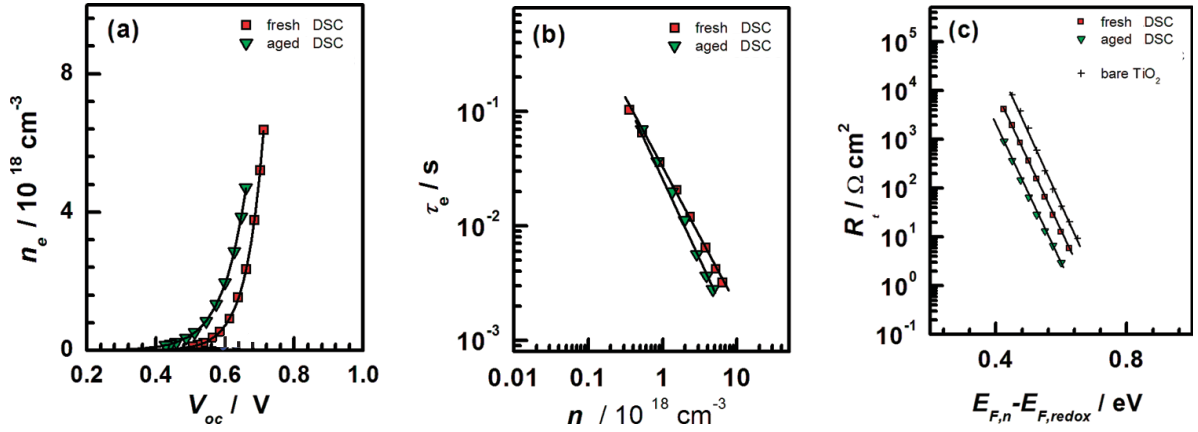
Figure 3.11: Transient photovoltage decay measurement of the fresh and aged devices with **B11**/DINHOP (4:1 molar ratio). The effect of light soaking was shown as a relationship between (a) the photoinduced charge density *vs* V_{oc} and (b) the recombination lifetime *vs* the photoinduced charge density. (c) Electron transport resistance R_t of TiO_2 film obtained by EIS measurement in the dark at 20 °C as a function of applied voltage bias. The resistance for bare TiO_2 (no sensitizer) with Z946 was also provided for comparison. The parameters (n_e and R_t) were normalized with respect to the TiO_2 film thickness, taking into account the porosity (67% for 20 nm TiO_2 working layer and 42% for the 400 nm TiO_2 scattering layer from BET measurements) for deriving the content of solid within the nanocrystalline film.

Electrochemical Impedance Spectroscopy (EIS) was also conducted to monitor the photovoltaic parameter changes in aged devices. Figure 3.11c presents the effect of the applied voltage on the electron transport resistance R_t under dark conditions for the fresh and aged devices (see section 2.3.4). For comparison, the resistance in the bare TiO_2 (the blank experiments without an adsorbing dye layer on the TiO_2) is also provided. The logarithm of the electron transport resistance, which depends on the number of free electrons ([e⁻]) in the conduction band, shows parallel behavior for both fresh and aged

devices. This implies that the shift of the resistances for the steady state electron transport in those devices is caused by a change in position of the conduction band edge (E_{cb}). [22,30] In the case of the **B11**/DINHOP cografted TiO$_2$ film (fresh device), a downward shift of the conduction band edge energy level (E_{cb}) by approximately 38 mV with respect to the Fermi level of the redox couple (iodide/triiodide) was clearly observed compared to the bare TiO$_2$ within the same electrolyte (Z946 in this case). This displacement arises from the protonation of the titania surface occurring when sensitizer and coadsorbent molecules are linked onto the oxides by the anchoring groups. [22] This energy shift influences principally the open-circuit voltage of the DSC device, an observation that has likewise been confirmed by transient photovoltage decay measurements.

3.5 Conclusion

In this chapter, the effect of extending π-conjugated system on ancillary ligand has been investigated through the three novel heteroleptic amphiphilic sensitizers; **C103** featuring 3,4-ethylenedioxythiophene unit, **B11** which contains hexylthio-bithiophene unit and **B19** which combines both hexylthio-bithiophene unit in its ancillary ligand and a vinyl-conjugation in its anchoring ligand. **C103** has set new benchmarks for high performance and practical DSCs with conversion efficiency of 9.6% and 8.5% with low-volatility and solvent-free electrolyte, respectively. Both devices maintain their efficiencies over 90% of initial values under prolonged light soaking at 60 °C. **B11** and **B19** exhibit an excellent light-harvesting capacity with high molecular extinction coefficient (ϵ). The corresponding **B11**-based DSC cell using a volatile electrolyte gives a new-high conversion efficiency of 11.5% under AM 1.5 G simulated sunlight. The cell employed low-volatile electrolyte also shows good performance (9.4%) and stability. The effect of π-extension in both anchoring and ancillary ligand in **B19** shows an excellent conversion efficiency of 8.4% with transparent 8 μm TiO$_2$ film and modified Lithium content in volatile electrolyte. Although the efficiency **B19** did not exceed that of **B11** based on devices fabricated under the identical conditions, the corresponding IPCE spectra suggest that the device sensitized with **B19** can convert photons into electricity more efficiently than the one sensitized with **B11**, especially in the red light region.

These initial results clearly demonstrate the benefits for improvements in performance and stability through the use of highly proficient light-harvesting ruthenium dyes in the thin film DSC. These types of cells are very promising and higher photovoltaic efficiencies

will most certainly be obtained in the future. Further works on searching other potential functionalities are underway to enhance the light-harvesting capability of incorporated Ru sensitizer and charge-collection yields of stained mesoscopic semiconducting films.

Bibliography

[1] Brian O'Regan and Michael Grätzel. A low-cost, high-efficiency solar cell based on dye-sensitized colloidal films. *Nature*, 353:737, 1991.

[2] M. K. Nazeeruddin, F. D. Angelis, S. Fantacci, et al. Combined experimental and DFT-TDDFT computational study of photoelectrochemical cell ruthenium sensitizers. *Journal of the American Chemical Society*, 127:16835–16847, 2005.

[3] Michael Grätzel. Conversion of sunlight to electric power by nanocrystalline dye-sensitized solar cells. *Journal of Photochemistry and Photobiology A: Chemistry*, 164:3–14, 2004.

[4] S. G. Yan and J. T. Hupp. Semiconductor-based interfacial electron-transfer reactivity: Decoupling kinetics from pH-dependent band energetics in a dye-sensitized titanium dioxide/aqueous solution system. *Journal of Physical Chemistry*, 100:6867, 1996.

[5] Y. Takahashi, H. Arakawa, H. Sugihara, et al. Highly efficient polypyridyl-ruthenium(II) photosensitizers with chelating oxygen donor ligands: β-diketonato-bis(dicarboxybipyridine)ruthenium. *Inorganica Chimica Acta*, 310:169–174, 2000.

[6] S. M. Zakeeruddin, M. K. Nazeeruddin, R. Humphry-Baker, et al. Design, synthesis, and application of amphiphilic ruthenium polypyridyl photosensitizers in solar cells based on nanocrystalline TiO_2 films. *Langmuir*, 18:952–954, 2002.

[7] P. Wang, S. M. Zakeeruddin, J. E. Moser, et al. A stable quasi-solid-state dye-sensitized solar cell with an amphiphilic ruthenium sensitizer and polymer gel electrolyte. *Nature Materials*, 2:402–407, 2003.

[8] P. Wang, S. M. Zakeeruddin, J. E. Moser, et al. Stable new sensitizer with improved light harvesting for nanocrystalline dye-sensitized solar cells. *Advanced Materials*, 16:1806, 2004.

[9] T. Renouard, R.-A. Fallahpour, Md. K. Nazeeruddin, et al. Novel ruthenium sensitizers containing functionalized hybrid tetradentate ligands: Synthesis, characterization, and INDO/S analysis. *Inorganic Chemistry*, 41:367, 2002.

[10] C. Klein, Md. K. Nazeeruddin, P. Liska, et al. Engineering of a novel ruthenium sensitizer and its application in dye-sensitized solar cells for conversion of sunlight into electricitym. *Inorganic Chemistry*, 44:178, 2005.

[11] C.Y. Chen, S. J. Wu, C. G. Wu, et al. A ruthenium complex with superhigh light-harvesting capacity for dye-sensitized solar cells. *Angewandte Chemie*, 118:5954–5957, 2006.

[12] P. Wang, C. Klein, R. H. Baker, et al. A high molar extinction coefficient sensitizer for stable dye-sensitized solar cells. *Journal of the American Chemical Society*, 127:808–890, 2005.

[13] C.Y. Chen, S. J. Wu, J.-Y. Li, et al. A new route to enhance the light-harvesting capability of ruthenium complexes for dye-sensitized solar cells. *Advanced Materials*, 19:3888–3891, 2007.

[14] F. Gao, Y. Wang, D. Shi, et al. Enhance the optical absorptivity of nanocrystalline TiO$_2$ film with high molar extinction coefficient ruthenium sensitizers for high performance dye-sensitized solar cells. *Journal of the American Chemical Society*, 130:10720–10728, 2008.

[15] F. Gao, Y. Wang, J. Zhang, et al. A new heteroleptic ruthenium sensitizer enhances the absorptivity of mesoporous titania film for a high efficiency dye-sensitized solar cell. *Chemical Communications*, pages 2635–2637, 2008.

[16] A. Abbotto, C. Barolo, L. Bellotto, et al. Electron-rich heteroaromatic conjugated bipyridine based ruthenium sensitizer for efficient dye-sensitized solar cells. *Chemical Communications*, pages 5318–5320, 2008.

[17] D. Shi, N. Pootrakulchote, R. Li, et al. New efficiency records for stable dye-sensitized solar cells with low-volatility and ionic liquid electrolytes. *Journal of Physical Chemistry C*, 112:17046–17050, 2008.

[18] C. Y. Chen, M. Wang, J. Y. Li, N. Pootrakulchote, et al. Highly efficient light-harvesting ruthenium sensitizer for thin-film dye-sensitized solar cells. *ACS Nano*, 3:3103–3109, 2009.

[19] Y. Cao, Y. Bai, Q. J. Yu, et al. Dye-sensitized solar cells with a high absorptivity ruthenium sensitizer featuring a 2-(hexylthio)thiophene conjugated bipyridine. *Journal of Physical Chemistry C*, 113:6290–6297, 2009.

[20] C. Goh, S. R. Scully, and M. D. McGehee. Effects of molecular interface modification in hybrid organic-inorganic photovoltaic cells. *Journal of Applied Physics*, 101:114503, 2007.

[21] Y. Bai, Y. Cao, J. Zhang, et al. High-performance dye-sensitized solar cells based on solvent-free electrolytes produced from eutectic melts. *Nature Materials*, 7:626, 2008.

[22] M. Wang, X. Li, H. Lin, et al. Passivation of nanocrystalline TiO_2 junctions by surface adsorbed phosphinate amphiphiles enhances the photovoltaic performance of dye sensitized solar cells. *Dalton Transactions*, pages 10015–10020, 2009.

[23] D. F. Watson and G. J. Meyer. Cation effects in nanocrystalline solar cells. *Coordination Chemistry Reviews*, 248:1391–1406, 2004.

[24] N. Kopidakis, K. D. Benkstein, J. van de Lagemat, and A. J. Frank. Transport-limited recombination of photocarriers in dye-sensitized nanocrystalline TiO_2 solar cells. *Dalton Transactions*, 107:11307–11315, 2003.

[25] S. E. Koops, B. C. O'Regan, P. R. F. Barnes, and J. R. Durrant. Parameters influencing the efficiency of electron injection in dye-sensitized solar cells. *Journal of the American Chemical Society*, 131:4808–4818, 2009.

[26] Z. Zhang, S. M. Zakeeruddin, B. C. O'Regan, et al. Influence of 4-guanidinobutyric acid as coadsorbent in reducing recombination in dye-sensitized solar cells. *Journal of Physical Chemistry B*, 109:21818–21824, 2005.

[27] A. Reynal, A. Forneli, E. Martinez-Ferrero, et al. Interfacial charge recombination between electron-and the iodide/triiodide electrolyte in ruthenium heteroleptic complexes: Dye molecular structure vs open circuit voltage relationship. *Journal of the American Chemical Society*, 130:13558–13567, 2008.

[28] B. C. O'Regan, K. Walley, M. Juozapavicius, et al. Structure/function relationships in dyes for solar energy conversion: A two-atom change in dye structure and the mechanism for its effect on cell voltage. *Journal of the American Chemical Society*, 131:3541–3548, 2009.

[29] R. Katoh, M. Kasuya, S. Kodate, et al. Effects of 4-*tert*-butylpyridine and li ions on photoinduced electron injection efficiency in black-dye-sensitized nanocrystalline TiO$_2$ films. *Journal of Chemical Physics and Physical Chemistry*, 113:20738–20744, 2009.

[30] M. Wang, P. Chen, R. Humphry-Backer, et al. The influence of charge transport and recombination on the performance of dye-sensitized solar cells. *Journal of Chemical Physics and Physical Chemistry*, 10:290–299, 2009.

[31] F. Matar, T. H. Ghaddar, K. Walley, et al. A new ruthenium polypyridyl dye, TG6, whose performance in dye-sensitized solar cells is surprisingly close to that of N719, the dye to beat for 17 years. *Journal of Material Chemistry*, 18:4246–4253, 2008.

[32] H. Gerischer. Neglected problems in the pH dependence of the flatband potential of semiconducting oxide and semiconductors covered with oxide layers. *Electrochimica Acta*, 34:1005–1009, 1989.

[33] Md. K. Nazeeruddin, R. Humphry-Baker, P. Liska, and M. Grätzel. Investigation of sensitizer adsorption and the influence of protons on current and voltage of a dye-sensitized nanocrystalline TiO$_2$ solar cell. *Journal of Physical Chemistry B*, 107:8981–8987, 2003.

Chapter 4

Effect of the extended π-conjugation on the anchoring ligand

4.1 Introduction

During the past two decades, DSCs with power conversion efficiency over 10% were initially demonstrated using *cis*-di(thocyanato)-bis[2,2′-bipyridyl-4,4′-dicarboxylic acid] ruthenium(II) (coded **N3**) or its bis-tetrabutylammonium (TBA) salt counterpart (coded **N719**) as sensitizers in combination with a thicker titania film (> 12–15 μm) and a volatile electrolyte. [1] To increase the ability to tolerate water in the electrolyte so that there will be no water-induced desorption of sensitizers from TiO_2 surface, **N3** was functionalized with a hydrophobic moiety; 4,4′-dinonyl-2,2′-bipyridine as ancillary ligand. [2] However, in order to enhance power conversion efficiencies of DSCs, it is imparative to design novel sensitizers that exhibit an enhanced molar absorptivity in combination with a red-shift of the metal-to-ligand charge transfer (MLCT) transitions. Extension of the π-conjugation of the ancillary ligand and/or the anchoring ligand was found to improve the spectral response of corresponding ruthenium sensitizers. [3–9] Thus, efforts were recently made by incorporating thiophene derivatives into the ancillary bipyridine ligand in order to increase the molar absorption coefficient of the ruthenium dyes and to enhance their light-harvesting capacity as well as the spectral response. [7,10–16]

Here, we present a novel homoleptic and a novel amphiphilic heteroleptic Ru(II) complexes, referred to as **BTC-1** [4] and **BTC-2** [5], respectively. Both complexes incor-

perate thiophene unit as an extended π-conjugation system between the bipyridine and carboxylate groups. This is the first time that a novel anchoring ligand incorporating a thiophene unit for homoleptic and amphiphilic sensitizers is presented. Figure 4.1 shows the molecular structure of the two novel sensitizers **BTC-1** and **BTC-2**, as well as standard sensitizers **N719** and **Z907**.

(a) **N719**

(b) **Z907**

(c) **BTC-1**

(d) **BTC-2**
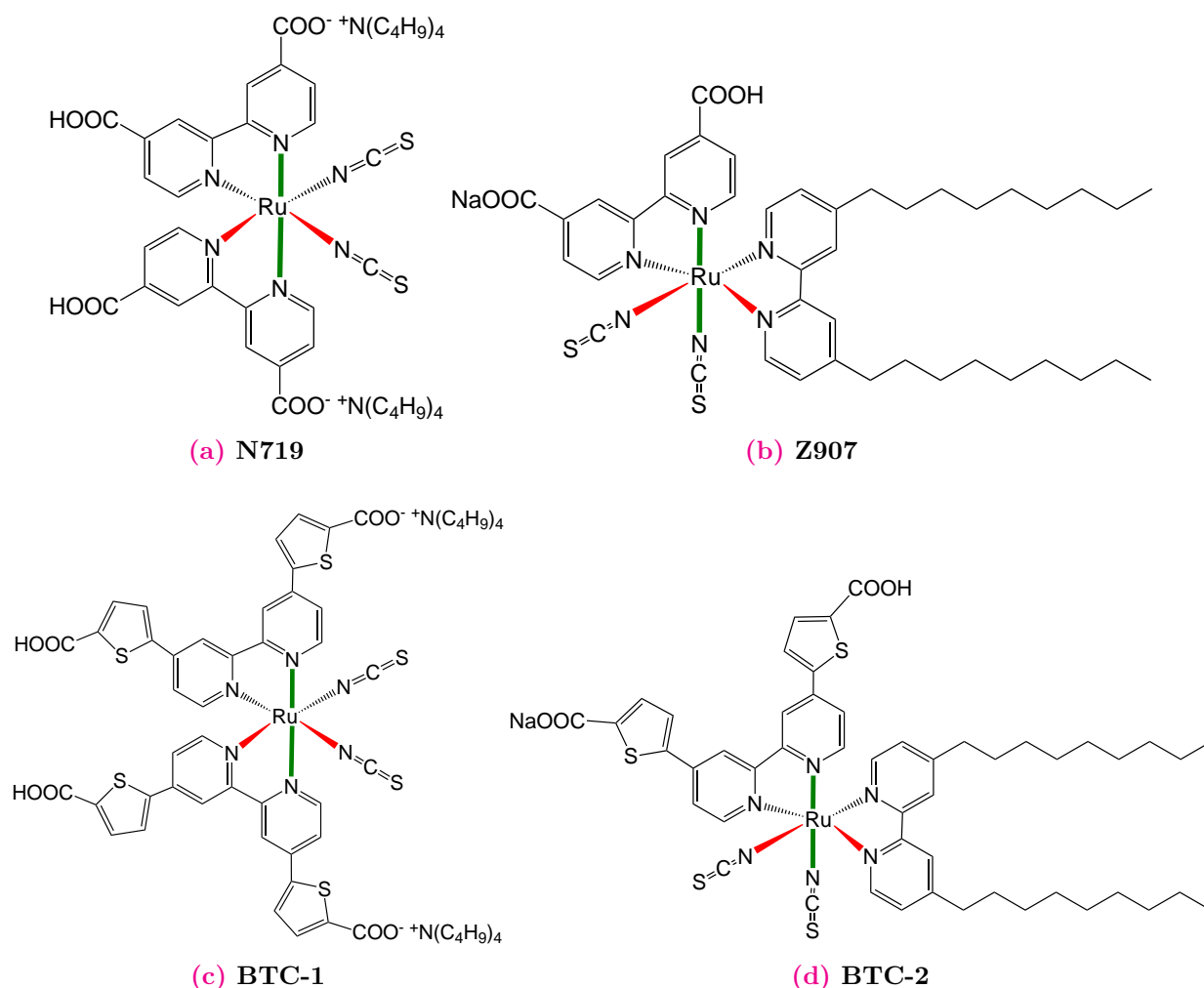
Figure 4.1: Molecular structures of sensitizers **N719**, **Z907**, **BTC-1** and **BTC-2**.

4.2 Homoleptic sensitizer

Homoleptic complex **BTC-1** was prepared in a typical one-pot procedure. The detailed preparation was described elsewhere. [4]. The electronic absorption spectrum of **BTC-1** in Dimethylformamide (DMF) is shown in figure 4.2 and the data are summarized in table

4.1. Complex **BTC-1** showed broad absorption bands in the 300 to 750 nm region. The absorption spectrum of **BTC-1** is dominated by MLCT transitions. The lowest energy MLCT band at 563 nm is 28 nm red-shifted compared to the standard **N719** sensitizer due to the extension of π-conjugation in the anchoring ligand and increased HOMO energy level.

Importantly, an increase of 72% of the molar extinction coefficient (ϵ) was observed for the longest wavelength MLCT band as a consequence of the insertion of thiophene units to the ligand compared to **N719** sensitizer. The emission data of the dyes were obtained in an air-equilibrated DMF solution at 298 K by exciting at the respective low energy MLCT absorption bands, showing a weak emission maximum at 800 nm for **BTC-1** and at 794 nm for **N719**.

The excited state oxidation potential of a sensitizer plays an important role in electron transfer processes. The quasi-Fermi level of the TiO_2 photoanode and the redox level of the iodide/triiodide-based electrolyte are situated at around -4.0 eV and -4.83 eV vs. vacuum, respectively. The HOMO level of **BTC-1** is located at -5.29 eV, the LUMO level at -3.34 eV. Overall, the HOMO-LUMO band gap of **BTC-1** ($E_g = 1.95$ eV) is approximately 370 meV smaller compared to **N719** ($E_g = 2.32$ eV), which is also reflected in the red-shift of the absorption spectrum. The position of the LUMO level of **BTC-1** is sufficiently more negative than the TiO_2 conduction band to facilitate efficient electron transfer from the excited dye to TiO_2. On the other hand, the HOMO level of **BTC-1** is sufficiently below the energy level of the redox mediator allowing dye regeneration.
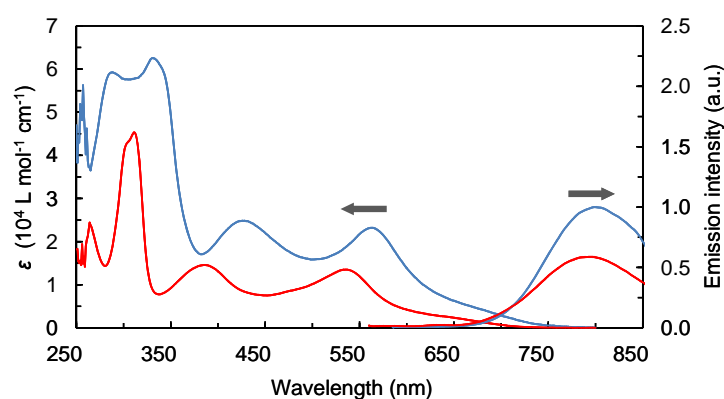

Figure 4.2: Electronic absorption and emission spectra of **BTC-1** (blue line) and **N719** (red line) in DMF.

Figure 4.3b shows the IPCE spectra obtained by DSC test devices sensitized with **BTC-1** and **N719** sensitizer using 3.3 μm transparent photoanodes and a MPN-based

Sensitizer	λ_{abs} [nm] (ϵ [L mol^{-1} cm^{-1}])	λ_{em} [nm]	HOMO [eV]	LUMO [eV]	$\triangle E$ [eV]
BTC-1	287 (59 000) 331 (62 300) 426 (24 800) 563 (23 200)	800	-5.29	-3.34	1.95
N719	312 (47 200) 388 (13 800) 535 (13 500)	794	-5.38	-3.06	2.32

Table 4.1: Photophysical and electrochemical data of **BTC-1** and **N719** measured in DMF (HOMO-LUMO vs. Fc/Fc$^+_{vac}$ = -5.1 eV).

electrolyte. **N719** and **BTC-1** exhibit at 550 nm IPCE values of 67 and 74%, respectively, with an extended red response for **BTC-1**. Under standard global AM 1.5 G solar conditions, **BTC-1**-sensitized cells gave a short-circuit photocurrent density (J_{sc}) of 12.2 mA cm^{-2}, an open-circuit voltage (V_{oc}) of 0.68 V, and a fill factor (FF) of 0.74, corresponding to an overall conversion efficiency of 6.1% (See figure 4.3a). Such a high performance is very intriguing for a Ru(II)-sensitizer on a 3.3 μm thin TiO$_2$ film in corporate with a low-volatility electrolyte. Under similar conditions, **N719** dye-sensitized cells gave an overall conversion efficiency of only 4.8%. The photovoltaic parameters are given in table 4.2. The J_{sc} value of the **BTC-1** sensitizer is 34% higher compared to that of **N719**. This observation is in accordance with the red-shifted absorption in the visible region and the increased molar extinction coefficient.

The influence of nanocrystalline TiO$_2$ film thickness on the photovoltaic performance with **BTC-1** sensitizer was studied using film thicknesses of 3.3 and 5.5 μm. Additionally, a thick TiO$_2$ film composed of 7 μm transparent layer and 5 μm scattering layer was tested. The detailed photovoltaic parameters of corresponding devices with **BTC-1** and **N719** are given in the table 4.2. Increasing the film thickness from 3.3 over 5.5 to 7+5 μm for **BTC-1** resulted in an increase of the current densities from 12.2 over 14.1 to 15.8 mA cm^{-2}. As a consequence, the overall cell performance was increased from 6.1 to 7.6% under full sunlight. It is interesting to note that with thinner films the photovoltaic performance of **BTC-1** devices outperformed **N719** devices, whereas, with double layer films the performance was nearly identical. With a double layer film the advantage of higher cross section of dye is compensated by the reflecting particle layer containing the red photons in the film and as a result both sensitizers gave almost identical values.

(a)

(b)
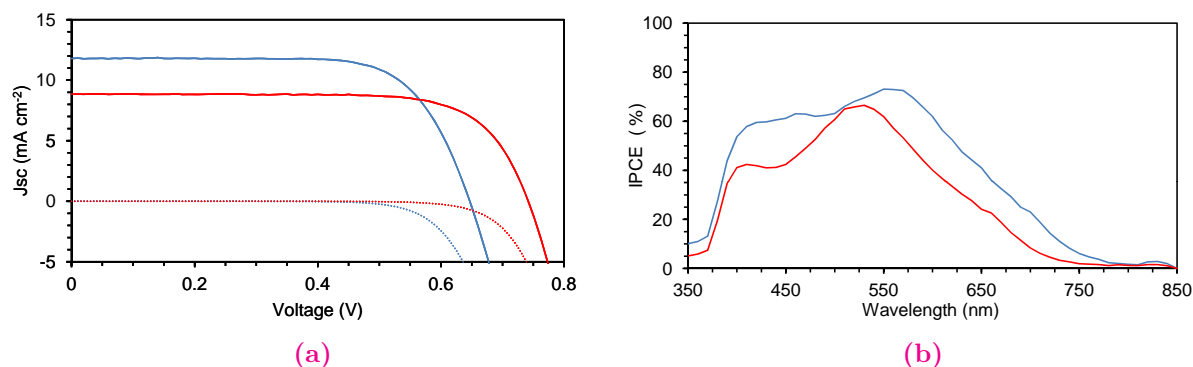
Figure 4.3: (a) J-V characteristics of DSC with **BTC-1** (blue) and **N719** (red) sensitizers in the dark (dotted line) and under full sunlight (solid line). Cell area is 0.158 cm^2. (b) IPCE spectra of **BTC-1** (blue) and **N719** (red) sensitizers on 3.3 μm thin nanocrystalline TiO$_2$ films.

Sensitizer	TiO$_2$ film thickness (μm)	V_{oc} (V)	J_{sc} (mA cm^{-2})	FF	η (%)
BTC-1	3.3	0.68	12.2	0.74	6.1
	5.5	0.67	14.1	0.73	6.9
	7 + 5	0.66	15.8	0.73	7.6
N719	3.3	0.74	9.1	0.71	4.8
	5.5	0.72	12.5	0.70	6.3
	7 + 5	0.71	15.3	0.71	7.7

Table 4.2: Comparison of photovoltaic parameters under full sunlight intensity of **BTC-1** and **N719** absorbed on nanocrystalline TiO$_2$ films of various thicknesses.

In conclusion, extending the π-conjugation of the anchoring ligand by 5,5′-(2,2′-bipyridine-4,4′-diyl)-bis(thiophene-2-carboxylic acid) has increased the DSC performance in thin films as a result of the increased molar extinction coefficient and enhanced spectral response in the red wavelength region. This class of sensitizers containing thiophene in the anchoring site has not been previously reported. This approach allows the design of efficient panchromatic sensitizers with increased photovoltaic conversion efficiencies.

4.3   Heteroleptic amphiphilic sensitizer

Similar to **BTC-1**, the heteroleptic amphiphilic complex **BTC-2** sensitizer was prepared in a typical one-pot procedure. [5] The absorption and emission maxima of **BTC-2** measured in DMF solution are summarized in table 4.3 and compared to standard sensitizer **Z907**. The absorption and normalized emission spectra are displayed in figure 4.4. Complex **BTC-2** showed broad absorption bands in the 300 to 750 nm region. The lower energy part of the absorption spectrum of the complex is dominated by MLCT transitions with maxima at 422 and 548 nm. A red-shift of about 28 nm was observed for the lowest energy MLCT band of **BTC-2** compared to the standard **Z907** sensitizer because of the extension of π-conjugation in the anchoring ligand and an increased HOMO energy level. The low energy MLCT absorption band at 548 nm of the **BTC-2** dye has a molar extinction coefficient of 1.6×10^4 L mol^{-1} cm^{-1}, which is higher than the corresponding value for **Z907** (1.2×10^4 L mol^{-1} cm^{-1}). An increase of about 30% of the molar extinction coefficient was observed for the longest wavelength MLCT band as a consequence of the insertion of thiophene units to the ligand compared to **Z907** sensitizer. The emission data of the sensitizers were obtained in an air-equilibrated DMF solution at 298 K by exciting at the respective low energy MLCT absorption band, showing a weak emission maximum at 805 nm for **BTC-2** and at 760 nm for **Z907**.
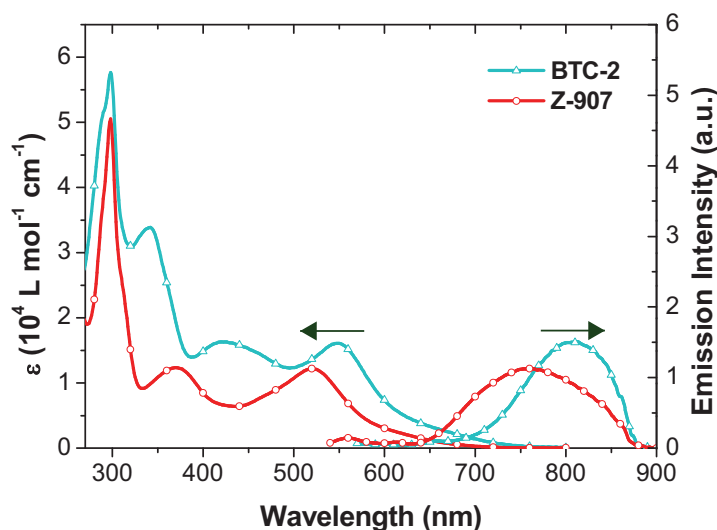

Figure 4.4: Electronic absorption and emission spectra of **BTC-2** and **Z907** in DMF.

Electrochemical studies. For a highly efficient sensitizer in DSCs, the LUMO energy level should be compatible with the conduction band edge energy of the TiO$_2$ photoanode (-4.0 eV vs vacuum) and its HOMO should be sufficiently low in energy to accept electrons

Sensitizer	λ_{abs} [nm] (ϵ [L mol^{-1} cm^{-1}])	λ_{em} [nm]	HOMO [eV]	LUMO [eV]	$\triangle E$ [eV]
BTC-2	548 (16 000)	805	-5.22	-3.30	1.92
	422 (16 200)				
	341 (33 700)				
	299 (57 500)				
Z907	526 (12 200)	760	-5.28	-3.11	2.17
	370 (12 300)				
	298 (50 700)				

Table 4.3: Optical and electrochemical data of **BTC-2** and **Z907** measured in DMF (HOMO-LUMO vs. Fc/Fc$^+_{vac}$ = -5.1 eV).

from the iodide/triiodide-based redox electrolyte (-4.83 eV vs vacuum). The HOMO level of **BTC-2** was determined to -5.22 eV and the LUMO level was -3.30 eV. Overall, the HOMO-LUMO band gap of **BTC-2** ($E_g = 1.92$ eV) is approximately 250 meV smaller than that of **Z907** ($E_g = 2.17$ eV), which is also reflected in the red-shift of the absorption spectrum. It was found that the HOMO energy levels of **BTC-2** match well with the redox potential of iodide/triiodide allowing regeneration of the sensitizer cation. The LUMO level of the sensitizer is much more negative than the conduction-band edge of TiO$_2$, thus providing a thermodynamic driving force for efficient electron injection. Therefore, the red-shifted absorption and higher molar extinction coefficient of **BTC-2** together with the well-matched energy levels should lead to a better conversion efficiency than the **Z907** sensitizer.

Photovoltaic performance. The IPCE spectrum and *J-V* characteristics of **BTC-2** sensitizer were assessed in test devices using standard mesoporous 7+5 μm thick TiO$_2$ films and a volatile acetonitrile-based electrolyte (Z984, see Appendix B for a composition of this electrolyte). Using 4-guanidinobutyric acid (GBA) (see section 2.1.6) as a coadsorbent the **BTC-2**-sensitized cell provided a short-circuit current density (J_{sc}) of 16.1 mA cm^{-2}, an open-circuit voltage (V_{oc}) of 0.75 V, and a fill factor (*FF*) of 0.74, yielding an overall power conversion efficiency (η) of 9.1% under standard AM 1.5 G sunlight. The corresponding IPCE spectrum showed a plateau of over 80% from 455 to 620 nm, with the maximum of 85% at 550 nm. (See figure 4.5 The J_{sc} agrees with the value calculated from the overlap integral of the IPCE spectrum with standard AM 1.5 G solar emission spectrum showing that the spectral mismatch is less than 2%.
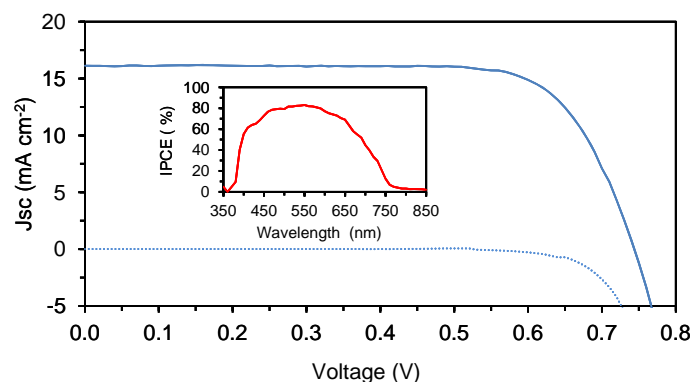
Figure 4.5: *J-V* characteristics of a double layer 7+5 TiO_2 film device sensitized with **BTC-2** using GBA as coadsorbent, in cooperate with volatile electrolyte Z984, in the dark (dotted line) and under AM 1.5 G illumination (100 mW cm^{-2}) (solid line). The inset is IPCE spectrum of the same device.

To demonstrate the potential of the **BTC-2** compared to the standard sensitizer **Z907**, which lacks the thiophene moieties in the anchoring groups, devices were prepared under identical conditions using the MPN-based electrolyte (Z946) with thin 3 μm TiO_2 film. The photovoltaic parameters of these devices are shown in figure 4.6 and the data are summarized in table 4.4. It is evident that the J_{sc} values obtained with a 3-μm thin TiO_2 film sensitized with the **BTC-2** are 18% higher than those of the corresponding devices prepared with **Z907**. As the TiO_2 film thickness increases from 3 μm to 5 μm, the J_{sc} values of devices using **BTC-2** are approximately 10% higher than those of the corresponding **Z907**. With a double-layer film (7+5 μm), a beneficial influence of the high molar extinction coefficient of sensitizer **BTC-2** over **Z907** on the short circuit photocurrent was not observed because it was nullified by the presence of reflecting particles in the double layer structure TiO_2 film and practically the same values were obtained.

Long-term stability. The long-term stability of a DSC device is a crucial parameter for its practical application in photovoltaics. To demonstrate the potential of the **BTC-2** sensitizer, devices based on **BTC-2** were optimized by using a double-layered TiO_2 film (7+5 μm) sensitized with **BTC-2** and GBA as a coadsorbent, in conjunction with a low-volatile MPN-based electrolyte as a solvent. From table 4.4, device B provided a J_{sc} of 15.1 mA cm^{-2}, a V_{oc} of 0.74 V, and a *FF* of 0.74, yielding an overall efficiency, η , of 8.3% under standard AM 1.5 G sunlight. In order to explore the stability of device B, the cell covered with a 50-μm-thick polyester film, which acted as a UV cut-off filter for the accelerated test, was illuminated with visible light (1 sun; 100 mW cm^{-2}) at 60 °C. After 1000 hours of light soaking and thermal stress, the photovoltaic parameters J_{sc}, V_{oc},
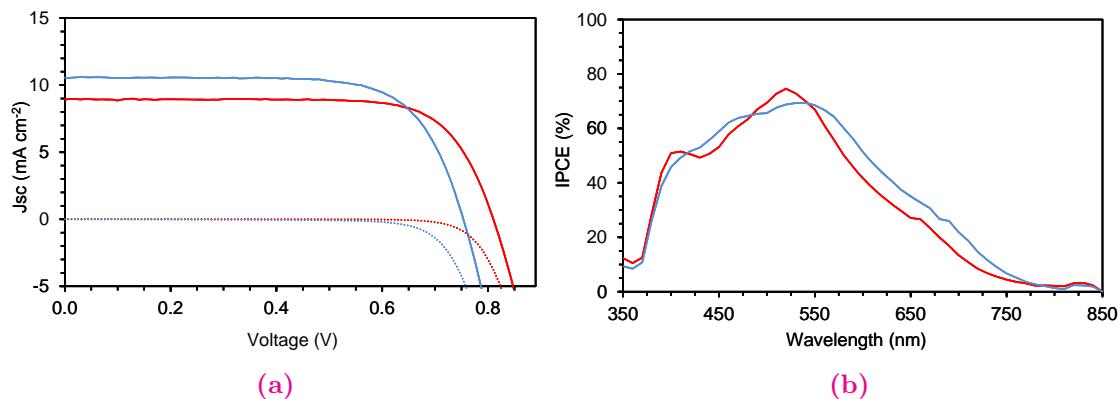
Figure 4.6: (a) J-V characteristics of DSC with **BTC-2** (blue) and **Z907** (red) sensitizers with GBA as coadsorbent in the dark (dotted line) and under full sunlight (solid line). The TiO$_2$ film contains a transparent layer of 3 μm thickness and the low-volatile electrolyte Z946 is used. (b) IPCE spectra of the same device.

Sensitizer	Device	Electrolyte	TiO$_2$ film (μm)	V_{oc} (V)	J_{sc} (mA cm^{-2})	FF	η (%)
BTC-2	B	Z984	7 + 5	0.75	16.1	0.74	9.1
BTC-2	A	Z946	7 + 5	0.71	14.8	0.72	7.6
	B	Z946	7 + 5	0.74	15.1	0.74	8.3
	B	Z946	5	0.75	12.7	0.73	7.0
	B	Z946	3	0.75	10.5	0.71	5.7
Z907	A	Z946	7 + 5	0.70	14.8	0.71	7.5
	B	Z946	5	0.80	11.1	0.74	6.6
	B	Z946	3	0.81	8.9	0.74	5.4

Table 4.4: Photovoltaic parameters of devices with TiO$_2$ films of various thicknesses. Device A: without coadsorbent and device B: with coadsorbent.

and *FF* of the cell were slightly changed to 15.0 mA cm^{-2}, 0.71 V, and 0.74, respectively, retaining 96% of its initial η value (See figure 4.7).

In order to understand the changes in the photovoltaic parameters during the aging process, Electrochemical Impedance Spectroscopy (EIS) was carried out with fresh and aged devices. EIS was likewise utilized to monitor the photovoltaic parameter changes in various devices. [17–20] Figure 4.8a presents the effect of the applied voltage (U) on the electron transport resistance R_t under dark conditions for various devices. The electron transfer resistance depends on the density of electrons (n_c) in the conduction band (CB)
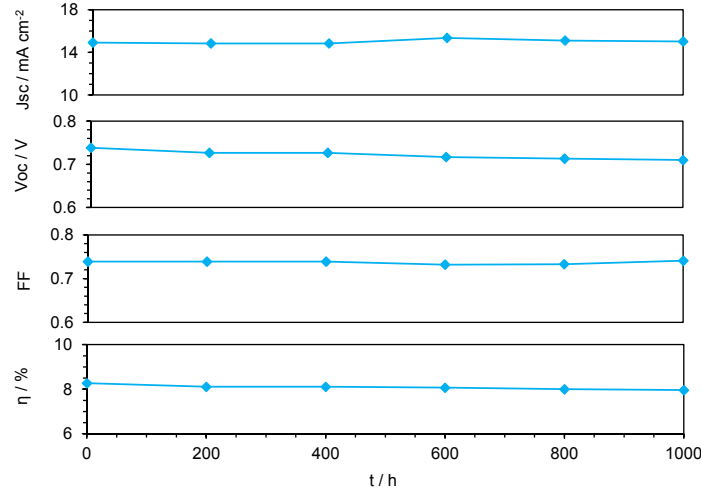
Figure 4.7: Long-term stability evaluation of the photovoltaic parameters for the device based on a 7+5-μm-thick TiO_2 double layer film sensitized with **BTC-2** using GBA as coadsorbent and MPN-based electrolyte.

and the mobility (μ_e, the free electrons diffusion coefficient according to the Einstein relation on diffusion of charged particles). [17] The R_t data from the fresh device B are shifted downward (+30 mV) from those of the fresh device A, which is caused by a shift in the conduction band edge of TiO_2, E_{cb}, towards higher values in fresh device B. [21] Without considering the change in electron mobility (μ_e), in case of the fresh device B, an upward shift of E_{cb} by approximately 88 mV with respect to the Fermi level of the redox couple was observed compared to that of the aged sample using the same electrolyte. Figure 4.8b presents the chemical capacitance (C_μ) versus R_t. Note that an identical resistance means that if the difference in charge mobility is ignored, an equal number of electrons, *i.e.* the same distance between Fermi level (E_F) and E_{cb}, was assumed.

Device B, and in particular the aged device B, showed an augmented chemical capacitance, indicating that more trap states were produced during light soaking and thermal stress, inferring that μ_e in the aged device could have an influence on the electron transfer resistance. Figure 4.8c presents the overall recombination resistance (R_{ct}) for the charge transfer at the TiO_2 /eletrolyte interface with R_t. [22] The fresh device B has largest R_t compared to the aged device at an identical R_t. This result can be attributed to the formation of a more compact monolayer on the film's surface when GBA is co-grafted compared to that formed in the presence of sensitizer alone. After light soaking, the R_{ct} values of the aged device became similar to those of the fresh device A. All devices have a larger value of R_{ct} than R_t, indicating an effective collection of photogenerated charge
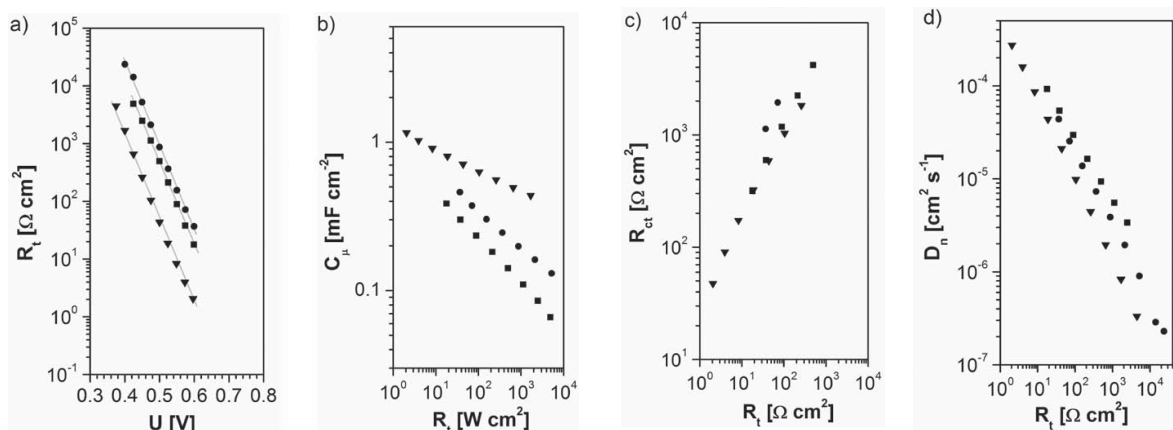
Figure 4.8: Derived equivalent circuit components obtained from EIS measurements under dark condition at 20 °C as a function of electron transfer resistance for three different devices sensitized with ■:**BTC-2**, the fresh device A, and ●,▼: **BTC-2**/GBA, the fresh device B and aged device B. a) Electron transport resistance (R_t) of the TiO$_2$ film, b) chemical capacitance (C_μ), c) recombination resistance (R_{ct}) and d) electron diffusion coefficient (D_n).

carriers in the dye-sensitized heterojunction. A slightly decreased apparent electron diffusion coefficient ($D_n = d/R_t C_\mu$, where d is the film thickness) in the devices B was observed and is illustrated in Figure 4.8d. This indicates that the GBA has a small influence on the electron transport in the TiO$_2$ nanoparticles, which might be due to the creation of surface states. For the aged sample, a large decrease in the apparent electron diffusion coefficient was observed under identical R_t, clarifying the influence of the light soaking and thermal stress on the dye-sensitized TiO$_2$ nanocrystalline film. Figure 4.9a shows the charge density vs voltage plot for the fresh and aged device under full sunlight soaking at 60 °C (device B). The photovoltage of the DSC is determined by the ratio of the values of free electron concentration in the TiO$_2$ film in the dark and under illumination. [23,24] The leftward shift (about 40 mV at the extracted charge density of 1×10^{18} cm^{-3}) in the charge density curve (the aged sample) can be interpreted as a downward movement (approximately a factor of 4.8) of the TiO$_2$ energy levels relative to the electrolyte. The lower band edge potential creates a larger driving force for the electron injection from the sensitizer; thus, a larger photocurrent was obtained in the aged sample as illustrated by the photovoltaic characteristics. Figure 4.9b shows the electron lifetimes for the fresh and aged cells plotted versus charge density. At an indicated charge density (1×10^{18} cm^{-3} for instance), the electron lifetime for the fresh device is about 1.7 times larger than for the aged one (0.1 ms vs 0.06 ms).
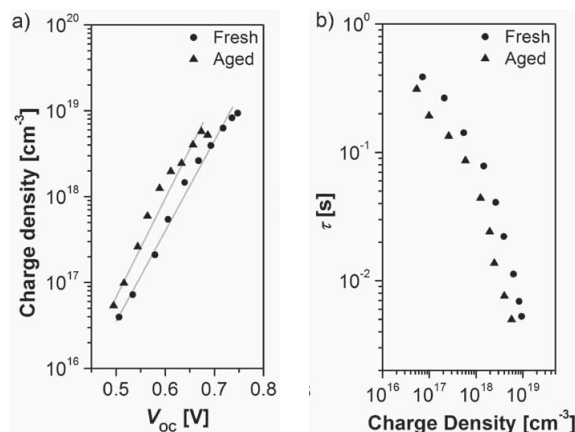
Figure 4.9: Transient photovoltage decay measurements of the fresh and aged devices with **BTC-2** and GBA (1:1 molar ratio): the effect of light soaking on the relationship between a) the photoinduced charge density and open-circuit voltage and b) the recombination lifetime and the photoinduced charge density.

4.4   Conclusion

In summary, we have successfully developed a new homoleptic and an amphiphilic heteroleptic ruthenium sensitizers; **BTC-1** and **BTC-2**, in which the anchoring carboxylic acid groups are extended to the thiophene units. The attachment of anchoring groups to the thiophene units lowered the LUMO energy level of the sensitizers (shift to more negative). Extending the π-conjugation of the anchoring ligand increased the device performance in thin films as a result of the increased molar absorptivity and enhanced spectral response in the red wavelength region. Using ~3-μm-thin mesoporous TiO_2 films, the device with **BTC-1** sensitizer achieved a higher solar-to-electricity conversion efficiency of 6.1% compared to 4.8% for **N719** using low-volatile MPN-based electrolyte. Similarly, the **BTC-2**-based device provided a conversion efficiency of 5.7% compared to 5.4% for **Z907** using the low-volatile MPN-based electrolyte and GBA as coadsorbent. Thicker films that employed a light scattering double layer structure showed 7.6% and 8.3% efficiency for sensitizer **BTC-1** and **BTC-2**, respectively, in combination with a low-volatile MPN-based electrolyte. For device sensitized with **BTC-2** using MPN-based electrolyte showed an excellent stability measured under light soaking at 60 °C. Electrochemical impedance spectroscopy and transient photovoltage decay analysis of this device revealed that the electron lifetime was reduced after long-term light soaking and the conduction band level of TiO_2 film was shifted downward.

Bibliography

[1] M. K. Nazeeruddin, F. D. Angelis, S. Fantacci, et al. Combined experimental and DFT-TDDFT computational study of photoelectrochemical cell ruthenium sensitizers. *Journal of the American Chemical Society*, 127:16835–16847, 2005.

[2] S. M. Zakeeruddin, M. K. Nazeeruddin, R. Humphry-Baker, et al. Design, synthesis, and application of amphiphilic ruthenium polypyridyl photosensitizers in solar cells based on nanocrystalline TiO_2 films. *Langmuir*, 18:952–954, 2002.

[3] Md. K. Nazeeruddin, P. Péchy, and M. Grätzel. Efficient panchromatic sensitization of nanocrystalline TiO_2 films by a black dye based on a trithiocyanato-ruthenium complex. *Chemical Communications*, page 1705, 1997.

[4] A. Mishra, N. Pootrakulchote, M. K. R. Fischer, et al. Design and synthesis of a novel anchoring ligand for highly efficient thin film dye-sensitized solar cells. *Chemical Communications*, pages 7146–7148, 2009.

[5] A. Mishra, N. Pootrakulchote, M. Wang, et al. A thiophene-based anchoring ligand and its heteroleptic Ru(II)-complex for efficient thin-film dye-sensitized solar cells. *Advanced Functional Materials*, 21:963–970, 2011.

[6] M. K. Nazeeruddin, F. D. Angelis, S. Fantacci, et al. Combined experimental and DFT-TDDFT computational study of photoelectrochemical cell ruthenium sensitizers. *Journal of the American Chemical Society*, 127:16835–16847, 2005.

[7] D. Shi, N. Pootrakulchote, R. Li, et al. New efficiency records for stable dye-sensitized solar cells with low-volatility and ionic liquid electrolytes. *Journal of Physical Chemistry C*, 112:17046–17050, 2008.

[8] C. Y. Chen, M. Wang, J. Y. Li, N. Pootrakulchote, et al. Highly efficient light-harvesting ruthenium sensitizer for thin-film dye-sensitized solar cells. *ACS Nano*, 3:3103–3109, 2009.

[9] P. Wang, C. Klein, R. Humphry-Baker, et al. Stable 8% efficient nanocrystalline dye-sensitized solar cell based on an electrolyte of low volatility. *Applied Physics Letters*, 86:123508, 2005.

[10] H. Choi, C. Baik, S. Kim, et al. Molecular engineering of hybrid sensitizers incorporating an organic antenna into ruthenium complex and their application in solar cells. *New Journal of Chemistry*, 32:2233–2237, 2008.

[11] F. Sauvage, M. K. R. Fischer, A. Mishra, et al. A dendritic oligothiophene ruthenium sensitizer for stable dye-sensitized solar cells. *Chemistry and Sustainability Energy and Materials* (CHEMsusCHEM), 2:761–768, 2009.

[12] S. Liu Q. J. Yu, M. Zhang, et al. An extremely high molar extinction coefficient ruthenium sensitizer in dye-sensitized solar cells: The effects of π-conjugation extension. *Journal of Physical Chemistry C*, 113:14559–14566, 2009.

[13] C.Y. Chen, S. J. Wu, C. G. Wu, et al. A ruthenium complex with superhigh light-harvesting capacity for dye-sensitized solar cells. *Angewandte Chemie*, 118:5954–5957, 2006.

[14] C.Y. Chen, S. J. Wu, J.-Y. Li, et al. A new route to enhance the light-harvesting capability of ruthenium complexes for dye-sensitized solar cells. *Advanced Materials*, 19:3888–3891, 2007.

[15] F. Gao, Y. Wang, D. Shi, et al. Enhance the optical absorptivity of nanocrystalline TiO$_2$ film with high molar extinction coefficient ruthenium sensitizers for high performance dye-sensitized solar cells. *Journal of the American Chemical Society*, 130:10720–10728, 2008.

[16] A. Abbotto, C. Barolo, L. Bellotto, et al. Electron-rich heteroaromatic conjugated bipyridine based ruthenium sensitizer for efficient dye-sensitized solar cells. *Chemical Communications*, pages 5318–5320, 2008.

[17] J. Bisquert and V. S. Vikhrenko. Interpretation of the time constants measured by kinetic techniques in nanostructured semiconductor electrodes and dye-sensitized solar cells. *Journal of Physical Chemistry B*, 108:82313–2322, 2004.

[18] M. Wang, P. Chen, R. Humphry-Baker, et al. The influence of charge transport and recombination on the performance of dye-sensitized solar cells. *Journal of Chemical Physics and Physical Chemistry*, 10:290, 2009.

[19] J. Bisquert, D. Cahen, G. Hodes, et al. Physical chemical principles of photovoltaic conversion with nanoparticulate, mesoporous dye-sensitized solar cells. *Journal of Physical Chemistry B*, 108:8106–8118, 2004.

[20] M. Wang, X. Li, H. Lin, et al. Passivation of nanocrystalline TiO$_2$ junctions by surface adsorbed phosphinate amphiphiles enhances the photovoltaic performance of dye sensitized solar cells. *Dalton Transactions*, pages 10015–10020, 2009.

[21] Q. Wang, Z. Zhang, S. M. Zakeeruddin, and M. Grätzel. Enhancement of the performance of dye-sensitized solar cell by formation of shallow transport levels under visible light illumination. *Journal of Physical Chemistry B*, 112:7084–7092, 2008.

[22] Juan Bisquert. Theory of the impedance of electron diffusion and recombination in a thin layer. *Journal of Physical Chemistry B*, 106:325–333, 2002.

[23] C. Y. Chen, M. Wang, J. Y. Li, N. Pootrakulchote, et al. Highly efficient light-harvesting ruthenium sensitizer for thin-film dye-sensitized solar cells. *ACS Nano*, 3:3103–3109, 2009.

[24] Laurence Peter. Sticky electrons transport and interfacial transfer of electrons in the dye-sensitized solar cell. *Accounts of Chemical Research*, 42:1839–1847, 2009.

Chapter 5

Effect of Carbazole moieties

5.1 Introduction

In Dye-sensitized solar cells (DSC), the dye molecule (sensitizer) self-assembled onto the surface of wide-band gap semiconductor, TiO_2 , plays a vital role in the light-harvesting, charge separation, and overall photon-to-current conversion efficiency of the devices. Under illumination, ultra-swift electron injection from photoexcited sensitizers into the conduction band of the semiconductor occurs and the hole in the dye is regenerated sequentially by electron donation from the redox electrolyte. Numerous efforts focused on optimizing the molecular structures of the sensitizers and modulating the composition of electrolytes have been made to enhance the photovoltaic performance and improve the durability of the devices. [1–4] Among numerous dyes designed for DSCs, the ruthenium-based sensitizers incorporating thiophene derivatives have been proven to be excellent candidates to realize highly efficient and robust devices. [5–12] In addition, another new branch of heteroleptic ruthenium sensitizers endowed with the ancillary ligand consisting of a conjugated bridge and a hole-transporting terminal have been developed toward enriching the light-capturing ability to match the solar radiation and retarding the charge recombination between the dye-sensitized n-type semiconductor and electrolyte.

Recently, the efficient ruthenium sensitizer endowed with the ancillary ligand consisting of a conjugated segment and a carbazole unit has been found to enhance the spectral response and therefore the conversion efficiency of the DSCs based on it. [13] However, the long-term stability of cells based on the ruthenium dyes incorporating hole-transporting

moieties such as carbazole has not been reported so far. To further improve the light
harvesting capacity of this class of sensitizers and at the same time test the merit of
the carbazole-containing ruthenium dyes, we present in this chapter two new ruthenium
sensitizers; coded **B12** [14] and **B13** [15], featuring carbazole derivatives as the molec-
ular terminal of the ancillary ligands, bearing thieno[3,2-*b*]thiophene and ethylenedioxy-
thiophene (EDOT) as a π-bridge, respectively. The molecular structures of these two
sensitizers are shown in figure 5.1 (See Appendix A). The photovoltaic performance of
these novel sensitizers in DSCs at different aspects was investigated.

(a) B12   **(b) B13**
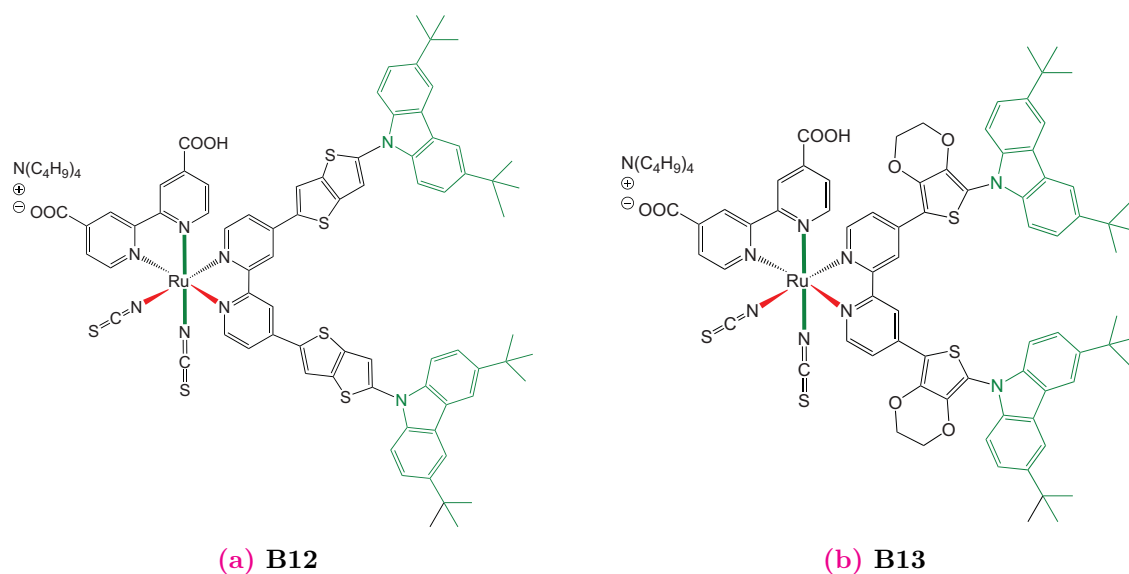
Figure 5.1: Molecular structures of sensitizers **B12** and **B13**.

5.2   Photophysical and electrochemical studies

The electronic absorption spectrum of **B12** measured in DMF is displayed in figure 5.2a.
B12 exhibits intense absorption bands centered at 393 and 555 nm, respectively. The
band at 393 nm is assigned to the overlap of π-π* transitions of the ancillary ligand
and one of the MLCT bands for **B12**. Another peak with λ_{max} at 555 nm and molar
absorption coefficient (ϵ) of 2.24×10^4 M^{-1} cm^{-1} is attributed to the characteristic MLCT
transition which is effective in charge generation by visible light in the devices sensitized
by **B12**. To gain more insights into these absorption bands of **B12** and to investigate the
position of tetrabutylammonium (TBA) cation, the time-dependent density functional
theory (TD-DFT) calculation of the singlet-singlet electronic transition for **B12(a)** and
B12(b) were performed based on the corresponding optimized geometry calculated at

the B3LYP/DGDZVP level, and the calculated absorption spectra are also presented in figure 5.2a. The experimental and TD-DFT calculated absorption spectra of **B12** in DMF show a good match based on the excitation energy. The calculated absorption profile of **B12(a)** and **B12(b)** are both close to the experimental result. Given the broad features of **B12** absorption band, it is difficult to attribute a specific TBA docking site. Therefore TBA cation may be either on the pyridine trans to NCS group (**B12(a)**) or pyridine trans to pyridine (**B12(b)**) when **B12** is dissolved in DMF. The location of cation in monoprotonated heteroleptic ruthenium sensitizers may be different at various solvent environment.

Figure 5.2b illustrates the electronic absortption spectra of **B13**, its anchoring and ancillary ligands measured in DMF. **B13** shows three absorption bands centered at 295 nm, 397 and 547 nm, respectively. The band at 295 nm is assigned to the overlap of intraligand π-π^* transitions of 4,4′-dicarboxylic acid-2,2′-bipyridyl anchoring ligand (dcbpy) and that of the ancillary ligand. [16] Another band centered at 397 nm also contains two components: the π-π^* transition of ancillary ligand and one of the metal-to-ligand charge transfer (MLCT) transitions for **B13**. The molar absorption coefficient (ϵ) of lower energy MLCT band centered at 547 nm is 1.93×10^4 M^{-1} cm^{-1}. This significant augmentation of the MLCT absorption cross section is due to the dioxyethylene pendent group of EDOT increasing both the electron donating ability and extension of π-conjugation to the thiophene moiety. [17]

Comparing the absorption profile of **B12** with that of **B13**, we find that the lower-energy MLCT band of **B12** slightly red-shifted and the corresponding ϵ value increased. These results indicate that the thieno[3,2-b]thiophene is a superior spacer in reinforcing the light-harvesting ability of ruthenium sensitizers.

The energy levels of the ground and excited states for **B12** and **B13** were estimated by square-wave voltammetry in combination with the optical transition energy, E_{0-0} determined from the absorption onset. These values are important to understand whether there is enough driving force to inject electrons into the TiO$_2$ conduction band and to regenerate the neutral dye by electron donation from the redox electrolyte present in the cell. The oxidation potentials of **B12** and **B13** are 0.98 V vs NHE (-5.48 eV vs vacuum) and 0.94 V vs NHE (-5.44 eV vs vacuum), respectively, which are 0.54–0.58 V more positive than the redox potential of the iodide/triiodide couple used in the electrolyte. The optical transition energy, E_{0-0} for **B12** and **B13** are both 1.58 eV. By neglecting the entropy changes during excitation, the excited-state redox potentials, $\phi^0(\text{S}^+/\text{S}^*)$ are
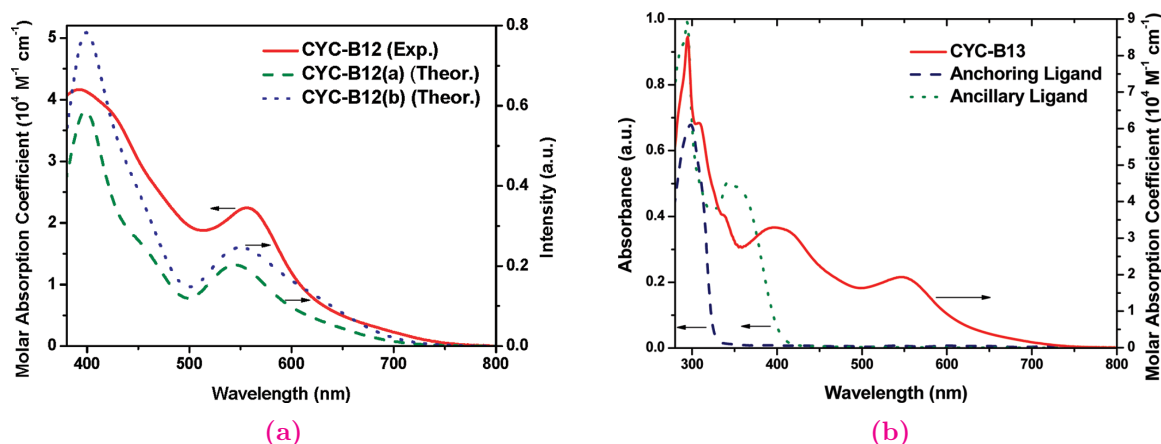
Figure 5.2: Experimental electronic absorption spectra measured in DMF of (a) **B12** in comparison with theoretical ones; **B12(a)** and **B12(b)**, obtained by Gaussian convolution with $\sigma = 0.15$ eV, and (b) **B13** with those of its anchoring and ancillary ligands.

-0.60 and -0.64 V vs NHE (-3.90 and -3.86 eV vs vacuum) for **B12** and **B13**, respectively, which is more negative than the potential (ca. 0.50 V vs NHE) of the TiO_2 (anatase) conduction band edge. These results clearly show that the energy levels of the ground and excited states for **B12** and **B13** match well the energetic requirements of a sensitizer for efficient charge generation in DSCs. [4] Thus upon photoexcitation, **B12** and **B13** self-assembled onto the TiO_2 film can inject electrons into the TiO_2 conduction band and then the reduction of oxidized **B12** and **B13** by the electrolyte will occur spontaneously in this regenerative photovoltaic devices.

5.3 Photovoltaic performance

In DSC devices, thicker TiO_2 films have higher surface area and thus enhancing the light-harvesting efficiency of dye-sensitized TiO_2 films, increasing the short-circuit photocurrent density (J_{sc}). However, the open-circuit photovoltage (V_{oc}) decreases with increasing the film thickness, due to higher surface area increases also the undesired dark current (due to an increase of surface trap states). Hence, initially the 3 μm thin TiO_2 films were used to fabricate DSC test devices, taking the advantage of the high optical cross section of **B12** and **B13** compared to standard **Z907** sensitizer. [18] All these test devices are employed with Z946 electrolyte (see section EL) and Appendix B. The characteristic J-V curves of the devices sensitized with **B12**, **B13** and **Z907** are displayed in figure 5.3a. Encouragingly, even with such thin titania film and low-volatile electrolyte, devices based

on **B12** in the presence of DINHOP [19] as a coadsorbent (4:1 molar ratio in the dye solution) provides a J_{sc} of 11.8 mA cm^{-2}, a V_{oc} of 0.733 V and a FF of 0.71, yielding an overall power conversion efficiency (η) of 6.2% under illumination with standard AM 1.5 G simulated sunlight (100 mW cm^{-2}). Similarly, device based on **B13** provides a J_{sc} 11.9 mA cm^{-2}, a V_{oc} of 0.734 V and a FF of 0.69 and η 6.1%. Under the same conditions, the η of **Z907** sensitized cell is only 5.3%. The detailed photovoltaic parameters of devices are summarized in table 5.1. The major difference in the photovoltaic performance is the J_{sc}, which was further verified from the IPCE spectra illustrated in figure 5.3b. This arises from the higher peak molar apsorption coefficient of **B12** and **B13** compared to that of **Z907** (see Appendix A) and a red-shift in the absorption.
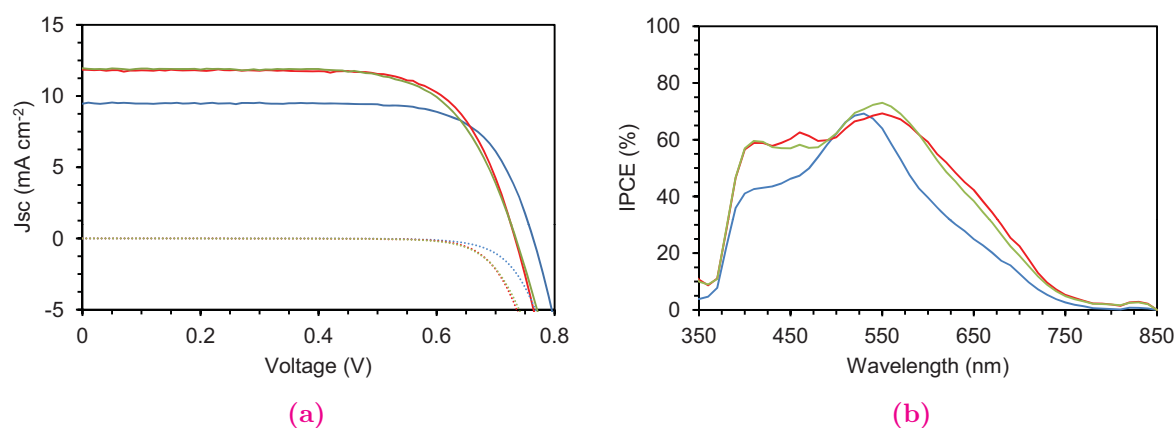
Figure 5.3: (a) *J-V* characteristic curves under full sunlight (AM 1.5 G, 100 mW cm^{-2}) of devices based on **B12** (red), **B13** (green) compared with **Z907** (blue); in combination with the low-volatile electrolyte, Z946. (b) The corresponding IPCE spectra of the same devices. (TiO$_2$ film thickness = 3 μm, cell active area tested with a mask: 0.159 cm^2.)

For further investigating the potential of **B12** and **B13** sensitizers, a device based on **B12** employed a double layer TiO$_2$ film (7+5 μm) and the low-volatile electrolyte, Z946, was also fabricated and its *J-V* characteristic curve is displayed in figure 5.4a The photovoltaic parameters are J_{sc} = 16.3 mA cm^{-2}, V_{oc} = 0.705 V and FF = 0.70, as summarized in table 5.1, yielding the PCE of 8.2%. The corresponding IPCE spectrum is shown in figure 5.4b which exhibits a plateau of over 70% from 450 to 670 nm, with the maximum of 81% at 570 nm. On the other hand the efficiency for **Z907** sensitized device fabricated with the same procedures is 7.9% [20] (See table 5.1). The higher J_{sc} for **B12** based device (compared to that sensitized with **Z907**) is mainly due to the higher light absorption capacity of **B12**. As expected, the J_{sc} for thick film device (7+5 μm) is also higher than that for the thin film device (3 μm). However, **B12** yields a 58 mV lower V_{oc} than **Z907**, indicating a faster interfacial electron recapture by triiodide with

Sensitizer	TiO$_2$ film thickness (μm)	Electrolyte	V_{oc} (mV)	J_{sc} (mA cm^{-2})	FF	η (%)
B12	3	Z946	733	11.8	0.71	6.2
B13	3	Z946	734	11.9	0.69	6.1
Z907	3	Z946	763	9.5	0.74	5.3
B12	7 + 5	Z946	705	16.3	0.70	8.2
B13	8 + 5	Z946	713	16.1	0.72	8.3
Z907	7 + 5	Z946	763	14.8	0.70	7.9
B12	7 + 5	Z960	703	17.9	0.74	9.4
B13[a]	8 + 5	Z960[b]	760	17.1	0.73	9.6

[a]a chenodeoxycholic acid (Cheno, see section 2.1.6) was used as coadsorbent (1:1 molar ratio in chlorobenzene)
[b]with reduced iodide content from 0.03 M to 0.02 M. See Appendix B.

Table 5.1: Detailed photovoltaic parameters of **B12**, **B13** and **Z907**-sensitized devices with various TiO$_2$ film thickness and various electrolytes, using DINHOP as coadsorbent, measured under AM 1.5 G simulated sunlight (100 mW cm^{-2}).

the former compared to the latter device. This might be caused by the lower **B12** loading and therefore more naked TiO$_2$ surface might be exposed to the electrolyte. To prove this supposition, the dye loading of both **B12** and **Z907** on 8 μm thick transparent TiO$_2$ film was measured. It was found that the amount of **B12** dye (2.31×10^8 mol) on the surface of TiO$_2$ is almost two times lower than that of **Z907** (4.18×10^8 mol), which accounts for the lower V_{oc} value of device sensitized by **B12**.

The J-V curve for device with a standard volatile electrolyte (Z960) is also displayed in figure 5.4a, providing a J_{sc} of 17.9 mA cm^{-2}, a V_{oc} of 0.703 V and a FF of 0.74, yielding a high conversion efficiency of 9.4%. The corresponding IPCE spectrum presented in figure 5.4b shows a plateau of over 80% from 460 to 620 nm with the maximum of 88% at 560 nm. The difference in J_{sc} in figure 5.4a can be rationalized in terms of the physical diffusion of iodide/triiodide in the electrolyte. [3, 21]

In general, a faster transportation of iodide/triiodide can be achieved in a higher volatile electrolyte. Z960 electrolyte has lower viscosity and lower concentration of triiodide compared to Z946 electrolyte. Electrolyte with low viscosity and triiodide concentration benefits the dye regeneration and the charge carrier collection efficiency. [21, 22] It is also known that the V_{oc} of a DSC is determined intrinsically by the potential difference between the quasi-Fermi level of the semiconductor (TiO$_2$) and the redox potential of the

hole-conductor (or electrolyte). Nevertheless, the V_{oc} will be affected by a shift of TiO_2 conduction band edge [23] as well as the degree of electron recombination. [24, 25]
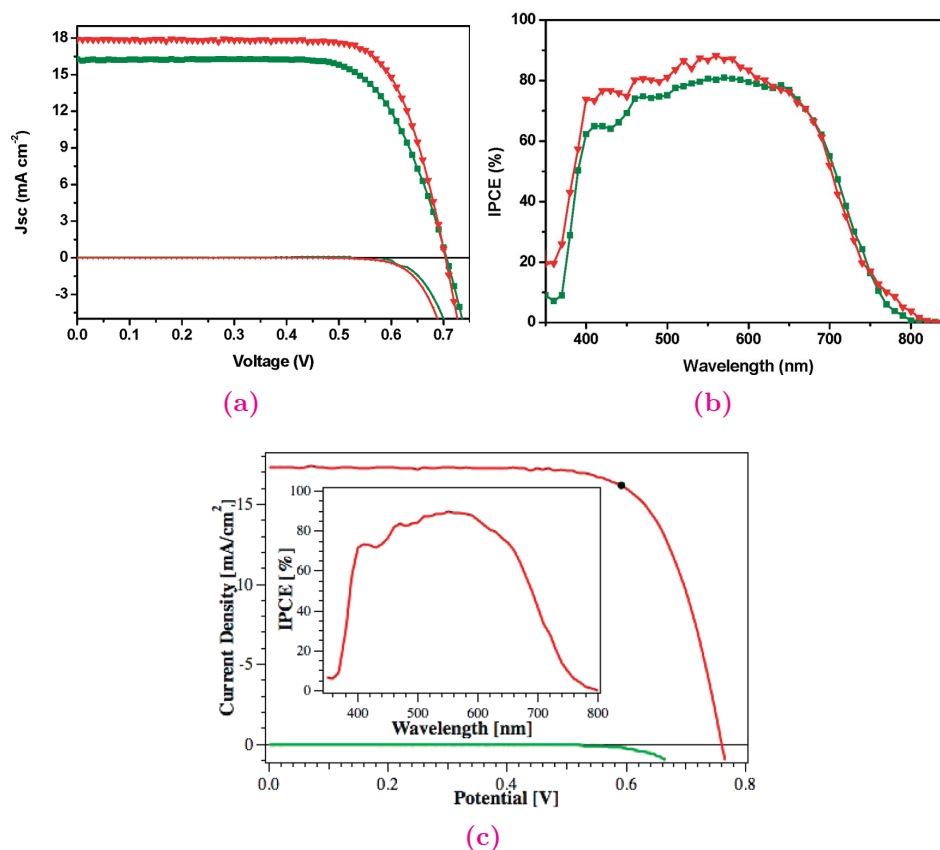
Figure 5.4: (a) J-V characteristic curves of DSC devices sensitized with **B12** conjunction with Z946 (green) and Z960 (red), respectively, measured in the dark and under AM 1.5 G simulated sunlight illumination (100 mW cm^{-2}).(b) The corresponding IPCE action spectra of devices. (Thickness of TiO2 film: 7+5 μm; cell active area tested with a mask: 0.158 cm^2.) (c) J-V characteristic curves of DSC devices sensitized with **B13** in corporate with volatile electrolyte, measured under the same condition. The inset is its IPCE action (Thickness of TiO2 film: 8+5 μm; cell active area tested with a mask: 0.158 cm^2.)

Similarly, a device based on **B13** using a double layer TiO_2 film (8+5 μm) and a low-volatile electrolyte (Z946) provides J_{sc} = 16.1 mA cm^{-2}, V_{oc} = 0.713 V and FF= 0.72, as summarized in table 5.1, yielding the η of 8.3%. On the other hand, a more efficient **B13**-based device employed a double layer TiO_2 film (8+5 μm), chenodeoxycholic acid as coadsorbent (1:1 molar ratio in chlorobenzene) and an acetonitrile-based volatile electrolyte were also fabricated. The IPCE spectrum shown in the inset of figure 5.4c exhibits a plateau of over 80% from 455 to 620 nm, with the maximum of 90% at 550 nm. The corresponding J-V characteristic curve of the solar cell under illumination with

standard AM 1.5 G simulated sunlight is also displayed in figure 5.4c. The photovoltaic parameters are summarized in table 5.1; $J_{sc} = 17.1$ mA cm^{-2}, $V_{oc} = 0.760$ V and $FF =$ 0.73, yielding an overall conversion efficiency (η) of 96%. The J_{sc} agrees with the value of 17.3 mA cm^{-2} calculated from the overlap integral of the IPCE spectrum with standard AM 1.5 G solar emission spectrum, showing that the spectral mismatch is less than 2%.

5.4   Long-term stability

In addition to the photon-to-current conversion efficiency, the stability of photovoltaic device is also a critical factor for the practical application. To demonstrate the durability of **B12** and **B13**, the devices based on **B12** and **B13** employed Z946 electrolytes, using double layer TiO$_2$ films, were subjected to the accelerated aging test performed under the illumination with the visible light (1 sun; 100 mW cm^{-2}) at 60 °C. As displayed in figure 5.5, the photovoltaic parameters J_{sc}, V_{oc}, FF, and η of the **B12**-based device slightly changed to 16.8 mA cm^{-2}, 0.676 V, 0.70, and 7.9%, respectively and the η retained 96% of its initial value after 1000 h of light soaking and thermal stressing. For **B13**-based device the values also change to 16.0 mA cm^{-2}, 0.673 V, 0.72, and 7.9%, respectively, the η retained 96% of its initial value (The initial values are listed in table 5.1). The preliminary results reveal that **B12** and **B13** can sustain excellent stability under prolonged light soaking at elevated temperatures. The thienothiophene-linked carbazole and the EDOT-linked carbazole moieties on **B12** and **B13**, respectively, not only can effectively prevent the desorption of the self-assembled dye molecules, induced by water during the accelerated aging process, but also can maintain the light-harvesting ability of the corresponding DSC device. Furthermore, by comparing the stability of the devices sensitized by **B12** and **B13**, it seems that having EDOT or thieno[3,2-b]thiophene as π-bridge in the ancillary ligand show little influence on the device stability.

To diagnose the changes of the photovoltaic parameters for the device during the long-term light-soaking and thermal stressing test, the transient photovoltage measurement was performed on the **B12**- and **B13**-based devices before and after aging. Figure 5.6a displays the open-circuit voltage as a function of the incident light intensity of the **B12**-sensitized device using Z946 electrolyte. Under the same light intensity, the V_{oc} decreases upon aging, indicating that after light soaking, the conduction band edge of TiO$_2$ may undergo a downward shift (to more positive potential), resulting in slightly decreasing the open circuit voltage. This scenario has been observed previously in DSCs, was attributed
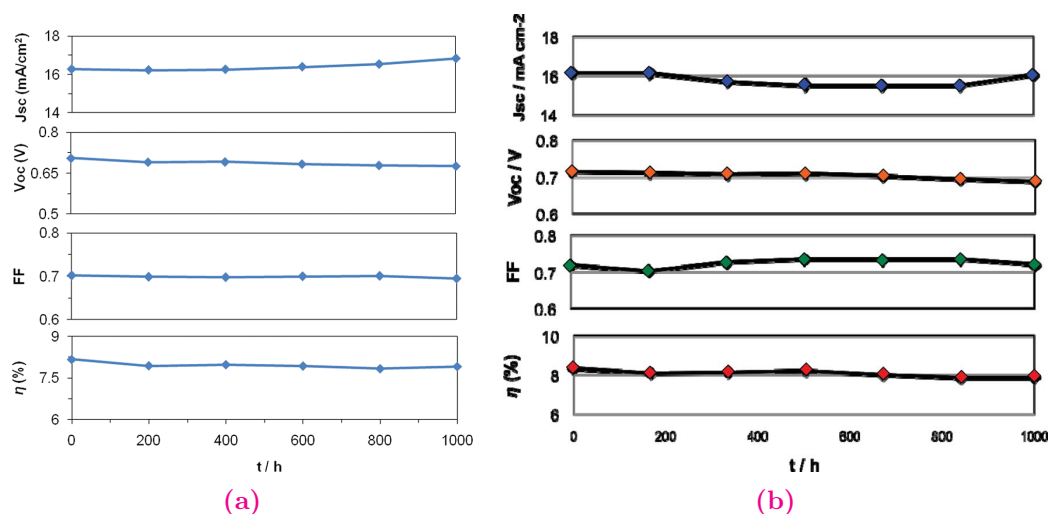
Figure 5.5: Evolution of the photovoltaic parameters (J_{sc}, V_{oc}, FF, and η) for devices sensitized with (a) **B12** and (b) **B13**, in combination with a low-volatile electrolyte (Z946) during the visible light-soaking (1 sun; 100 mW cm^{-2}) at 60 °C.

to the photoinduced proton intercalation of the titania. [26] To clarify the V_{oc} degrading mechanism upon aging, the transient photoelectrical studies were performance and the results are displayed in figure 5.6b and 5.6c. The chemical capacitance (C_μ) for both fresh and aged device increases exponentially with increasing light intensity. At the identical V_{oc}, the capacitance of the aged device is higher than that for the fresh one (figure 5.6b), revealing a larger density of surface trap states below the conduction band edge caused by 1000 h light soaking. Furthermore, at the same photoinduced charge density (1×10^{19} cm^{-3}, for example) the recombination lifetime (3.6 ms) for the aged device is significantly shorter than that (73.0 ms) of the fresh device as shown in figure 5.6c. In spite of this, the overall conversion efficiency for the aged device is close to that of the fresh device because the increase in charge recombination rate can be compensated by increasing the short-circuit current upon aging.

Similarly, the photovoltage transient measurements were also performed for both fresh and aged **B13**-based devices. Figure 5.7a displays the open-circuit voltage as a function of the photoinduced charge density accumulated in the TiO$_2$ nanoparticles at open-circuit condition. At identical photoinduced charge densities, the fresh cell shows higher V_{oc} compared to the aged cell. This result indicates that after light soaking, the conduction band edge of the TiO$_2$ in the aged device undergoes a downward shift (to more positive potentials), similar to that of **B12**-based device. However, from figure 5.7b we can see that at identical photoinduced charge densities, the recombination lifetime for the fresh and
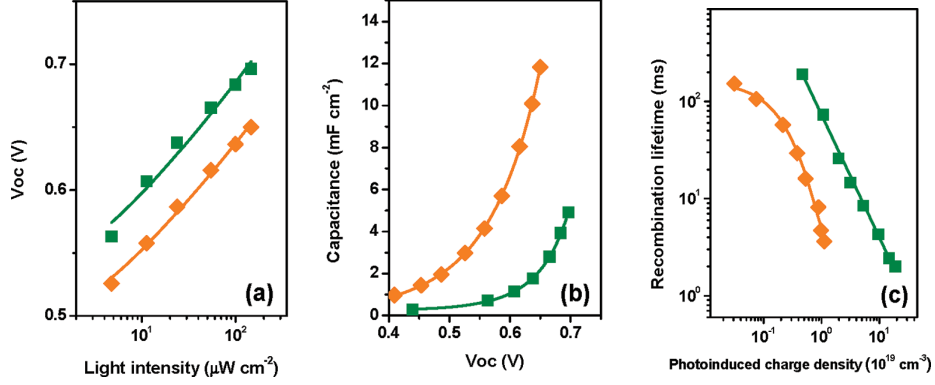
Figure 5.6: Transient photoelectrical measurements of the fresh and aged device sensitized with **B12** in conjunction with Z946 electrolyte. (a) Open-circuit voltage for devices as a function of incident light intensity. (b) Chemical capacitance (C_μ)of devices as a function of V_{oc}. (c) Recombination lifetime (τ_n) of device as a function of photoinduced charge density.

aged **B13**-based devices has similar values, revealing that no change in the distribution of the surface trap states or rate for interfacial charge recombination during the 1000 h light soaking test. The slight decrease in the efficiency after light-soaking and thermal stressing of **B13**-based device is mainly due to the change of V_{oc}.
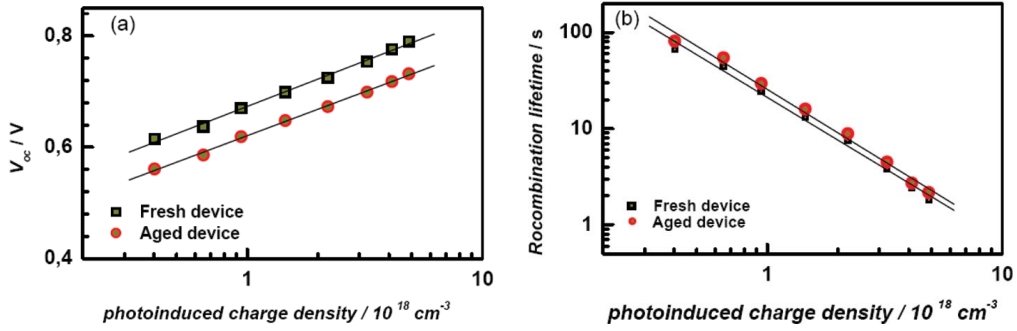
Figure 5.7: Transient photoelectrical measurements of the fresh and aged device sensitized with **B13** in conjunction with Z946 electrolyte: An effect of light soaking on the relationship between (a) photoinduced charge density and open-circuit voltage and (b) photoinduced charge density and recombination lifetime.

In addition, an electrochemical impedance spectroscopy (EIS) was also employed to examine the effect of light soaking on the photovoltaic performance of the **B13**-sensitized devices. Figure 5.8a depicts the Nyquist plots of the fresh and aged devices at a forward bias of -0.5 V. These spectra follow well the transmission line model suggested by Bisquert et al. [27] The EIS spectrum of the aged device shown in figure 5.8b displays a smaller electron transport resistance (R_t) in the nanocrystalline TiO_2 at high frequencies range (from

10 kHz to 200 Hz) compared to that for the fresh device. Under forward bias, electrons are transferred from the FTO substrate into the TiO$_2$ film, allowing electron propagation through the individual TiO$_2$ particles. The logarithm of the electron transport resistance, which depends on the number of free electrons (e_{cb}^-) in the TiO$_2$ conduction band, shows parallel behavior for various devices. This implies that the shift of the resistances for the steady state electron transport of those devices are caused by the displacement of the Fermi level for the electrons (E_{Fn}) with respect to the conduction band edge (E_{cb}). [28]

Figure 5.8: (a) Impedance spectra (Nyquist plot) of the fresh and aged devices at forward bias of -0.50 V under dark conditions at 20 °C. (b) The enlarge part of plot (a) in the high frequency range. The TiO$_2$ film was co-sensitized with **B13** and DINHOP (molar ratio 4:1). The solid line corresponds to the derived values using the fitting model.

Figure 5.9 illustrates the electron transport resistance (R_t) vs applied voltage for the TiO$_2$ film obtained from the impedance measurements in the dark at 20 °C. There is a small downward shift of the TiO$_2$ conduction band edge by about 20 mV for the aged device compared to that of the fresh device. As we did not observe a change in the diffusion and redox overpotentials of the electrolyte on the platinized counter electrode by impedance measurements, the decrease of open-circuit voltage of the aged device should be mainly related to surface protonation during the light-soaking period. This energy shift principally influenced the open-circuit voltage of the device. Both photovoltage transient and electrochemical impedance data suggest that **B13** is stable during the light soaking and thermal stressing treatments.

5.5   Conclusion

In summary, we report novel high light-harvesting ruthenium sensitizers, **B12** and **B13**, endowed with a new antenna consisting of the sequential connection of an electron-
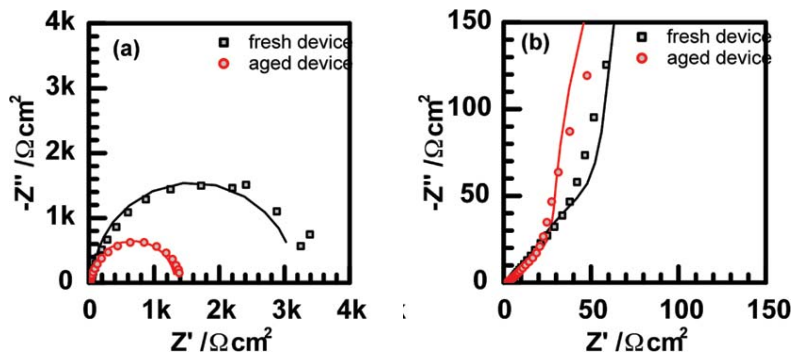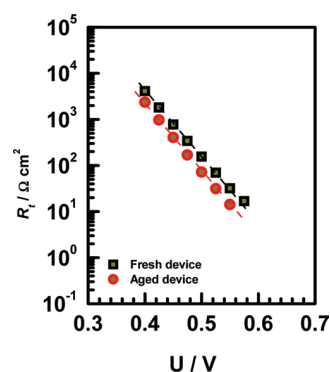
Figure 5.9: (a) Impedance spectra (Nyquist plot) of the fresh and aged devices at forward bias of -0.50 V under dark conditions at 20 °C. (b) The enlarge part of plot (a) in the high frequency range. The TiO$_2$ film was co-sensitized with **B13** and DINHOP (molar ratio 4:1). The solid line corresponds to the derived values using the fitting model.

rich thienothiophene- and EDOT-conjugated bridge, respectively, together with carbazole hole-transport moiety. DSCs based on these new sensitizers with a volatile liquid electrolyte exhibits a 9.4% and 9.6% conversion efficiency under AM 1.5 G sunlight for **B12** and **B13**, respectively. Excellent cells stability under prolonged light soaking and thermal stressing are also demonstrated with a low-volatility liquid electrolyte. The physicochemical data clearly prove that both are good sensitizers for efficient and robust DSCs. In addition, the transient photoelectrical analysis for the fresh and aged devices suggests that the both carbazole-containing sensitizers are stable under the light soaking and thermal stressing treatments. For **B12**, the transient measurement also indicates that the variation in the electron recombination lifetime, due to the change in the triiodide concentration, is the main reason for the divergence of the cell performance.

Bibliography

[1] A. Mishra, M. K. R. Fischer, and P. Bäuerle. Metal-free organic dyes for dye-sensitized solar cells: From structure: Property relationships to design rules. *Angewandte Chemie*, 48:2474–2499, 2009.

[2] A. Hagfeldt, G. Boschloo, L. Sun, et al. Dye-sensitized solar cells. *Chemical Reviews*, 110:6595–6663, 2010.

[3] S. M. Zakeeruddin and M. Grätzel. Solvent-free ionic liquid electrolytes for mesoscopic dye-sensitized solar cells. *Advanced Functional Materials*, 19:2187–2202, 2009.

[4] Michael Grätzel. Recent advances in sensitized mesoscopic solar cells. *Accounts of Chemical Research*, 42:1788–1798, 2009.

[5] C. Y. Chen, H. G. Lu, C. G. Wu, et al. New ruthenium complexes containing oligoalkylthiophene-substituted 1,10-Phenanthroline for nanocrystalline dye-sensitized solar cells. *Advanced Functional Materials*, 17:29–36, 2007.

[6] C.Y. Chen, S. J. Wu, C. G. Wu, et al. A ruthenium complex with superhigh light-harvesting capacity for dye-sensitized solar cells. *Angewandte Chemie*, 118:5954–5957, 2006.

[7] C. Y. Chen, M. Wang, J. Y. Li, N. Pootrakulchote, et al. Highly efficient light-harvesting ruthenium sensitizer for thin-film dye-sensitized solar cells. *ACS Nano*, 3:3103–3109, 2009.

[8] D. Shi, N. Pootrakulchote, R. Li, et al. New efficiency records for stable dye-sensitized solar cells with low-volatility and ionic liquid electrolytes. *Journal of Physical Chemistry C*, 112:17046–17050, 2008.

[9] F. Sauvage, M. K. R. Fischer, A. Mishra, et al. A dendritic oligothiophene ruthenium sensitizer for stable dye-sensitized solar cells. *Chemistry and Sustainability Energy and Materials* (CHEMsusCHEM), 2:761–768, 2009.

[10] Y. Cao, Y. Bai, Q. J. Yu, et al. Dye-sensitized solar cells with a high absorptivity ruthenium sensitizer featuring a 2-(hexylthio)thiophene conjugated bipyridine. *Journal of Physical Chemistry C*, 113:6290–6297, 2009.

[11] A. Abbotto, C. Barolo, L. Bellotto, et al. Electron-rich heteroaromatic conjugated bipyridine based ruthenium sensitizer for efficient dye-sensitized solar cells. *Chemical Communications*, pages 5318–5320, 2008.

[12] S. Liu Q. J. Yu, M. Zhang, et al. An extremely high molar extinction coefficient ruthenium sensitizer in dye-sensitized solar cells: The effects of π-conjugation extension. *Journal of Physical Chemistry C*, 113:14559–14566, 2009.

[13] C. Y. Chen, J. G. Chen, S. J. Wu, et al. Multifunctionalized ruthenium-based supersensitizers for highly efficient dye-sensitized solar cells. *Angewandte Chemie*, 47:7342–7345, 2008.

[14] C. Y. Chen, N. Pootrakulchote, T.-H. Hung, et al. Ruthenium sensitizer with thienothiophene-linked carbazole antennas in conjunction with liquid electrolytes for dye-sensitized solar cells. *Journal of Physical Chemistry C*, 115:20043–20050, 2011.

[15] C. Y. Chen, N. Pootrakulchote, S.-J. Wu, et al. New ruthenium sensitizer with carbazole antennas for efficient and stable thin-film dye-sensitized solar cells. *Journal of Physical Chemistry C*, 113:20752–20757, 2009.

[16] V. Balzani, A. Juris, and M. Venturi. Luminescent and redox-active polynuclear transition metal complexes. *Chemical Reviews*, 96:759–833, 1996.

[17] C.Y. Chen, S. J. Wu, J.-Y. Li, et al. A new route to enhance the light-harvesting capability of ruthenium complexes for dye-sensitized solar cells. *Advanced Materials*, 19:3888–3891, 2007.

[18] P. Wang, C. Klein, R. H. Baker, et al. A high molar extinction coefficient sensitizer for stable dye-sensitized solar cells. *Journal of the American Chemical Society*, 127:808–890, 2005.

[19] M. Wang, X. Li, H. Lin, et al. Passivation of nanocrystalline TiO_2 junctions by surface adsorbed phosphinate amphiphiles enhances the photovoltaic performance of dye sensitized solar cells. *Dalton Transactions*, pages 10015–10020, 2009.

[20] C. Barolo, Md. K. Nazeeruddin, S. Fantacci, et al. Synthesis, characterization, and DFT-TDDFT computational study of a ruthenium complex containing a functionalized tetradentate ligand. *Dalton Transactions*, 45:4642–4653, 2006.

[21] Z. Zhang, S. Ito, J.-E. Moser, et al. Influence of iodide concentration on the efficiency and stability of dye-sensitized solar cell containing non-volatile electrolyte. *Journal of Chemical Physics and Physical Chemistry*, 10:1834–1838, 2009.

[22] G. Boschloo and A. Hagfeldt. Characteristics of the iodide/triiodide redox mediator in dye-sensitized solar cells. *Accounts of Chemical Research*, 42:1819–1826, 2009.

[23] Z. Zhang, S. M. Zakeeruddin, B. C. O'Regan, et al. Influence of 4-guanidinobutyric acid as coadsorbent in reducing recombination in dye-sensitized solar cells. *Journal of Physical Chemistry B*, 109:21818–21824, 2005.

[24] A. Reynal, A. Forneli, E. Martinez-Ferrero, et al. Interfacial charge recombination between electron-and the iodide/triiodide electrolyte in ruthenium heteroleptic complexes: Dye molecular structure vs open circuit voltage relationship. *Journal of the American Chemical Society*, 130:13558–13567, 2008.

[25] B. C. O'Regan, K. Walley, M. Juozapavicius, et al. Structure/function relationships in dyes for solar energy conversion: A two-atom change in dye structure and the

mechanism for its effect on cell voltage. *Journal of the American Chemical Society*, 131:3541–3548, 2009.

[26] Q. Wang, Z. Zhang, S. M. Zakeeruddin, and M. Grätzel. Enhancement of the performance of dye-sensitized solar cell by formation of shallow transport levels under visible light illumination. *Journal of Physical Chemistry B*, 112:7084–7092, 2008.

[27] J. Bisquert, D. Cahen, G. Hodes, et al. Physical chemical principles of photovoltaic conversion with nanoparticulate, mesoporous dye-sensitized solar cells. *Journal of Physical Chemistry B*, 108:8106–8118, 2004.

[28] M. Wang, P. Chen, R. Humphry-Backer, et al. The influence of charge transport and recombination on the performance of dye-sensitized solar cells. *Journal of Chemical Physics and Physical Chemistry*, 10:290–299, 2009.

Chapter 6

Effect of Triazole moieties

6.1 Introduction

As we have discussed in previous chapters, the ruthinium sensitizers play an important role in DSCs as they absorb sunlight and induce intramolecular charge transfer from the ancillary ligand to the anchoring ligand with subsequent electron injection into the TiO_2 semiconductor. In this respect, numerous reports about bipyridine-Ru(II) sensitizers which, for example, were functionalized with either hydrophobic chains to improve the device stability or with elongated π-conjugated systems to enhance absorption, have been published. [1–7] In general, bi- and terpyridines (bpy and terpy) are the most frequently investigated ligands for ruthenium(II) complexes. [8–10]

It has been long investigated that hydrophobic substituents such as alkyl chains in the standard sensitizer **Z907** reduce the recombination reaction by hindering the triiodide present in the electrolyte to approach the semiconductor surface, thus, improve the device stability. Furthermore, polyethylene glycol (PEG) chains attached to sensitizers such as **K51**. [11] are able to coordinate lithium cations from the electrolyte which results in an improved current density and overall device performance.

In search of new ligands for Ru(II) dyes in DSCs, it is shown that pyridines can successfully be replaced by other N-containing ligands, for example, pyrazoles. [12,13] In a recent report, a "*click-chemistry*" approach was used to functionalize the periphery of an ancillary bipyridine-ligand in a Ru(II) sensitizer and the corresponding DSC device based on this sensitizer, using a volatile acetonitrile-based electrolyte, provided an overall

conversion efficiency of 6.75% [14] A click-chemistry tool; the Cu(I)-catalyzed alkyne-azide cycloaddition (CuAAC), first presented in 2001 , is a useful method to attach variety of substituents into ancillary ligands.

Here in this chapter, we propose a series of novel Ru sensitizers prepared by click-chemistry to functionalize the periphery of an ancillary bpy ligand with three different tri-azole derivatives; (a) with hexyl-triazolyl group, coded **R1**, (b) with hexylphenyl-triazolyl group, coded **R2** and 4-triethyleneglycol-substituted phenyl triazolyl group, coded **R3**. The molecular structures of these compounds are shown in figure 6.1. The complexes were incorporated and characterized in DSC test devices using volatile acetonitrile-based and solvent-free electrolytes.
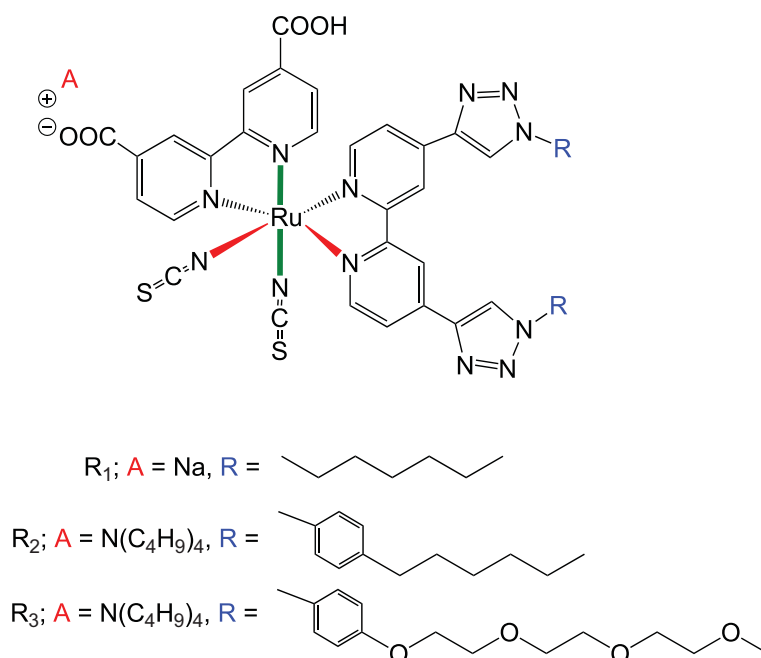
Figure 6.1: Molecular structures of sensitizers **R1**, **R2**, and **R3**.

Furthermore, growing interest in 1,2,3-triazolyl-derivatives as chelates has been long evolving. Very recently, several bi- and terdentate ligands such as (1,2,3-triazol-4-yl) pyridines [15–18], 2,6-bis(1,2,3-triazol-4-yl) pyridines [19], and 4,4′-bis(1,2,3-triazoles) [15] and their corresponding Ru(II) complexes were synthesized using click-chemistry. However, Ru(II) complexes in which 1,2,3-triazoles are used as chelating ligands are relatively little known and there are no examples reported up to now where 1,2,3-triazoles have been used as chelating ligands in Ru(II) sensitizers for solar cell applications.

In order to gain more insight into structure-property-device performance relation-

ships, we also propose here two more Ru sensitizers functionalized with chelating biden-
tate triazolyl-pyridine ligands; coded **R4** and **R5**. The molecular structures of these
compounds are shown in figure 6.2. The synthesis of these sensitizers was described else-
where. [20] The complexes were incorporated and characterized in DSC test devices using
a volatile electrolyte.

(a) **R4**   (b) **R5**
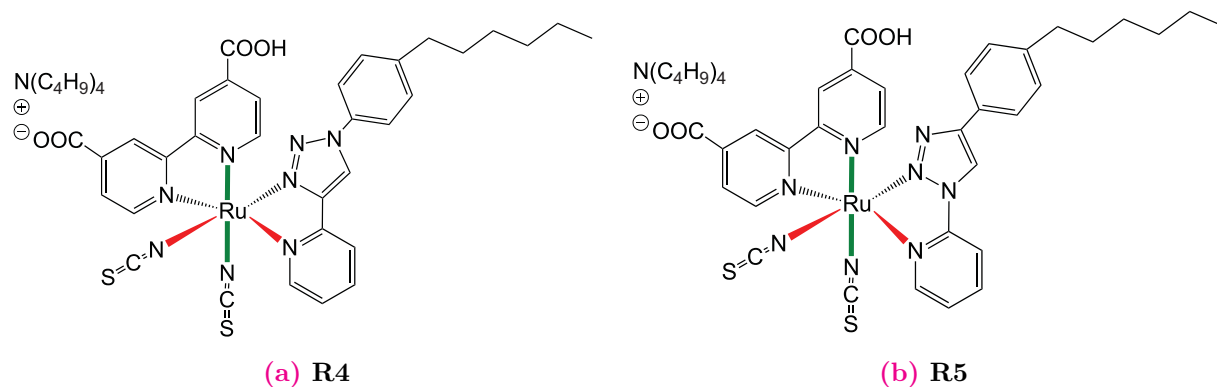
Figure 6.2: Molecular structures of sensitizers **R3**, **R4** and **R5**.

6.2   Photophysical and electrochemical studies

Absorption and emission spectra of sensitizers **R1**–**R5** are shown in figure 6.3 Those of
R1, **R2** and **R3** appear similar since the chromophore is basically the same in all three
complexes. They show broad absorption bands from the ultra-violet (UV) to the visible
(VIS) region up to 750 nm. The high energy absorption band around 310 nm can be
assigned to intraligand π-π^* transitions. The absorption bands at lower energy, in the
range of 350 to 750 nm, arise predominantly from MLCT transitions. The higher energy
MLCT absorption maxima are located in between 388 and 394 nm and the lower energy
MLCT absorption maxima in between 536 and 540 nm for all sensitizers. Thus, different
substituents, whether alkyl or aryl, attached to the triazolyl moieties cause only minor
shifts in the absorption spectra. This is in accordance with our expectations, because the
triazole unit is known to be a weak bridge for conjugated π-systems. [21] However, the
phenyl substituents seem to slightly increase the molar extinction coefficient (ϵ) over the
whole UV-VIS region. Phenyl-substituted **R2** and **R3** showed a very similar ϵ of 1.74 and
1.92×10^4 M^{-1} cm^{-1} for the higher energy MLCT band and 1.39 and 1.54×10^4 M^{-1} cm^{-1}
for the lower energy MLCT band. On the other hand, alkyl-substituted **R1** displayed a
lower ϵ of 1.41 and 1.19×10^4 M^{-1} cm^{-1} for the higher and lower energy MLCT band,

respectively. The molar extinction coefficient of **R1** is comparable to that of **Z907** (see Appendix A) whereas it is increased by about 0.2×10^4 M^{-1} cm^{-1} for the lowest energy MLCT band and about 0.6×10^4 M^{-1} cm^{-1} for the higher energy MLCT band of **R2** and **R3**. During our studies, Ko et al. independently reported the synthesis and performance of **R2** in DSCs [14]. They found a similar MLCT maxima at 388 and 529 nm and molar extinction coefficient of 1.61×10^4 M^{-1} cm^{-1} in ethanol solution.

Alkyl- and Phenyl-triazolyl functionalized sensitizers **R1**, **R2** and **R3** showed an un-structured emission band at 762, 788 and 797 nm, respectively, which was assigned to triplet MLCT emission. The difference of the lowest energy MLCT absorption and the emission maximum for **R1**, **R2** and **R3** are 5533, 5863 and 5971 cm^{-1}, respectively.
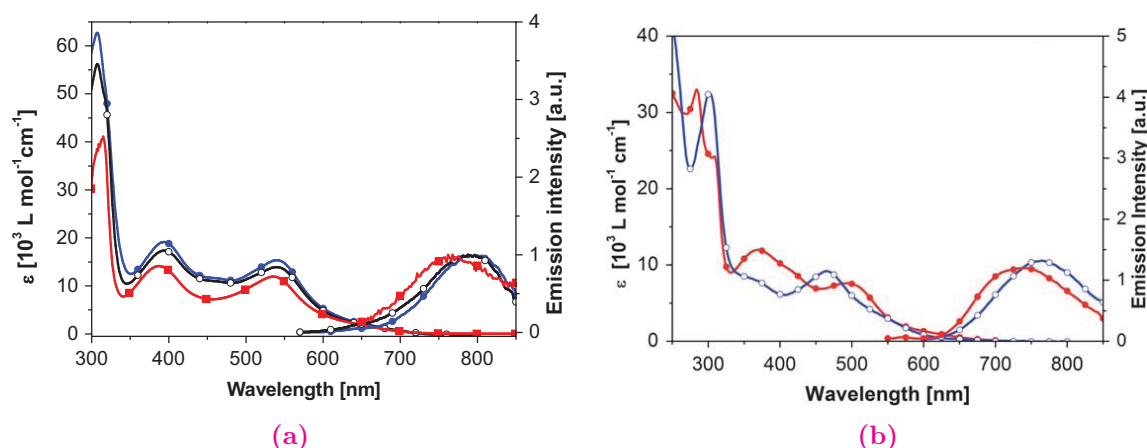
Figure 6.3: (a) UV-VIS spectra of **R1** (red), **R2** (black) and **R3** (blue) measured in DMF. Emission spectra were measured in aerated DMF solution with c ~10^{-5} M^{-1} (λ_{ex} = 540 nm). (b) UV-VIS and normalized emission spectra of **R4** (red) and **R5** (blue), measured in acetonitrile. Emission spectra were measured in aerated acetonitrile solution with c ~10^{-5} M^{-1} (λ_{ex} = 480 nm).

Both **R4** and **R5** sensitizers show broad absorption from the UV region up to 650 nm. The high energy absorption band at 250-300 nm can be assigned to intraligand π-π^* transitions. Both dyes show two additional absorption bands at lower energies which can be attributed to MLCT transition. **R4** showed the lowest energy MLCT absorption band at 493 nm with a molar extinction coefficient of 7600 M^{-1} cm^{-1}, which is lower than the higher energy MLCT band(λ_{max} = 369 nm, ϵ = 12000 M^{-1} cm^{-1}). In contrast, **R5** showed the lowest energy MLCT band at 465 nm with a higher extinction coefficient of 92000 M^{-1} cm^{-1} than the higher energy MLCT band at 366 nm (ϵ = 8000 M^{-1} cm^{-1}). The lowest energy MLCT band of **R5** is blue-shifted by 30 nm compared to **R4**.

Sensitizer	λ_{abs}[nm] (ϵ [L mol^{-1} cm^{-1}])	λ_{em} [nm]	HOMO [eV]	LUMO [eV]	$\triangle E$ [eV]
R1	315 (41 100)	762	-5.26	-3.25	2.01
	388 (14 100)				
	536 (11 900)				
R2	307 (56 200)	788	-5.36	-3.36	2.00
	393 (17 400)				
	539 (13 900)				
R3	307 (62 700)	797	-5.32	-3.34	1.98
	394 (19 200)				
	540 (15 400)				
R4	284 (30 000)	738	-5.23	-3.11	2.12
	369 (12 000)				
	493 (7 600)				
R5	302 (32 500)	765	-5.28	-3.09	2.19
	366 (8 000)				
	465 (9 200)				

Table 6.1: Photophysical and electrochemical data of complexes **R1**–**R3**. The λ_{abs} and λ_{em} were measured in DMF solution and acetonitrile solution for **R1**–**R3** and **R4**–**R5**, respectively. (HOMO-LUMO vs Fc/Fc$_{vac}^{+}$ = -5.1 eV).

Emission maxima of **R4** and **R5** are found at 738 and 765 nm, respectively, when excited at 480 nm, in the region of the lowest energy MLCT absorption. A large Stoke's shift was observed for both **R4** (6734 cm^{-1}) and **R5** (8433 cm^{-1}), which is an indication of significant structural changes between the ground and excited state. Similar to the absorption spectra, the emission bands are also blue-shifted compared to bipyridine-based Ru(II) complexes.

The HOMO energy levels for **R1**–**R5** complexes determined from the onsets of the oxidation waves lay in the range between -5.23 to -5.36 eV vs vacuum. The LUMO energy levels calculated from the onset of the reduction waves were in between -3.09 and -3.36 eV vs vacuum. The results showed that the attachment of different substituents at the triazolyl unit have only a minor influence on the HOMO/LUMO energy levels. The calculated energy gap was found to be around 2.0 eV for all three complexes. A successful application of the sensitizers in DSCs requires a suitable alignment of the HOMO

levels with the potential of the redox mediator and the LUMO level with the conduction band potential of TiO_2 . In this case the HOMO levels of about -5.3 eV vs vacuum are sufficiently low compared to redox mediator iodide/triiodide (-4.8 eV), providing efficient dye regeneration. Similarly, the LUMO levels with -3.1 to -3.3 eV are sufficiently high for efficient electron transfer from the excited dye to the titanium dioxide semiconductor (-4.0 eV). Detailed of photophysical and electrochemical data are summarized in table 6.1.

6.3   Photovoltaic performance

In order to study the influence of differently "click"-functionalized substituents on the DSC device performance of **R1**–**R3**, photovoltaic experiments were conducted. The devices were fabricated using an 8+5 μm double layer TiO_2 film in conjunction with a standard volatile acetonitrile-based electrolyte Z960 (see section 2.2). The TiO_2 films were sensitized by dipping overnight in a 0.3 mM dye solution in the presence of DINHOP as coadsorbent (molar ratio 4:1). Figure 6.4 shows the photocurrent-voltage (J-V) characteristics of devices with **R1**, **R2**, and **R3**, using the above mentioned volatile electrolyte under standard AM 1.5 G sunlight (100 mW cm^{-2}). The short-circuit photocurrent density (J_{sc}), open-circuit voltage (V_{oc}) and fill factor (FF) of all three devices are tabulated in table 6.2. The overall conversion efficiency (η) of devices stained with **R1** reached as high as 9.9%. Using the same titania film and electrolyte, the η of devices using sensitizers **R2** and **R3** were 8.7% and 9.6%, respectively. All these devices have similar V_{oc} (0.74– 0.78 V) and FF(0.74–0.76 V) values, but due to the differences in the J_{sc} the η values vary. Even though the molar extinction coefficient of sensitizer **R1** is lower than that of **R2**, to our surprise the J_{sc} value of device **R1** is higher than device **R2**. However, the trend is followed as expected in case of sensitizer **R3**. This can also be verified from the corresponding incident-photon to current conversion efficiency (IPCE) spectra exhibited in figure 6.4b. The IPCE spectra of devices based on sensitizers **R1** and **R3** reached more than 80% over a wide spectral range from 480 to 630 nm. The increased J_{sc} value for dye **R3** is due to the higher IPCE response at the lower energy region reaching a maximum of 94% at 590 nm. Whereas in case of **R2**-based device the maximum IPCE reached a maximum of 78% at 540 nm, which is consistent with the lower J_{sc} value. The improved performance of dye **R3** compared to **R2** could be ascribed to the attachment of Li$^+$ co-ordinating triethylene glycol chains at the periphery of the dye molecule, which showed a significant increase in the J_{sc} value with a negligible effect on the V_{oc}. Similar increased

performance has already been reported for Li$^+$ coordinating sensitizer **K51** compared to non-ion coordinating sensitizer **Z907**. [11]

The use of dye **R2** in an acetonitrile-based electrolyte reported by Ko and co-workers resulted in a significantly lower J_{sc} and η of 12.55 mA cm^{-2} and 6.75% with a comparable IPCE (above 70%) [14]; the sharp contrast to our results might be due to the differences in the electrolyte and the co-adsorbent.

(a)   (b)
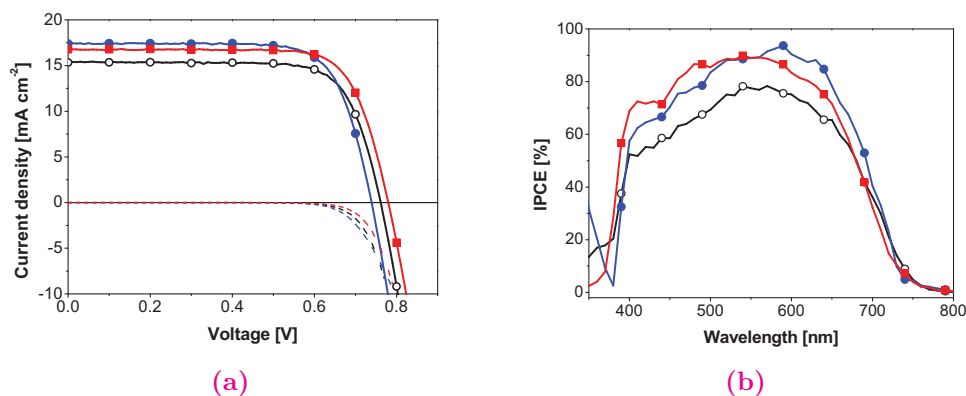
Figure 6.4: (a) *J-V* curves for devices sensitized with **R1** (red), **R2** (black) and **R3** (blue), using a double layered TiO$_2$ film (8+5 μm) and electrolyte Z960. Corresponding dark current curves given as dashed lines. The cell active area is 0.159 cm^2. (b) Corresponding IPCE spectra as a function of wavelength.

Sensitizer	Electrolyte	V_{oc} (V)	J_{sc} (mA cm^{-2})	FF	η (%)
R1	Z960	0.78	16.8	0.76	9.9
R2	Z960	0.76	15.3	0.75	8.7
R3	Z960	0.74	17.4	0.74	9.6
R1	Z952	0.69	13.4	0.76	7.1
R2	Z952	0.69	12.1	0.78	6.6
R3	Z952	0.68	12.8	0.77	6.7
R4	Z959	0.76	13.2	0.77	7.8
R5	Z959	0.67	8.9	0.77	4.7

Table 6.2: Detailed photovoltaic performances of devices sensitized with **R1**–**R5** under standard AM 1.5 G sunlight (100 mW cm^{-2}), using various electrolytes.

DSC devices sensitized with **R4** and **R5** were also fabricated using an 8+5 μm double layer TiO$_2$ film in conjunction with a volatile acetonitrile-based electrolyte Z959 (see

Appendix B for composition of this electrolyte), and DINHOP was also added as coadsorbent to the dye solution. The J-V curves and IPCE spectra of the devices are depicted in figure 6.5. Detailed photovoltaic parameters are summarized in table 6.2. The IPCE spectrum of **R4** covers a broad range from 380 to 700 nm, reaching its maximum of 77% at 500 nm, whereas the IPCE spectrum of **R5** is slightly blue-shifted with a maximum of 58% at 480 nm. Under full sunlight, the **R4**-based device exhibited V_{oc}, J_{sc}, FF and η of 761 mV, 13.2 mA cm^{-2}, 0.77 and 7.8%, respectively. On the other hand, a **R5**-based device gave a V_{oc} of 673 mV, J_{sc} of 8.9 mA cm^{-2}, and FF of 0.77, yielding a lower η of 4.7%.

(a)   (b)

Figure 6.5: (a) J-V characteristics under standard AM 1.5 G sunlight (100 mW cm^{-2}) and in the deark, and (b) corresponding IPCE spect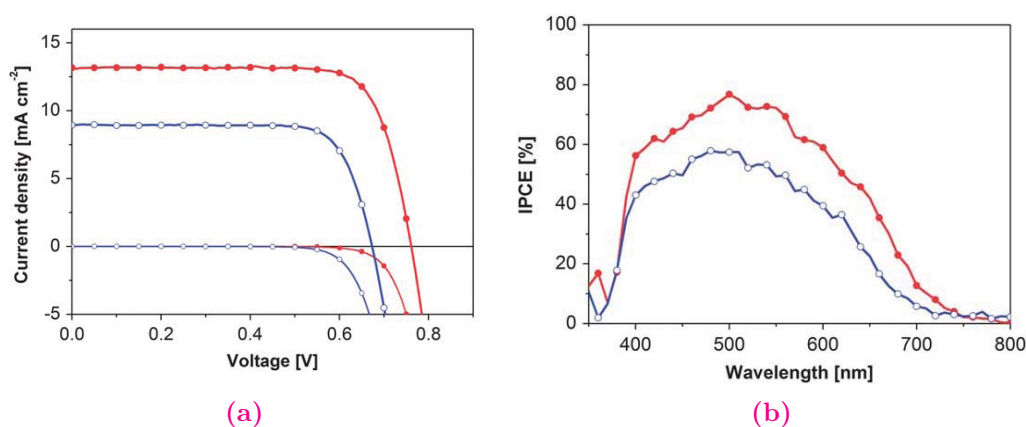ra for devices sensitized with **R4** (red) and **R5** (blue), using a double layered TiO$_2$ film (8+5 μm) and electrolyte Z959. The cell active area is 0.159 cm^2.

The power conversion efficiency of dye **R4** bearing the 1,2,3-triazol-4-yl ligand is superior to the 1,2,3-triazol-1-yl counterpart **R5** under similar conditions. Considering the lower molar extinction coefficient and the blue-shift in the absorption spectrum of **R4** compared to other bipyridine-based Ru(II) sensitizers, such as **Z907** [22], the device with a power conversion efficiency of 7.8% is quite impressive. The higher photocurrent density in the case of the **R4**-based device can be explained by an increase in the light absorbing capability of the **R4**-sensitized TiO$_2$ film. The higher V_{oc} in case of the **R4**-based device is due to either the reduction of charge recombination or the upward shift of the conduction-band edge position. In order to elaborate more on this assumption, transient photovoltage decay measurements were performed on these devices.

As shown in figure 6.6a, the structural differences of the two sensitizers have a significant effect on the photocurrent decay rate across the TiO$_2$ film and on the slope of decay
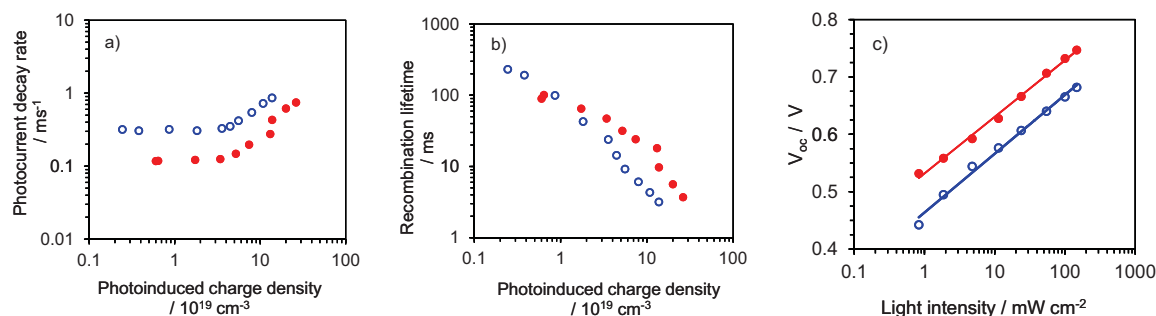
Figure 6.6: (a) Open-circuit transient photocurrent decay rate for DSC devices sensitized with complexes **R4** (red) and **R5** (blue) as a function of photoinduced charge density. (b) Charge recombination lifetime vs photoinduced charge density of the two devices measured at open-circuit conditions. (c) Open-circuit voltage vs the light intensity of the two devices, with illumination from a white LED light source.

rate vs charge density measured under open-circuit conditions. At identical charge density, the photoinduced electrons in the case of the **R4**-based device diffuse faster through the TiO$_2$ film than those of the dye **R5**-based device, resulting from a larger number of occupied trap states for the given Fermi level in the TiO$_2$ film. Figure 6.6b shows the dependence of the charge recombination lifetime on the photoinduced charge density. The recombination lifetime is determined by the reciprocal of the photovoltage decay rate obtained from a small perturbation voltage decay technique. The value of the charge density is obtained from the experimental measurements by collecting electrons when switching the device from open-circuit to short-circuit conditions. [23]

It is noted that the **R4**-sensitized device shows a longer charge recombination lifetime than that of the **R5**-sensitized device at an identical photoinduced charge density, clearly suggesting an advantage of **R4** in retarding charge recombination. However, this influence becomes smaller under incident low light intensity where fewer charges are accumulated in the TiO$_2$ film. The V_{oc} as a function of incident light intensity is displayed in figure 6.6c. The V_{oc} of both devices changes linearly according to the logarithm of the light intensity with the slope of 99 mV per decade and 102 mV per decade for devices sensitized with **R4** and **R5**, respectively. The almost identical slopes indicate that the trap states on the surface of TiO$_2$ are identical when both dyes are sensitized on TiO$_2$. The slope of 59 mV per decade is reported for an ideal diode. [24] The difference in the slope between the ideal diode and the real devices is attributed to a non-linear recombination occurring in the DSCs. [25]

6.4   Long-term stability

In addition to the volatile electrolyte, we also applied a solvent-free ionic liquid electrolyte (Z952, see composition in Appendix B) to verify the durability of DSC devices sensitized with **R1**, **R2** and **R3** under visible light soaking at 60 °C. The photovoltaic parameters for all three devices are summarized in table 6.2. Using **R1** we obtained a J_{sc} of 13.4 mA cm^{-2}, a V_{oc} of 0.69 V and a FF of 0.76, yielding an overall power conversion efficiency of 7.1% under illumination with standard AM 1.5 G simulated sunlight (100 mW cm^{-2}). The performances of sensitizers **R2** and **R3** were in the same range showing slightly lower η's of 6.6 and 6.7%, respectively.
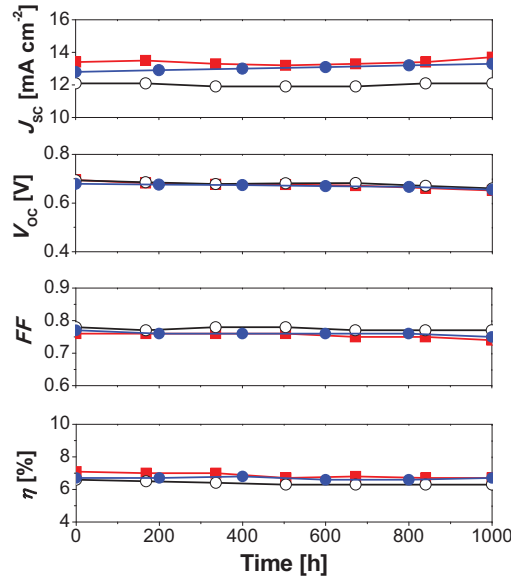
Figure 6.7: Evaluation of the photovoltaic parameters (J_{sc}, V_{oc}, FF and η) for the devices sensitized with **R1** (red), **R2** (black) and **R3** (blue), in combination with Z952 electrolyte during the visible light soaking (1 sun: 100 mW cm^{-2}) at 60 ∘C.

Figure 6.7 presents the variation in the photovoltaic parameters of dye-sensitized cells when subjected to the accelerating test in a solar simulator at full sunlight (100 mW cm^{-2}) and 60 °C. Over the entire 1000 h light soaking the photovoltaic parameters of the cells varied only slightly from the initial values. The V_{oc} of all devices was decreased by about 40 mV, which was partially compensated by a slight increase in the J_{sc} values. After the 1000 h light soaking and thermal stress, the η values retained ~95% of the initial values ($\eta = 6.7\%$ for **R1**; 6.3% for **R2**; and 6.7% for **R3**; respectively). Interestingly, the η of sensitizer **R3** maintained its initial value.

In order to understand the variations in the photovoltaic parameters, transient photo-

voltage decay measurements were recorded on devices before and after the light soaking process. The open-circuit voltage of devices sensitized with dyes **R1**–**R3** as a function of incident light intensity was plotted in figure 6.8a. Under the same light intensity, the aged cell showed lower V_{oc} values compared to the fresh cell. The chemical capacitance (C_μ) of both, the fresh and aged device, increased exponentially with increased bias potential as shown in figure 6.8b. The C_μ of aged devices was shifted for about 35–40 mV against the fresh device. This result indicates that after light soaking the conduction band edge of the TiO$_2$ was shifted to more positive potentials (vs NHE), resulting in a slight decrease of the V_{oc}. As shown in figure 6.8c, when we plotted the recombination lifetime against the photo induced charge density, we observed that at the same charge density the recombination life time for the aged and fresh devices were nearly the same. This reveals that the change in V_{oc} can only originate from the shift in the conduction band of the TiO$_2$ film. This effect is commonly observed in DSCs and could be attributed to the proton adsorption on the surface of the titania.

6.5 Conclusion

We have shown in this chapter five ruthenium complexes synthesized by click-chemistry as a tool for periphery functionalization of the ancillary ligand with three different triazole derivatives; **R1**, **R2** and **R3**, and for the design of new triazolyl chelating ligand; **R4** and **R5** and successfully used them as DSC sensitizers. **R1**–**R3** showed broad absorption bands covering from 300 to 700 nm region and their molecular absorption coefficient reached as high as 15400 M^{-1} cm^{-1} for the low energy MLCT transition. DSCs sensitized with these dyes provided the photo conversion efficiency close to 10% with a volatile acetonitrile-based electrolyte. Further studies with solvent-free ionic liquid based electrolyte show excellent device stability under prolonged full sunlight intensity at 60 °C. Transient photovoltage decay experiments reaffirmed that the decrease in the V_{oc} of aged devices compared to that of the fresh ones is due to the downward shift in the conduction band edge of TiO$_2$. DSC devices sensitized with **R4** and **R5** exhibited the photo conversion efficiency up to 7.8% which is a remarkable value considering that in comparison with to other bipyridine-based Ru(II) sensitizers, the absorption spectra are considerably blue-shifted and the molar absorption coefficients are significantly lower. Transient photovoltage decay analysis revealed that a better photovoltaic performance of **R4**-based device is due to the faster electron transport into the TiO$_2$ film and a lower recombination rate in comparison to the **R5**-based device. The large difference in device performance
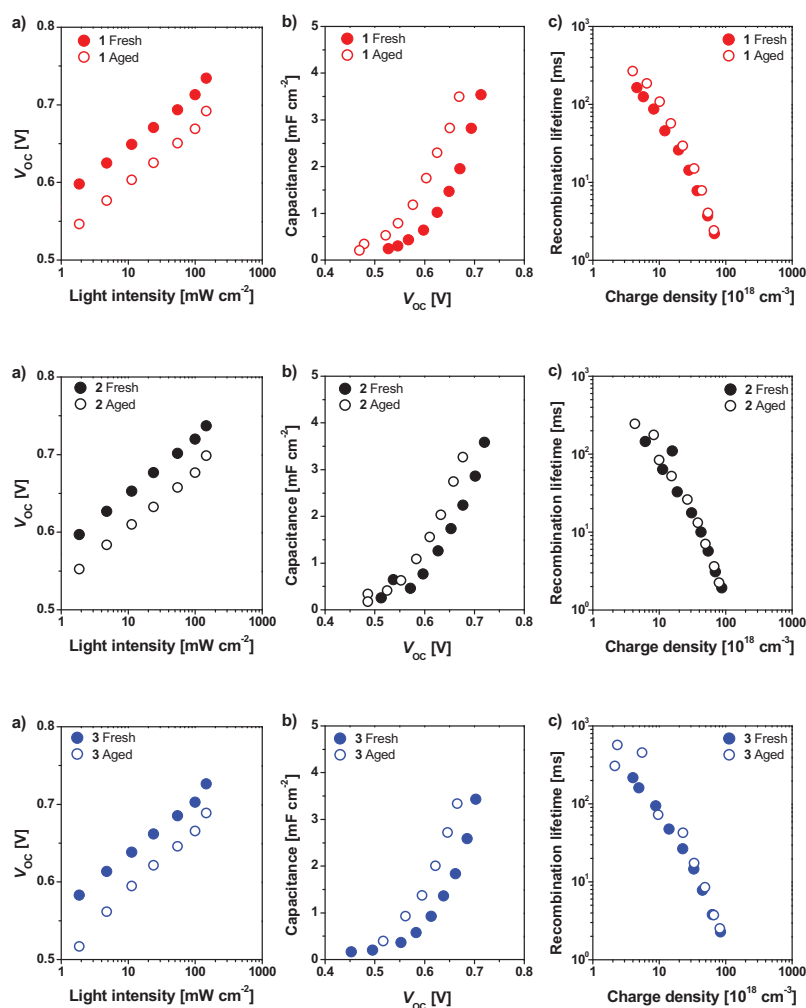
Figure 6.8: Transient photoelectrical plots of the fresh and aged devices sensitized with
R1 (top), **R2** (middle), and **R3** (bottom) in conjunction with ionic liquid electrolyte Z952.
a) Open-circuit voltage for devices as a function of incident light intensity. b) Chemical
capacitance of devices as a function of V_{oc}. c) Recombination lifetime of devices as a function
of photo-induced charge density.

correlates with minor structural changes in the isomeric ligands (see molecular structures
on page 99), which is the different substitution pattern of the 1,2,3-triazole unit. Taking
into account that it is possible to red-shift and to increase the absorption of these dyes by,
e.g. extending the π-conjugation, a new class of highly efficient 1,2,3-triazolyl-pyridine
Ru(II) sensitizers should be accessible via the convenient and versatile click-approach.

Bibliography

[1] A. Mishra, N. Pootrakulchote, M. K. R. Fischer, et al. Design and synthesis of a novel anchoring ligand for highly efficient thin film dye-sensitized solar cells. *Chemical Communications*, pages 7146–7148, 2009.

[2] A. Mishra, N. Pootrakulchote, M. Wang, et al. A thiophene-based anchoring ligand and its heteroleptic Ru(II)-complex for efficient thin-film dye-sensitized solar cells. *Advanced Functional Materials*, 21:963–970, 2011.

[3] Md. K. Nazeeruddin, P. Péchy, and M. Grätzel. Efficient panchromatic sensitization of nanocrystalline TiO₂ films by a black dye based on a trithiocyanato-ruthenium complex. *Chemical Communications*, page 1705, 1997.

[4] M. K. Nazeeruddin, F. D. Angelis, S. Fantacci, et al. Combined experimental and DFT-TDDFT computational study of photoelectrochemical cell ruthenium sensitizers. *Journal of the American Chemical Society*, 127:16835–16847, 2005.

[5] D. Shi, N. Pootrakulchote, R. Li, et al. New efficiency records for stable dye-sensitized solar cells with low-volatility and ionic liquid electrolytes. *Journal of Physical Chemistry C*, 112:17046–17050, 2008.

[6] C. Y. Chen, M. Wang, J. Y. Li, N. Pootrakulchote, et al. Highly efficient light-harvesting ruthenium sensitizer for thin-film dye-sensitized solar cells. *ACS Nano*, 3:3103–3109, 2009.

[7] P. Wang, C. Klein, R. Humphry-Baker, et al. Stable 8% efficient nanocrystalline dye-sensitized solar cell based on an electrolyte of low volatility. *Applied Physics Letters*, 86:123508, 2005.

[8] Polo A. S., M. K. Itokazu, and N. Y. M. Iha. Metal complex sensitizers in dye-sensitized solar cells. *Coordination Chemistry Reviews*, 248:1343–1361, 2004.

[9] C. Kaes, A. Katz, and M. W. Hosseini. Bipyridine: The most widely used ligand. A review of molecules comprising at least two 2,2′-bipyridine units. *Chemical Society Reviews*, 100:3553–3590, 2000.

[10] H. Hofmeier and U. S. Schubert. Recent development in the supramolecular chemistry of terpyridine-metal complexes. *Chemical Reviews*, 33:373–399, 2004.

[11] D. Kuang, C. Klein, H. J. Snaith, et al. Ion coordinating sensitizer for high efficiency mesoscopic dye-sensitized solar cells: Influence of lithium ions on the photovoltaic performance of liquid and solid-state cells. *Nano Letters*, 6:769, 2006.

[12] K. S. Chen, W. H. Liu, Y. H. Wang, et al. New family of ruthenium-dye-sensitized nanocrystalline TiO_2 solar cells with a high solar-energy-conversion efficiency. *Advanced Functional Materials*, 17:2964–2974, 2007.

[13] K. L. Wu, H. C. Hsu, K. Chen, et al. Development of thiocyanate-free, charge-neutral ru(II) sensitizers for dye-sensitized solar cells. *Chemical Communications*, 46:5124–5126, 2010.

[14] S. Paek, C. Baik, M. S. Kang, et al. New type of ruthenium sensitizers with a triazole moiety as a bridging group. *Journal of Organometallic Chemistry*, 695:821–826, 2010.

[15] C. M. Fitchett, F. R. Keene, C. Richardson, and P. J. Steel. Synthesis, x-ray crystal structures, spectroscopy and electrochemistry of ruthenium(II) complexes of two chelating ligands containing [1,2,3]triazolo[1,5-*a*]pyridine subunits. *Inorganic Chemistry Communication*, 11:595–598, 2008.

[16] C. Richardson, C. M. Fitchett, F. R. Keene, and P. J Steel. 4,5-di(2-pyridyl)-1,2,3-triazolate: the elusive member of a family of bridging ligands that facilitate strong metal-metal interactions. *Dalton Transactions*, pages 2534–2537, 2008.

[17] B. Happ, C. Friebe, A. Winter, et al. 2-(1H-1,2,3-triazol-4-yl)-pyridine ligands as alternatives to 2,2′-bipyridines in ruthenium(II) complexes. *Chemistry – An Asian Journal*, 4:154–163, 2009.

[18] B. Happ, D. Escudero, M. D. Hager, et al. N-heterocyclic donor- and acceptor-type ligands based on 2-(1H-[1,2,3]triazol-4-yl)pyridines and their ruthenium(II) complexes. *Journal of Organic Chemistry*, 75:4025–4038, 2010.

[19] Y. J. Li, J. C. Huffman, and A. H. Flood. Can terdentate 2,6-bis(1,2,3-triazol-4-yl)pyridines form stable coordination compounds? *Chemical Communications*, pages 2692–2694, 2007.

[20] I. Stengel, A. Mishra, N. Pootrakulchote, et al. Click-chemistry approach in the design of 1,2,3-triazolyl-pyridine ligands and their ru(II)-complexes for dye-sensitized solar cells. *Journal of Materials Chemistry*, 21:3726, 2011.

[21] D. J. V. C. van Steenis, O. R. P. David, G. P. F. van Striijdonck, et al. Click-chemistry as an efficient synthetic tool for the preparation of novel conjugated polymers. *Chemical Communications*, pages 4333–4335, 2005.

[22] P. Wang, B. Wenger, R. Humphry-Baker, et al. Charge separation and efficient light energy conversion in sensitized mesoscopic solar cells based on binary ionic liquids. *Journal of the American Chemical Society*, 127:6850–6856, 2005.

[23] B. C. O'Regan, K. Walley, M. Juozapavicius, et al. Structure/function relationships in dyes for solar energy conversion: A two-atom change in dye structure and the mechanism for its effect on cell voltage. *Journal of the American Chemical Society*, 131:3541–3548, 2009.

[24] S. Y. Huang, G. Schlichthörl, A. J. Nozik, M. Grätzel, and A. J. Frank. Charge recombination in dye-sensitized nanocrystalline TiO_2 solar cells. *Journal Physical Chemistry B*, 101:2576–2582, 1997.

[25] B. C. O'Regan and J. R. Durrant. Kinetic and energetic paradigms for dye-sensitized solar cells: Moving from the ideal to the real. *Accounts of Chemical Research*, 42:1799–1808, 2009.

Chapter 7

Optical Characterization of Dye-sensitized Solar Cells

7.1   Introduction

From previous chapters, we know that a good light harvesting efficiency (LHE) of sensitizers is the first step to achieve efficient DSCs. According to the Lambert-Beer law, the cell's LHE is determined by (a) the dye absorption coefficient (ϵ), (b) the attached dye concentration, and (c) the optical path length within the film. Improvement of the LHE is dependent upon whether the appropriate dye absorbance can be extended to a wider wavelength range, especially for wavelengths >700 nm. Intensive studies have been conducted to investigate sensitizers with wide light absorption bands, some of which have already been mentioned in previous chapters. However, when the same sensitizer is applied, the LHE can still be further enhanced by increasing the attached dye concentration or the optical path length by modification of nanocrystalline TiO_2 films, according to Lamber-Beer law. The attached dye concentration is dominated by the effective surface area that can be enlarged by reducing the size of the nanoparticles (down to 10-20 nm in diameter). Further reducing is difficult because such a small size is not suitable for colloid synthesis and screenprinting film preparation. Increasing the film optical path length seems more practical, and can be achieved by the addition of relatively large particles into a small particle solution to induce light scattering within the TiO_2 film, and J_{sc} improvement was indeed observed. [1, 2]

The light-scattering property of TiO$_2$ films induced by introducing relatively large particles into small particles has been simulated theoretically, using a multiflux model [3] or radiative transport theory. [4] Ferber and Luther calculated the optimum size and ratio of large particles mixed with small particles (20 nm in diameter) [4] and predicted the maximum LHE of the dye-sensitized TiO$_2$ film. They also concluded that the excess of the large particles enhances front surface light reflection, resulting in a LHE decrease. Rothenberger et al. employed a four-flux model to explain the light scattering properties and concluded that an appropriate mixture of small and large particles synthesized from acidic and basic TiO$_2$ solution, respectively, exhibits the maximum LHE over wavelengths considered for light absorption. [3]

This four-flux optical model has been used to describe the light absorption and scattering process in porous medium by separating the total light flux into two collimated fluxes and two diffuse fluxes. The measurements of the reflection and transmission spectra of the light passing through the porous film allows the determination of the absorption $k(\lambda)$ and scattering $s(\lambda)$ coefficients, the equivalent path length cofficient ϵ, and the forward scattering ratio coefficient ζ (see section 7.2). Reflectance and transmittance spectra were recorded by a spectrophotometer equipped with an integrating sphere. The wavelength-dependent absorption coefficient $k(\lambda)$ and scattering coefficient $s(\lambda)$ were determined from experimental data for different films. Once $k(\lambda)$, $s(\lambda)$, ϵ and ζ are determined, these parameters can be used to estimate the absorption in the same medium in more complex layer structures such as films with a back reflector or structures composed of two layers with different absorption and scattering properties. The total absorbed flux over the whole film thickness G(λ) can also be calculated from these four parameters. This study helps to understand the effect of different particle sizes on absorption and scattering in dye-sensitized porous nanocrystalline TiO$_2$ film and to further improve the optical design for dye-sensitized solar cells.

In this study, nanoporous TiO$_2$ films composed of 20 nm and 40 nm particle size, together with ZrO$_2$ film having 12 nm particle size were used. The films were sensitized with three different heteroleptic amphiphilic ruthenium complex sensitizers: (1) extended π-conjugation with thiophene derivatives unit (**B11**), (2) functionalized with carbazole antennas (**B12**) and (3) standard **Z907** will be used. The simulation of light propagating in the sensitized films will be studied to see an effect of different sensitizers, as well as film type and particle size on the absorption and scattering of the light by applying the four-flux model.

7.2 Optical model

In DSC, the light absorbed by dye sensitizer promotes it to an excited state, which injects an electron into the TiO_2 conduction band. To increase the light absorptivity of DSC, the optical property of nanocrystalline TiO_2 layer can be optimized by introducing a light-scattering layer. However, the optical property of this inhomogeneous TiO_2 film is generally a very complex phenomenon because of the re-scatttering and the intereaction of scattered light. [5] This complexity has been approached by the radiative transfer equation [6, 7]. One of the most successful was the simplest two-flux model; Kubelka-Munk (K-M) model [8] which predicts the optical property of scattering films under diffusive illumination from effective absorption and scattering coefficient of the material. This two-flux model describes the light propagation in two opposing directions presented by two diffusive fluxes through the medium by assuming that the layers are homogeneous and the light is completely diffusive inside the layer. This model has been widely used to investigate the optical property of light-scattering and light-absorbing medium in a matrix such as paints [9], papers [10], pigment polymers [11, 12] and so on. However, the use of K-M model in collimated incident light is not perfect and in some cases the dependence of scattering and absorption on film depth is significant. [6] Some revised or extended K-M models are developed to make it more applicable. [13–15] A more rigorous model with four-flux approach was proposed to implement the K-M model and is adopted here to study the optical process of DSC system. [16, 17]

Four-flux model

The simplified sample stack is shown in Figure 7.1. This sample is supposed to be isotropic and homogeneous on the μm scale so that it absorbs and scatters light but it is not luminescent. It is illuminated from the left with a collimated unpolarized monochromatic beam of intensity I_0, perpendicular to the substrate. This collimated beam undergoes multiple reflections at the air/glass and glass porous medium interfaces. The reflected part contributes to the collimated reflectance R_c. The transmitted fraction, neither absorbed nor scattered inside the porous medium, leaves the sample as the collimated transmittance T_c. The light diffusion inside the porous medium is partly transmitted which contributes to the diffuse transmittance T_d, and partly reflected which contributes to the diffuse reflectance R_d. The wavelenght-dependent values of T_c, T_d, R_c and R_d are obtained experimentally by changing the position of sample device as depicted in section 7.3.2.
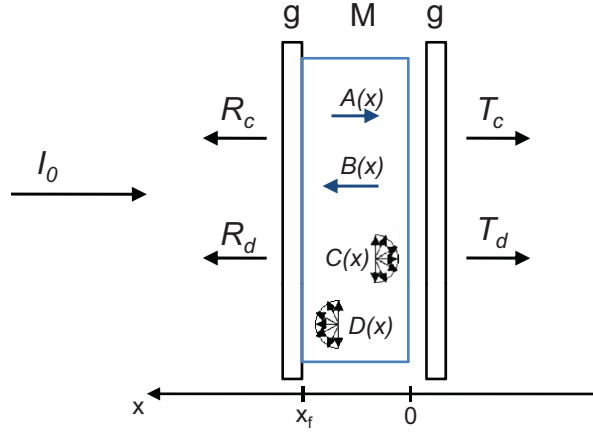
Figure 7.1: A simplified sample scheme consisting of g: glass substrate and M: porous medium having thickness x_f.

The four-flux model separates the total incident light beam into 4 distinct fluxes. Two collinear fluxes; one traveling in the forward direction and the other in the backward direction, are labeled in Figure 7.1 as $A(x)$ and $B(x)$, respectively. In addition, there are two diffuse fluxes; one traveling in the forward direction and the other in the backward direction, shown in Figure 7.1 as $C(x)$ and $D(x)$, respectively. The solid angles corresponding to the collimated fluxes are small enough, so that scattering into them can be neglected. By undertaking the energy balance for forward scattering, backward scattering and absorption within an infinitesimal volume of thickness dx, the four fluxes $A(x)$, $B(x)$, $C(x)$ and $D(x)$ can be formulated as following:

$$
\begin{aligned}
\frac{dA(x)}{dx} &= (k+s)A(x), \\[2mm]
\frac{dB(x)}{dx} &= -(k+s)B(x), \\[2mm]
\frac{dC(x)}{dx} &= \epsilon k C(x) + \epsilon(1-\zeta)sC(x) - \epsilon(1-\zeta)sD(x) - \zeta sA(x) - (1-\zeta)sB(x), \\[2mm]
\frac{dD(x)}{dx} &= -\epsilon k D(x) - \epsilon(1-\zeta)sD(x) + \epsilon(1-\zeta)sC(x) + (1-\zeta)sA(x) + \zeta sB(x), \quad (7.1)
\end{aligned}
$$

where $k(\lambda)$ and $s(\lambda)$ are the wavelength-dependent absorption coefficient and scattering coefficient in units of length^{-1}, respectively. The factor ϵ is the equivalent path length for the diffuse fluxes, which accounts for an increase of the optical path length in a slab dx when light is diffused rather than collimated; ϵ ranges from 1 for collimated light to 2 for isotropically scattered light. The factor ζ is the forward scattering ratio coefficient;

which ranges from 1, if light is scattered in the forward direction only, to 0, if light is back scattered only. the parameter x is the distance from the substrate; $x = 0$ corresponds to the location of light exit and $x = f$ the light entrance. The differential quations 7.1 can be solved subject to the boundary conditions at $x = 0$ and $x = x_f$ to obtain function solutions for A, B, C and D, from which the empirical coefficients ($k(\lambda)$ and $s(\lambda)$) can be calculated by using a non-linear least-squares algorithm. [3]

The local rate of light absorption per unit volume, $g(x)$ is defined as

$$g(x) = kA(x) + kB(x) + \epsilon kC(x) + \epsilon kD(x), \tag{7.2}$$

and the total absorbed flux over the whole film thickness is obtained from the integral:

$$G(\lambda) = \int_0^{x_f} g(x)\,\mathrm{d}x. \tag{7.3}$$

7.3 Experiments

7.3.1 Sample preparation

In this experiment, sensitizer **B11**, **B12** and standard **Z907** were optically characterized using TiO_2 and ZrO_2 as porous medium. The nanoporous photoanodes were prepared as described in section 2.1.3. The glass slide having thickness 1 mm was used for substrate instead of conducting glass (NSG 10) in order to reduce the number of interfaces to a minimum. The film area 2×2 cm^2 was required in order to match the light entrance port of the spectrophotometer. The type of the film, its thickness, particle size, and corresponding sensitizer were summarized in Table 7.1. The complete sample devices, as shown in Figure 7.1, were fabricated following the standard procedure described in section 2.2. The three sensitizers; **B11**, **B12** and **Z907** (see Appendix A) were prepared in a mixed solution of 90% of Acetronitrile and t-Butanol (1:1 volume ratio), plus 10% Dimethyl sulfoxide (DMSO) for better solubility. The electrolyte was replaced by a solvent of nearly identical refraction index. In this case, 3-methoxypropionitrile (MPN) was used.

Sample No.	Sensitizer	Film type	Particle size (nm)	Film thickness (μm)
1	**B11**			
2	**B12**	TiO$_2$	20	2.7
3	**Z907**			
4	**B11**			
5	**B12**	TiO$_2$	40	3.3
6	**Z907**			
7	**B11**			
8	**B12**	ZrO$_2$	12	2.7
9	**Z907**			

Table 7.1: Details of sample devices for optical characterization

7.3.2   Optical characterization

The transmittance and reflectance spectra were recorded with a Varian Cary 5 spectrophotometer equipped with an integrating sphere, the inner surface of which is coated with polytetralfluoroethylene (PTFE). The light entrance and exit port of the integrating sphere are aligned with the incident beam (entrance port: 19×17 mm²; exit port; circular with a diameter of 16 mm). To measure the total transmittance T_{tot}, a sample device was placed in front of the entrance port while the exit port was blocked with a plug having the inner surface coated with similar material as other part of the sphere. The total transmittance is a summation of collimated transmittance and diffuse transmittance ($T_{tot} = T_c + T_d$). The diffuse transmittance T_d was measured with the opened exit port. The diffuse reflectance R_d was measured when the sample device was placed behind the exit port normal to the incident beam. Finally, The total reflectance R_{tot}; a summation of collimated reflectance R_c and diffuse reflectance R_d ($R_{tot} = R_c + R_d$), was measured the same way as R_d with a small tilt in sample position. Figure 7.2 shows the configurations of integrating sphere for each measurement.
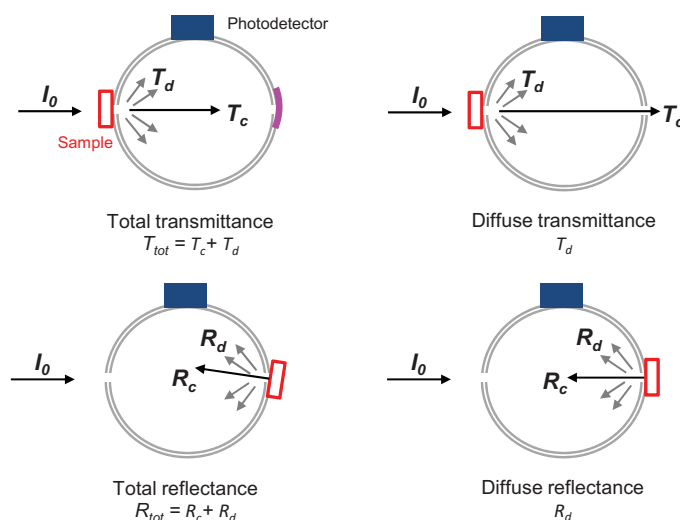
Figure 7.2: Schematic of integrating sphere configurations to measure the total/diffuse transmittance and reflectance of a given sample device.

7.4 Results and discussions

The measured four-flux transmittance and reflectance spectra of samples 1-3 are shown in figure 7.3. Figure 7.3d shows the four fluxes of the 20 nm TiO_2 film with no sensitizer absorbed, and the four spectra of the 20 nm TiO_2 absorbed with **B11**, **B12** and **Z907** are shown in figure 7.3a, 7.3b and 7.3c, respectively. Similarly, the transmittance and reflectance spectra of sample 4-6 and 7-9 are shown in figure 7.4 and 7.5, respectively. The four fluxes behave differently when the light interacts with films composed of different particle size. For reference, the four-flux spectra; T_c, T_d, R_c and R_d, of the 20 nm TiO_2 , 40 nm TiO_2 and 12 nm ZrO_2 films with no sensitizer absorbed are display in figure 7.3d, 7.4d and 7.5d, respectively.

The amplitudes of the four fluxes sum up to ~100% for 20 nm TiO_2 and 12 nm ZrO_2 films, whereas the *light loss* of approximately 10% is observed in case of 40 nm TiO_2 film. During the transmittance measurement, films composing of bigger particles render a stronger scattering effect to diffuse an incoming light compared to small particle films, allowing more light to escape from the side of sample devices and not being collected in the integrating sphere (see figure 7.2). Likewise, the reflected light can escape from the front window of the integrating sphere during the reflectance measurement and not being collected by the photodetector in case of the film with large particle size.

7.4.1 Effect of film type and particle size on light absorption and scattering

From figure 7.4d, one can observe a decrease of collimated part of the transmittance light (T_c) which corresponds to an increase of concomitant diffuse transmittance (T_d) as wavelength decreases. This arises from a strong scattering of the blank 40 nm TiO_2 film for shorter-wavelength light. However, the pattern is changed when sensitizers are absorbed on the TiO_2 film. The amplitudes of all four spectra are reduced below 550 nm where the sensitizers start to absorb the light as can be seen in figure 7.4a, 7.4b and 7.4c. Furthermore, the 40 nm TiO_2 films sensitized with **B11** and **B12** absorb more light in wavelength range 400–500 nm compared to **Z907**-sensitized film.

Figure 7.3: The measured (solid lines) and fitting (dotted lines) of transmission and reflection as a function of wavelength of the 2.7 μm-thick 20 nm TiO_2 film (a) with **B11** (sample 1), (b) with **B12** (sample 2), (c) with **Z907** (sample 3) and (d) without sensitizer.

In case of a visually-transparent film with 20 nm TiO_2 particle (figure 7.3d), the diffuse

parts of transmittance and reflectance light are much smaller compared to 40 nm TiO_2 film, resulting from a smaller scattering effect of small nanoparticles. Light of wavelength longer than 450 nm is likely to transmit through the film rather than being absorbed by it. When the sensitizers are absorbed on this film, a similar tendency is observed as in case of 60 nm TiO_2 film *i.e.* the films sensitized with **B11** and **B12** show higher amplitudes of light absorption than the **Z907**-sensitized film (see figure 7.3a, 7.3b and 7.3c).
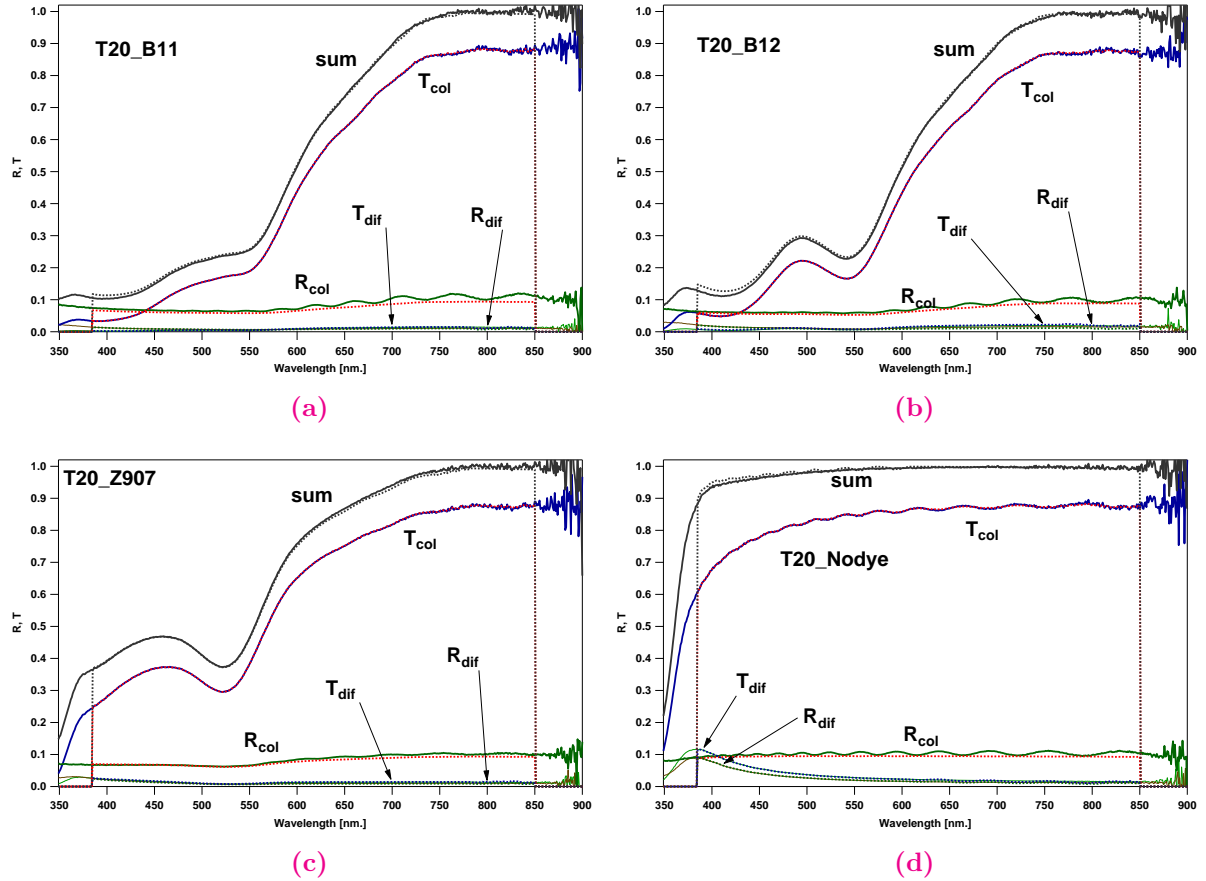

Figure 7.4: The measured (solid lines) and fitting (dotted lines) of transmission and reflection as a function of wavelength of the 3.3 μm-thick 40 nm TiO_2 film (a) with **B11** (sample 4), (b) with **B12** (sample 5), (c) with **Z907** (sample 6) and (d) without sensitizer.

For transparent thin film with small size of TiO_2 particles, the incoming light may reflect back collimatedly at the glass slide/TiO_2 interface or TiO_2/solvent interface and interfere with the reflectance part of the light during the reflectance measurement, forming a constructive and destructive patterns. This accounts for interference fringes observed in figure 7.3 either for blank or sensitized films which are inevitable in the experiment. The amplitude of the fringes depends on many factors such as the quality of the glass used, the properties of the porous layer, the composition of the solvent and the bandwitch

of the probe beam. The amplitude of the fringes become larger for longer wavelength. Nevertheless, the fringes render only a minor deviation in the modeling where the overall energy balance of scattered light is considered.
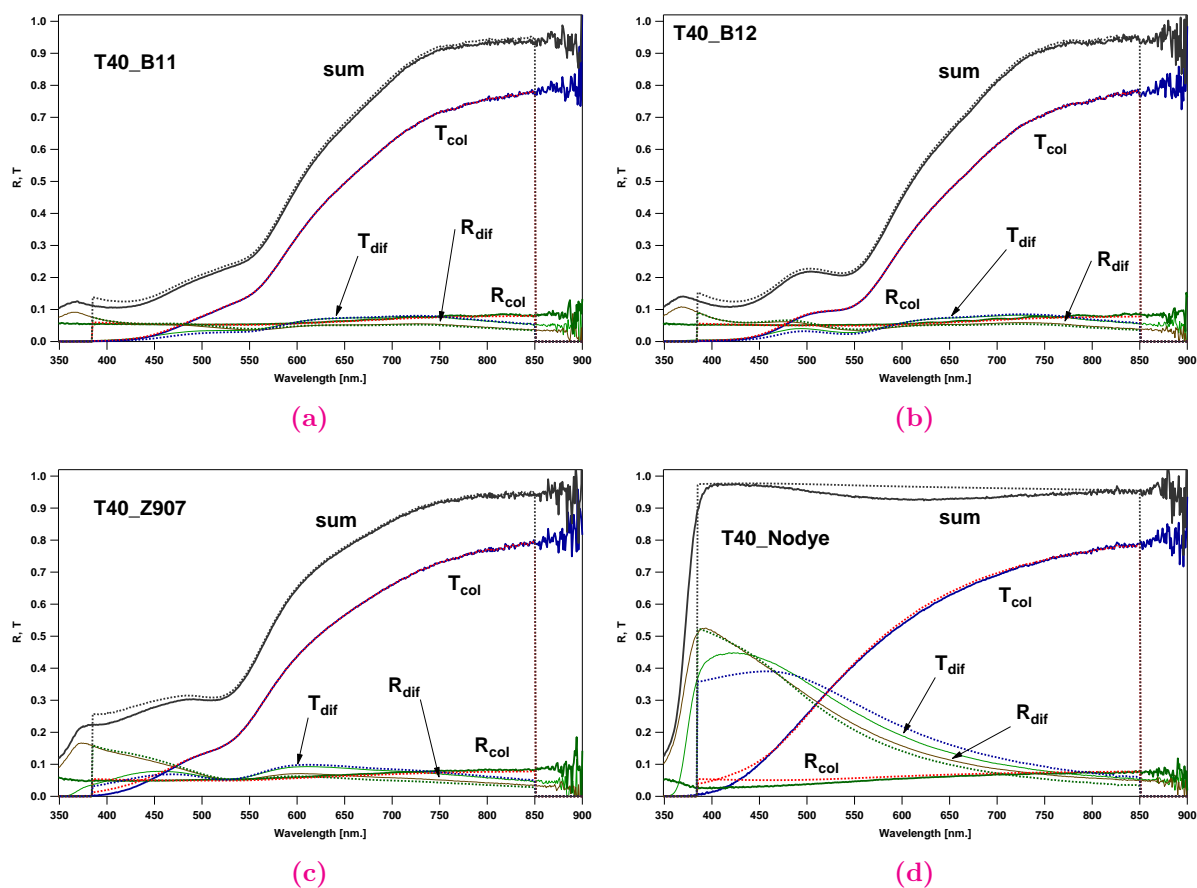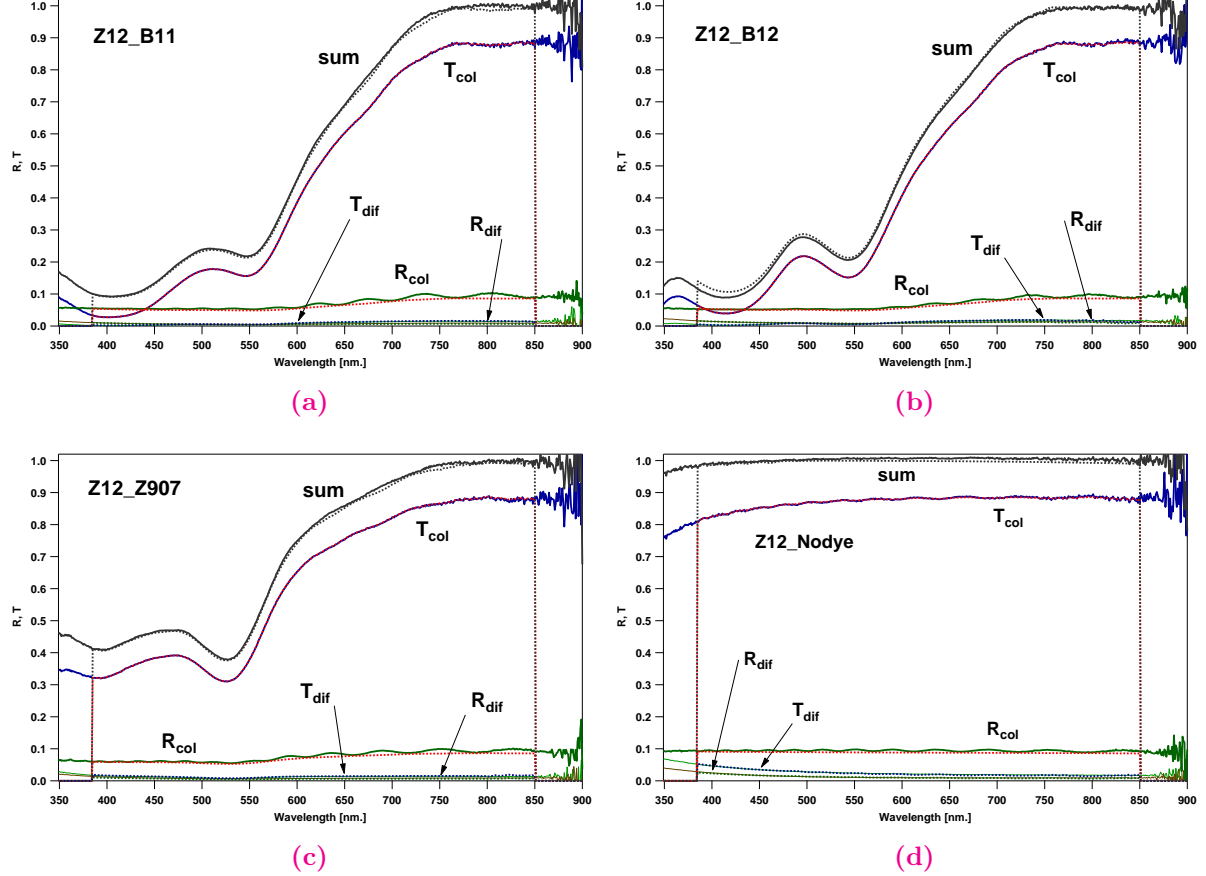

Figure 7.5: The measured (solid lines) and fitting (dotted lines) of transmission and reflection as a function of wavelength of the 2.7 μm-thick 12 nm ZrO$_2$ film (a) with **B11** (sample 10), (b) with **B12** (sample 11), (c) with **Z907** (sample 12) and (d) without sensitizer.

The dotted lines in all figures represent the simultaneous least-square fitting results from the four-flux model described in section 7.2. These modeling-fit results determine the optimal parameters $k(\lambda)$, $s(\lambda)$, ϵ and ζ for each sample. The wavelength-dependent absorption coefficient $k(\lambda)$ and scattering coefficient $s(\lambda)$ acquired from the four-flux model for **B11**, **B12** and **Z907** on nanocrystalline films of different type and particle size are displayed in figure 7.6. The equivalent path lengths and forwarding scattering ratios obtained from the fits are summarized in table 7.2.

From figure 7.6a, at wavelength range of 500-600 nm the absorption coefficient $k(\lambda)$ spectra of nanofilms sensitized with **B11** and **B12** show higher local maxima than those of
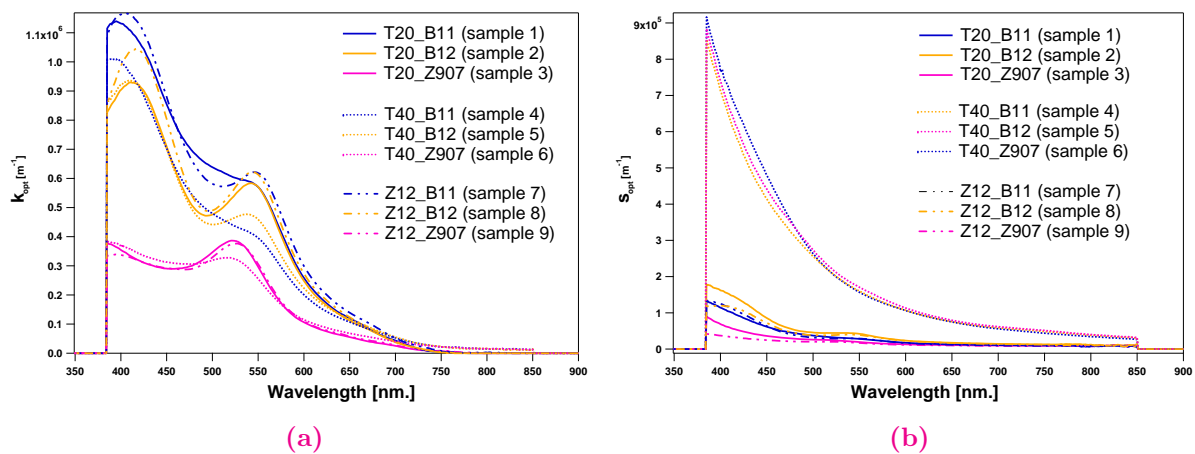
Figure 7.6: (a) The absorption $k(\lambda)$ and (b) the scattering $k(\lambda)$ coefficient values as a function of wavelength obtained with a least-squares fit of the four-flux model for all samples.

Sensitizer	Film type	ζ	ϵ
B11	20 nm TiO$_2$	0.60	1.99
	40 nm TiO$_2$	0.64	1.95
	12 nm ZrO$_2$	0.72	1.99
B12	20 nm TiO$_2$	0.64	1.99
	40 nm TiO$_2$	0.68	1.99
	12 nm ZrO$_2$	0.71	1.99
Z907	20 nm TiO$_2$	0.63	1.99
	40 nm TiO$_2$	0.67	1.99
	12 nm ZrO$_2$	0.72	1.99

Table 7.2: The equivalent pathlength (ϵ) and forward scattering ratio coefficient (ζ) values of each sample, obtained with the four-flux model.

Z907 for both 20 nm and 40 nm TiO$_2$ films as well as for ZrO$_2$ film, ascribed to the nearly double values of molecular absorption coefficients for **B11** and **B12** compared to that of **Z907** (see appendix A). The absorption peaks for **B11** and **B12** in this wavelength range show no significant difference for transparent 20 nm TiO$_2$ film and ZrO$_2$ films, but the peak for larger particle size TiO$_2$ film (40 nm) appears much lower. This reduction is ascribed to a lower dye concentration, as the specific surface area accessible for dye adsorption is smaller in the film with larger particle size. As one can expect, the scattering coefficient $s(\lambda)$ for the film containing larger particles (40 nm TiO$_2$) is higher by several order of

magnitudes than the those of transparent films (20 nm TiO_2 film and ZrO_2 film) as clearly depicted in figure 7.6b. The scattering efficiency increases with shorter wavelength.

The diffuse part of the light propagating in the film is characterized by the equivalent path length ϵ and the forward scattering ratio coefficient ζ, the definition of which is described in section 7.2. Considering the ϵ values in table 7.2, it is likely that scatterd light in the film is nearly isotropic for film composed of particle size in range of 20–40 nm, discarding type of film and sensitizer. Note that in other studies [18], it was reported that ϵ decreases as particle size increases, in agreement with the case of TiO_2 film sensitized by **B11** presented here.

The ζ values for all samples are found in range of 0.60–0.72. A higher ζ value for 40 nm TiO_2 film compared to that of 20 nm TiO_2 film for all three sensitizers implies that the scattered light is more oriented in the forward direction in case of larger particles. Surprisingly, the ZrO_2 film containing the smallest particle size gives the highest ζ values. The ζ value obtained by Mie calculations reported in the literature [4] is approx. 0.5 for very small TiO_2 particles. According to this reference the ζ values for ZrO_2 film obtained in this study are significantly too large. It is possible that the higher values in ZrO_2 case arise from dye aggregation.

7.4.2 Dye loading

For this approach, the absorption and scattering centers are well separated so that the absorption and scattering coefficients are proportional to the number of density of the centers: $k(\lambda) = \sigma_{abs}\, n_{abs}$ and $s(\lambda) = \sigma_{scatt}\, n_{scatt}$, where σ is the optical cross-sectional area and n is number density, for absorption and scattering, respectively. The σ_{abs} can be determined by essentially performing the "dye loading" experiment.

The sensitizer that is adsorbed on the film can be quantitatively desorbed with a suitable base after the optical measurement, and its amount can be determined. This dye loading experiment has been conducted by using a solution of tetra-butyl ammonium hydroxide (TBAOH) in dimethylformamide (DMF) with concentration of 0.1 g/ml as a desorbing agent. The sensitized films were immersed in this solution until the dye was completed desorbed, then an absorption spectrum was measured for the solution containing the dye in order to determine a volume fraction (n_{abs}) of the dye absorbed on the films by applying Beer-Lambert's law. Once the n_{abs} was known, the σ_{abs} can be calculated using $k(\lambda)$ values obtained from previous section, and $k(\lambda) = \sigma_{abs}\, n_{abs}$.

The results summarized in table 7.3 were determined in this way for **B11**, **B12** and **Z907** dyes adsorbed on 20 nm TiO_2 and 40 nm TiO_2 films.

Sensitizer	**B11**		**B12**		**Z907**	
TiO_2 film particle size (nm)	20	40	20	40	20	40
$n_{abs} \times 10^{-4}$ (mole cm^{-3})	1.24	0.50	1.48	0.49	1.58	0.88
$\sigma_{abs} \times 10^{-21}$ (m^2)	7.95	14.05	6.16	16.28	4.09	6.17

Table 7.3: The absorption cross-sectional area σ_{abs} of **B11**, **B12** and **Z907** sensitizers absorbed on transparent 20 nm TiO_2 film (2.7 μm-thick) and 40 nm TiO_2 film (3.3 μm-thick), obtained from the dye loading experiment. The molar extinction coefficient of three sensitizers are listed in appendix A and the absorption peaks were obtained from results in section 7.4.1.

The σ_{abs} values of 7.95×10^{-21} m^2 and 6.16×10^{-21} m^2 were obtained for **B11** and **B12** adsorbed on the 2.7 nm TiO_2 film, respectively, ascribed for a higher molecular extinction coefficient of **B11** than **B12**. **Z907** exhibits the smallest σ_{abs} on this film. As expected, the dye loadings on 40 nm TiO_2 film are much lower than those on 20 nm TiO_2 film for all three sensitizers (see n_{abs} values for comparison), suggesting the smaller accessible surface area in case of large particles. Note that a reference σ_{abs} value of 5.43×10^{-21} m^2 at 534 nm was previously reported for standard **N719** sensitizer in ethanol. [19] The dye loading for **B12** and **Z907** on 20 nm TiO_2 film appear equal in this experiment, in contrary to the results observed in section 5.3. In addition, the dye loading of **Z907** on 20 nm and 40 nm films shows much less different than those of the other two dyes. These errors are likely taken into account for a dye aggregation in case of **Z907**.

7.4.3   The total absorbed flux

The wavelength-dependent of the absorbed flux $G(\lambda)$ over the whole film thickness can be obtained from the integral in equation 7.3 described in previous section. By comparing the total absorbed flux of **B11**, **B12** and **Z907** sensitized on 20 nm TiO_2 film (figure 7.7a) calculated at film thickness (x_f) = 2.7 μm, it can be clearly seen that **B11** and **B12** provide a higher absorption efficiency compared to **Z907**, agreed with the $k(\lambda)$ results in section 7.4.1. The absorption peaks of **B11** and **B12** also show no significance difference on transparent films, suggesting that the different functionalized groups (hexylthiobithiophene unit for **B11** and carbazole unit for **B12**, see appendix A) does not effect much on an absorption efficiency of the dye sensitizers. The same behavior is observed on 40 nm

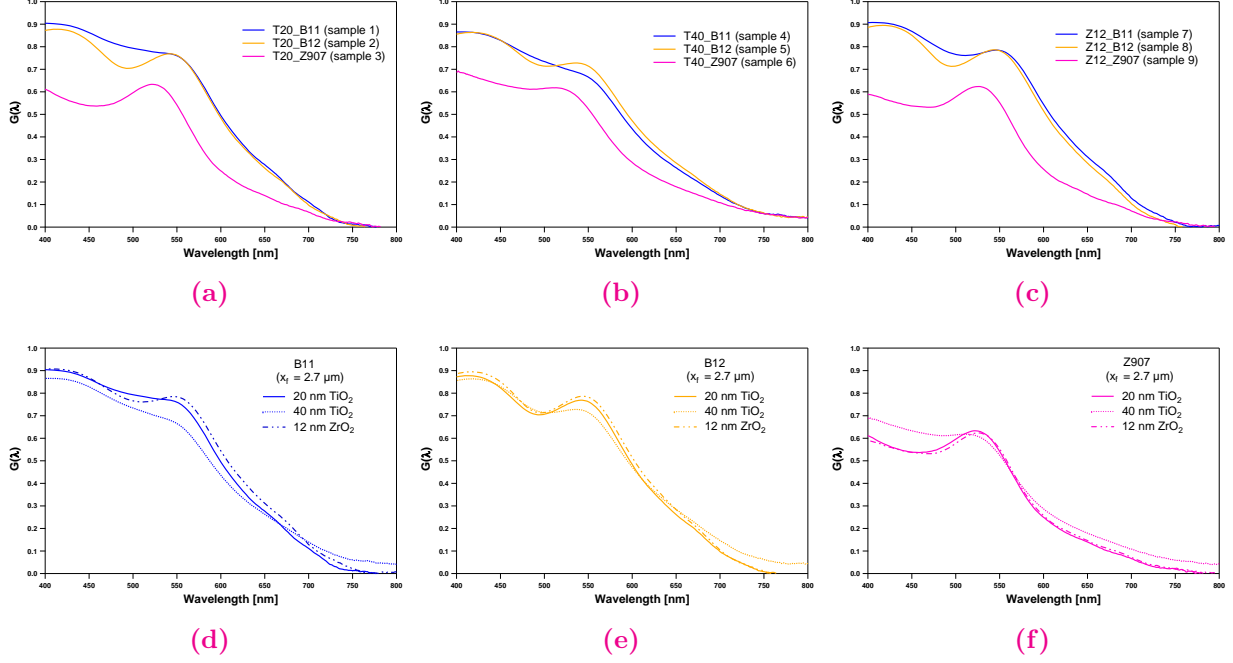TiO$_2$ film and 12 nm ZrO$_2$ film as displayed in figure 7.7b and 7.7c, respectively.

Figure 7.7: The total absorbed flux $G(\lambda)$ as a function of wavelength for samples 1-9, calculated for a film thickness of x$_f$ = 2.7 μm: (a)-(c) effect of dye sensitized on 20 nm TiO$_2$ film, 40 nm TiO$_2$ film and 12 nm ZrO$_2$ film, respectively; (d)-(f) effect of film type and film particle size sensitized with **B11**, **B12** and **Z907**, respectively.

On the other hand, one can compare the effect of the film type and particle size on the total absorbed flux, when the film is sensitized with different dyes. Figure 7.7d, 7.7e and 7.7f show the $G(\lambda)$ values of the three dyes adsorbed on different 20 nm TiO$_2$ film, 40 nm TiO$_2$ and 12 nm ZrO$_2$ film, respectively (the $G(\lambda)$ values are calculated at x$_f$ = 2.7 μm). It is observed that for long wavelength region, the film composed of large particles increases the fraction of the incoming light than is absorbed, by increasing the optical path length of the film. [20]. This phenomenon is observed more clearly in case of **Z907**, which has lower molecular absorption coefficient value than the other two sensitizers. It implies that large complex molecules such as **B11** and **B12** tend to absorb the light rather than scatter it when sensitized on the film with particle size ranges 20-40 nm.

7.4.4   The absorbed flux and IPCE

In general, the absorption efficiency ($G(\lambda)$) can be considered as an integral of local rate of light trapped in the film per unit volume; by both absorption and scattering, over

the whole film thickness at a given wavelength. By integrating the product of $G(\lambda)$ and the spectral photon flux density $\phi(\lambda)$ (units m^{-2} nm^{-1} s^{-1}) incident on the film yields the hypothetical maximal electric current density ($J_{sc,max}$). Thus, the $G(\lambda)$ spectrum is comparable to the incident photon to current conversion efficiency (IPCE) (see section 2.3.2). In order to compare $G(\lambda)$ with the IPCE spectrum, a transparent 2.7 μm-thick TiO$_2$ film composed of 20 nm TiO$_2$ particle size was prepared on conducting glass as described in section 2.1.3. The film was sensitized by 0.3 mM **B11** solution for 15 h and then was fabricated using volatile electrolyte Z960 as described in section 2.2 in order to measure the *J-V* characteristics and IPCE spectrum. The photovoltaic parameters appeared as $J_{sc} = 11.0$ mA cm^{-2}, $V_{oc} = 0.707$ V and *FF*= 0.71, yielding the conversion efficiency η of 5.6%. The characteristic *J-V* curve is plotted in figure 7.8a, and the corresponding normalized IPCE spectrum of the same device in comparison with $G(\lambda)$ spectrum obtained from previous section (see figure 7.7a and 7.7d) are plotted in figure 7.8b.
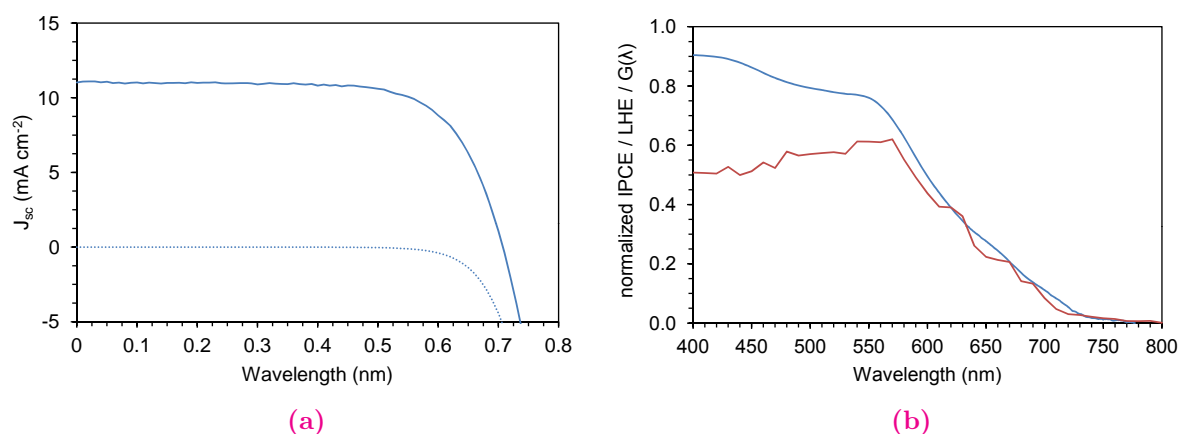

(a)   (b)

Figure 7.8: (a) *J-V* characteristic curves under full sunlight (AM 1.5 G, 100 mW cm^{-2}) (solid line) and in the dark (dotted line) of DSC test device based on a transparent 20 nm TiO$_2$ film of 2.7 μm thick, sensitized with **B11** sensitizer in corporate with Z960 acetonitrile-based electrolyte (illumination area = 0.59 cm^2). (b) The corresponding normalized IPCE spectrum (red) compared with the $G(\lambda)$ values (blue) calculated at x$_f$ = 2.7 μm, obtained from section 7.4.3.

IPCE spectrum in figure 7.8b agreed well with the calculated $G(\lambda)$ for wavelength longer than ~600 nm. However, a marked reduction of IPCE values at strongly absorbed light wavelengths below 600 nm can come from several factors. The $G(\lambda)$ calculation assumes a collinear incident light, and every absorbed photons yields an electron in the external circuit. The IPCE calculation is based on incident light which is diffuse and may not be absorbed by the sensitizer. The conducting glass used in photovoltaic experiment

also absorbs 15–20% of incident light in range of 400–800 nm, where the light absorption of glass slide used in optical measurement is negligible. The light absorption by triiodide species in the electrolyte is significant up to 650 nm, particularly strong below 520 nm. [21]. As mentioned in section 2.3.2, the IPCE can be factorized into light harvesting efficiency (LHE), the charge injection efficiency ϕ_{inj} and the charge collection efficiency η_{coll}. Giving a high LHE efficiency of **B11** sensitizer as seen from its absorption spectrum leaves a limitation in collection efficiency due to the electron transport obstructions in the electrolyte, electron density dependence of the electron diffusion length or slow photocurrent response time due to electron trapping. [22] Any of these loss processes may account for the difference between $G(\lambda)$ and IPCE spectra below 600 nm.

7.5   Conclusion

In this chapter the four-flux model was described with several factors to simulate how the light propagates in the nanocrystalline TiO_2 and ZrO_2 porous films sensitized with dye sensitizers **B11**, **B12** and **Z907** to understand the effect of film type, particle size, as well as functionalized groups of dye sensitizers on the light absorption and scattering in the film. The absorption coefficient $k(\lambda)$ spectra of the films sensitized with **B11** and **B12** show superior local maxima at 500–600 nm to that of **Z907**, in agreement with findings in chapter 3 and 5. The absorption peaks appear no significant difference for transparent film 20 nm TiO_2 and 12 nm ZrO_2 film, but much lower in case of semi-transparent TiO_2 film composed of larger particle size (40 nm), where light scattered more effectively below 550 nm. Sensitizer with high molecular extinction coefficient such as **B11** and **B12** adsorbed on transparent film tend to absorb light rather than scatter it. There is no indicative deviation from different functionalized groups of **B11** and **B12** sensitized on transparent TiO_2 and ZrO_2 film.

The total absorbed flux $G(\lambda)$ over the entire film thickness is comparable to the IPCE values at long wavelength. However, a lower IPCE efficiency than $G(\lambda)$ at shorter wavelength range is observed resulting from several loss processes.

There are several assumptions made and limitations in boundary conditions used for solving the set of equation 7.1 when the four-flux model was applied in this study that needed to be modified when the sun is used as a light source in stead of the collinear monochromatic spectrophotometer used in the experiment. However, the model has several features that render it particularly useful to researchers developing and testing the

optical parameters of materials for DSCs.

Bibliography

[1] C. J. Barbé, F. Arendse, P. Comte, et al. Nanocrystalline titanium oxide electrodes for photovoltaic applications. *Journal of the American Ceramic Society*, 80:3157–3171, 1997.

[2] M. K. Nazeeruddin, P. Péchy, T. Renouard, et al. Engineering of efficient panchromatic sensitizers for nanocrystalline TiO_2 -based solar cells. *Journal of the American Chemical Society*, 123:1613–1624, 2001.

[3] G. Rothenberger, P. Comte, and M. Grätzel. A contribution to the optical design of dye-sensitized nanocrystalline solar cells. *Solar Energy Materials and Solar Cells*, 58:321–336, 1999.

[4] J. Ferber and J Luther. Computer simulations of light scattering and absorption in dye-sensitized solar cells. *Solar Energy Materials and Solar Cells*, 54:265–275, 1998.

[5] A. Usami and H. Ozaki. Optical modeling of nanocrystalline TiO_2 films. *Journal of Physical Chemistry B*, 109:2591–2596, 2005.

[6] W. E. Vargas and G. A. Niklasson. Intensity of diffuse radiation in particulate media. *Journal of the Optical Society of America A*, 14(9):2253, 1997.

[7] William E. Vargas. Generalized four-flux radiative transfer model. *Applied Optics*, 37(13):2615, 1998.

[8] Paul Kubelka. New contributions to the optics of intensely light-scattering materials. part i. *Journal of the Optical Society of America*, 38(5):448, 1948.

[9] Arthur B. Krewinghaus. Infrared reflectance of paints. *Applied Optics*, 8(4):807, 1969.

[10] C. Rennel and M. Rigdahl. Enhancement of the light-scattering ability of coatings by using hollow pigments. *Colloid & Polymer Science*, 272(9):1111, 1994.

[11] W. E. Vargas and G. A. Niklasson. Reflectance of pigmented polymer coatings: comparisons between measurements and radiative transfer calculations. *Applied Optics*, 40(1):85, 2001.

[12] M. M. Beppu, E. C. Lima, and F. Galembeck. Aluminum phosphate particles containing closed pores: Preparation, characterization, and use as a white pigment. *Journal of Colloid and Interface Science*, 178:93–103, 1996.

[13] L. Yang and B. Kruse. Revised Kubelka-Munk theory. I. Theory and application. *Journal of the Optical Society of America A*, 21(10):1933, 2004.

[14] L. Yang and S. J. Miklavcic. Revised Kubelka Munk theory. II. Unified framework for homogeneous and inhomogeneous optical media. *Journal of the Optical Society of America A*, 21(10):1942, 2004.

[15] L. Yang, B. Kruse, and S. J. Miklavcic. Revised Kubelka-Munk theory. III. A general theory of light propagation in scattering and absorptive media. *Journal of the Optical Society of America A*, 22(9):1866, 2005.

[16] B. Maheu, J. N. Letoulouzan, and G. Gouesbet. Four-flux models to solve the scattering transfer equation in terms of lorenz-mie parameters. *Applied Optics*, 23(19):3353, 1984.

[17] B. Maheu and G. Gouesbet. Four-flux models to solve the scattering transfer equation: special cases. *Applied Optics*, 25(7):1122, 1986.

[18] W. E. Vargas and G. A. Niklasson. Forward average path-length parameter in four-flux radiative transfer models. *Applied Optics*, 36:3735, 1997.

[19] M. K. Nazeeruddin, A. Kay, I. Rodicio, et al. Conversion of light to electricity by cis-x2bis(2,2′-bipyridyl-4,4′-dicarboxylate)ruthenium(II) charge-transfer sensitizers on nanocrystalline titanium dioxide electrodes. *Journal of the American Chemical Society*, 115:6382–6390, 1993.

[20] Y. Tachibana, K. Hara, K. Sayama, and H. Arakawa. Quantitative analaysis of light-harvesting efficiency and electron-transfer yiel in ruthenium-dye-sensitized nanocrystalline TiO_2 solar cells. *Chemical Materials*, 14:2527–2535, 2002.

[21] J. Halme, P. Vahermaa, K. Miettunen, and P. Lund. Device physics of dye solar cells. *Advanced Materials*, 22:E210–E324, 2010.

[22] P. M. Sommeling, H. C. Rieffe, J. A. M. van Roosmalen, et al. Spectral response and iv-characterization of dye-sensitized nanocrystalline TiO_2 solar cells. *Solar Energy Materials and Solar Cells*, 62:399–410, 2000.

Chapter 8

Final Conclusion

The dye-sensitized solar cell (DSC) has been considered the "new" generation solar cell for the 21st century and is a fast growing multidisplinary subject. In a near future, this system will promote the acceptance of clean and renewable energy technology, not least by setting new standard of convenience and economy. As one of the crucial parts in DSC, it is challenging to search for optimum sensitizers which are capable of absorbing the whole region of visible light whereas having their excited state levels higher than the conduction band edge of the semiconductor and their oxidized stated levels more positive than the redox potential of electrolyte. Promising strategies to gain higher molecular absorptivity of sensitizers, ruthenium-based ones in this case, include an extension of a π-conjugation system in both ancillary/anchoring ligands, a functionalization of the sensitizer molecules with electron-rich antennas, and so on.

All works discussed in this thesis were going toward this goal. We have presented new benchmarks for high performance DSCs with ruthenium complex sensitizers with π-extension in their ancillary ligands. The overall conversion efficiency of 9.6% and 8.5% have been achieved with Ru-based sensitizer containing ethylenedioxythiophene, using low-volatile electrolyte and solvent-free electrolyte, respectively. Furthermore, the Ru-sensitizer functionalized with hexylthio-bithiophene unit also expressed a conversion efficiency of 9.4% with low-volatile electrolyte. All three devices showed good stability under prolonged light soaking at 60 °C. Extending π-conjugation of the anchoring ligand with thiophene units in monoleptic Ru-sensitizer also yields an impressive conversion efficiency of 6.1% using 3-μm-thin mesoporous TiO_2 film in corporate with low-volatile electrolyte.

Ruthenium sensitizers based on new antennas consisting of the sequential connection of an electron-rich thienothiophene- and EDOT-conjugated bridge, together with carbazole hole-transport moiety on their ancillary ligands were presented. The corresponding DCS devices with a volatile electrolyte exhibited 9.4% and 9.6% conversion efficiency for thienothiophene- and EDOT-conjugation, respectively. In addition, the devices based on these two bridges in association with low-volatility electrolyte also showed an excellent stability. On the other hand, the Ru-complexes synthesized by click-chemistry as a tool for periphery functionalization of the ancillary ligands with different triazole derivatives, and for the design of new triazolyl chelating ligands were successfully used as DCS sensitizers. DSC devices sensitized with these dyes provided the overall conversion efficiency close to 10% with volatile electrolyte. Further studies with solvent-free electrolyte showed notable device stability under extending full sunlight intensity at 60 °C. An optical characterization has been performed on **B11**, **B12** and **Z907** sensitizers featuring the four-flux model. **B11** and **B12** exhibited a higher absorption efficiency than **Z907** for both absorption and scattering parts of the light propagating in the film, however, there is no indicative deviation from different functionalized groups of **B11** and **B12** sensitized on transparent TiO_2 and ZrO_2 film. The absorption efficiency $G(\lambda)$ over the entire film thickness obtained from the simulation model is comparable to the IPCE values at long wavelength range.

Future outlook. To attain a DSC with higher efficiency, while maintaining its robustness, through an enhanced light-harvesting capability of the ruthenium-based sensitizer and better charge-collection yields of the sensitized mesoscopic semiconducting films, one needs to search for designated strategies to incorporate one 4,4′-dicarboxybipyridine ligand of the ruthenium complex with new potential electron-donor functionalities in order to further broaden the absorption spectra and to increase the molar extinction coefficient (ϵ). For long-term stability reasons, a cografting of the sensitizer with other coadsorbent molecules should also be intensively investigated to improve a blocking effect from photoelectron recombination via electrolyte. All these strategies would expand the DSC capability to better harvest the sun's energy and decrease human's dependency on fossil fuels and nuclear power.

Appendices

Appendix A

List of Ruthenium sensitizers

Code	Complex formula[a]	λ_{max} (nm)[b] (ϵ [M^{-1} cm^{-1}])	HOMO [eV]	LUMO [eV]	$\triangle E$ [eV]
N719	[Ru(dcbpy)$_2$(NCS)$_2$]$^{2-}$ [TBA]$_2$$^{2+}$	535 (13 500)	-5.38	-3.06	2.32
Z907	[Ru(dcbpy)(dnbpy)(NCS)$_2$]$^-$ Na$^+$	526 (12 200)	-5.28	-3.11	2.17
BTC-1	[Ru(dtcbpy)$_2$(NCS)$_2$]$^{2-}$ [TBA]$_2$$^{2+}$	563 (23 200)	-5.29	-3.34	1.95
BTC-2	[Ru(dtcbpy)(dnbpy)(NCS)$_2$]$^-$ Na$^+$	548 (16 000)	-5.22	-3.30	1.92
C103	[Ru(dcbpy)(dehtbpy)(NCS)$_2$]$^-$ Na$^+$	550 (18 800)	-5.40	-3.69	1.71
B11	[Ru(dcbpy)(dhtbtbpy)(NCS)$_2$]$^-$ [TBA]$^+$	554 (24 200)	-5.46	-3.88	1.59
B19	[Ru(dcvbpy)(dhtbtbpy)(NCS)$_2$]$^{2-}$	562 (29 700)	-5.47	-3.90	1.57
B12	[Ru(dcbpy)(dbttcbpy)(NCS)$_2$]$^-$ [TBA]$^+$	555 (22 400)	-5.48	-3.90	1.58
B13	[Ru(dcbpy)(dbetcbpy)(NCS)$_2$]$^-$ [TBA]$^+$	547 (19 300)	-5.44	-3.86	1.58
R1	[Ru(dcbpy)(dh[tz]bpy)(NCS)$_2$]$^-$ Na$^+$	536 (11 900)	-5.26	-3.25	2.01
R2	[Ru(dcbpy)(dh[ph][tz]bpy)(NCS)$_2$]$^-$ [TBA]$^+$	539 (13 900)	-5.36	-3.36	2.00
R3	[Ru(dcbpy)(d[tod][ph][tz]bpy)(NCS)$_2$]$^-$ [TBA]$^+$	540 (15 400)	-5.32	-3.34	1.98
R4	[Ru(dcbpy)(h[ph]tz-4-py)(NCS)$_2$]$^-$ [TBA]$^+$	493 (7 600)	-5.23	-3.11	2.12
R5	[Ru(dcbpy)(h[ph]tz-1-py)(NCS)$_2$]$^-$ [TBA]$^+$	465 (9 200)	-5.28	-3.09	2.19

[a]See Ligands abbreviations on the next page.
[b]measured in DMF

Ligand abbreviations

dcbpy	–	2,2′-bipyridine-4,4′-dicarboxylic acid
dtcbpy	–	5,5′-(2,2′-bipyridine-4,4′-diyl)-bis(thiophene-2-carboxylic acid)
dnbpy	–	4,4′-dinonyl-2,2′-bipyridine
dcvbpy	–	4,4′-dicarboxyvinyl-2,2′-bipyridine
dehtbpy	–	4,4′-di(3,4-ethylenedioxyl-2-hexylthiophenyl)-2,2′-bipyridine
dhtbtbpy	–	4,4′-bis(5-(hexylthio)-2,2′-bithien-5′-yl)-2,2′-bipyridine
dbttcbpy	–	4,4′-bis[3,6-bis-t-butyl-9-(2-thieno[3,2-b]thienyl)carbazole]-2,2′-bipyridine
dbetcbpy	–	4,4′-bis[3,6-bis-t-butyl-9-(3,4-(ethylenedioxy)thien-2-yl)carbazole]-2,2′-bipyridine
dh[tz]bpy	–	4,4′-bis(1-hexyl-1H-1,2,3-triazol-4-yl)-2,2′-bipyridine
dh[ph][tz]bpy	–	4,4′-bis(4-hexylphenyl-1H-1,2,3-triazol-4-yl)-2,2′-bipyridine
d[tod][ph][tz]bpy	–	4,4′-bis{1-[4-(1,4,7,10-tetraoxaundecanyl)phenyl]-1H-1,2,3-triazol-4-yl}-2,2′-bipyridine
h[ph]tz-4-py	–	2-[1-(4-hexylphenyl)-1H-1,2,3-triazol-4-yl]pyridine
h[ph]tz-1-py	–	2-[1-(4-hexylphenyl)-1H-1,2,3-triazol-1-yl]pyridine
NCS	–	thiocyanate
Na	–	Sodium
TBA	–	bis-tetrabutylammonium [N(C$_4$H$_9$)$_4$]

Chemical structures

(a) N719

(b) Z907
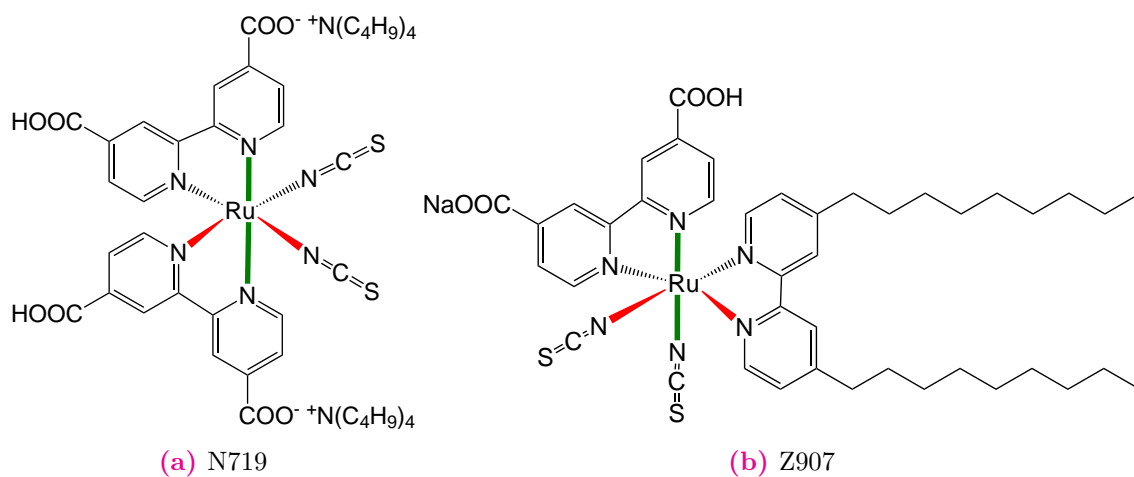
Figure A.1: Standard sensitizers

(a) BTC-1

(b) BTC-2
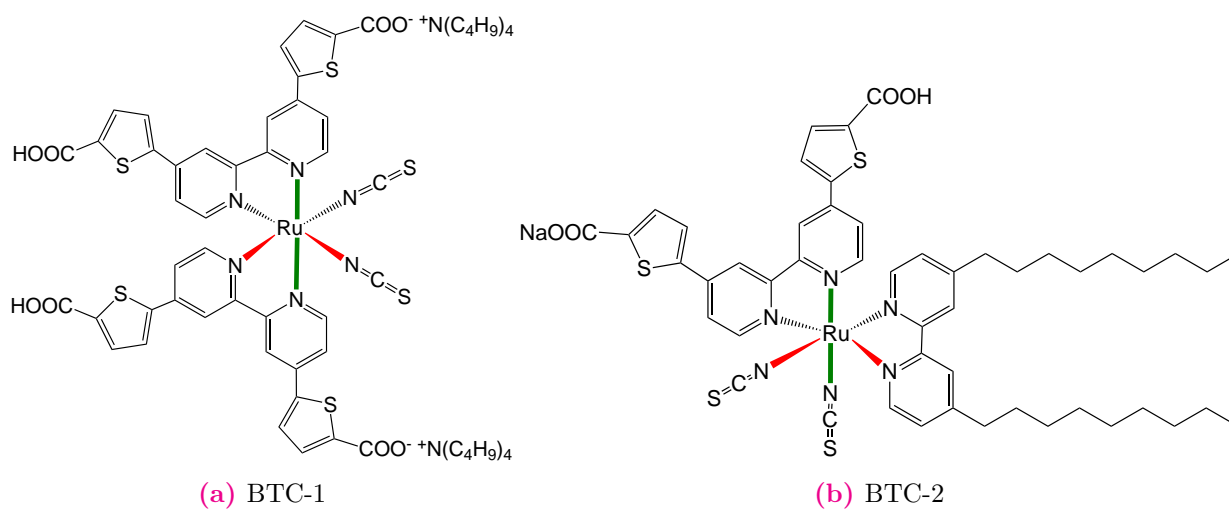
Figure A.2: Sensitizers with extended π-conjugations on ancillary ligands

(a) C103

(b) B11

(c) B19
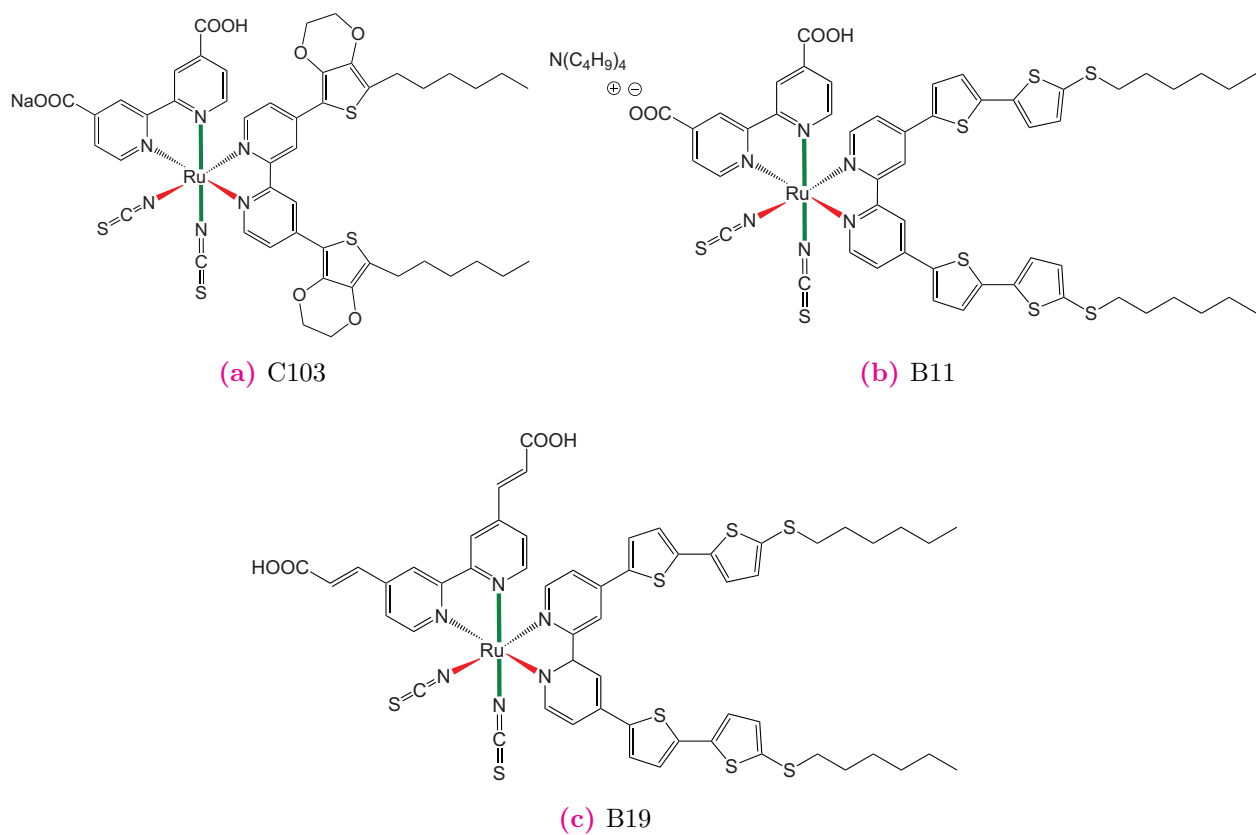
Figure A.3: Sensitizers with extended π-conjugations on anchoring ligands

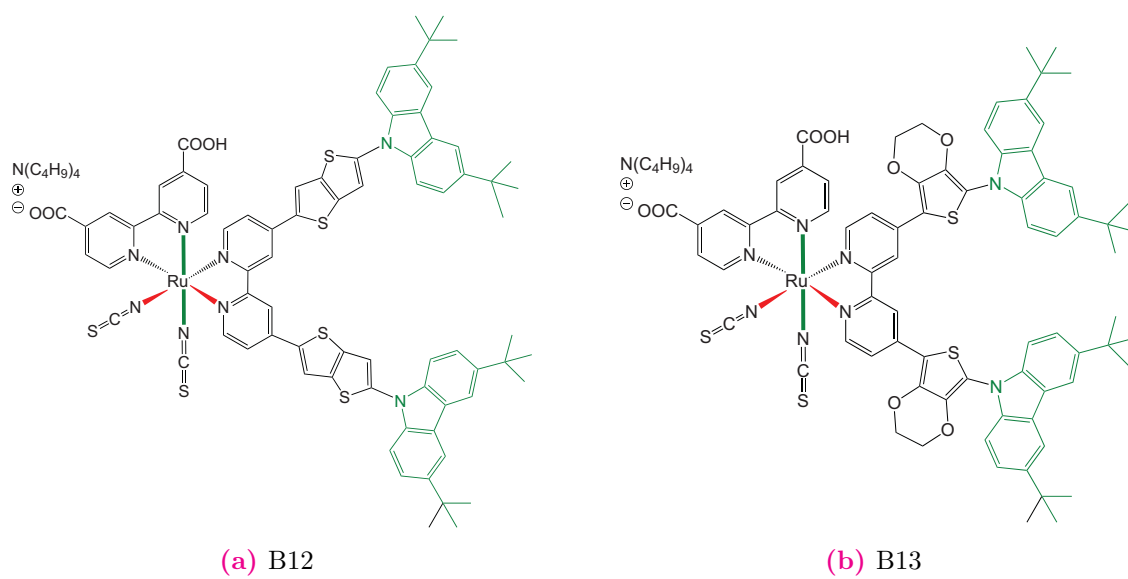

(a) B12

(b) B13

Figure A.4: Sensitizers functionalized with Carbarzole antennas
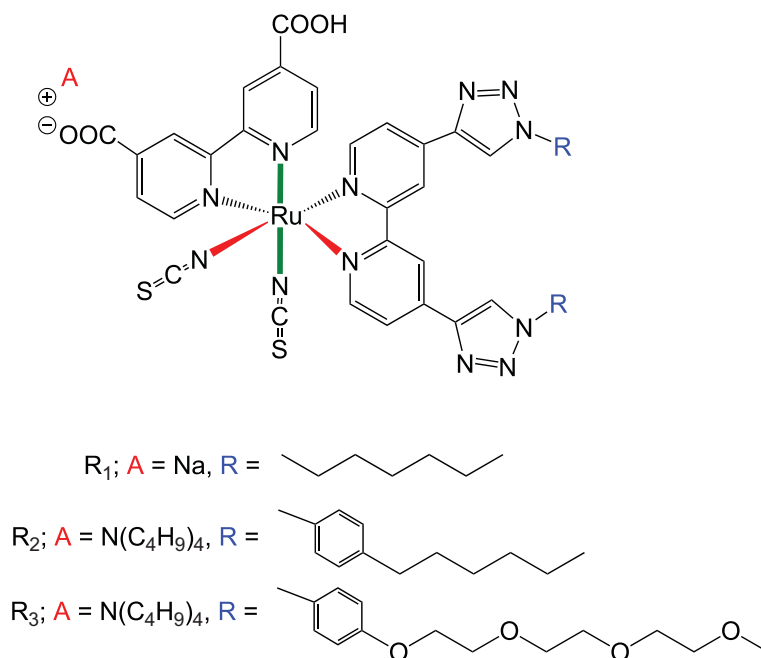
Figure A.5: Sensitizers functionalized with Triazole antennas on periphery of ancillary ligands
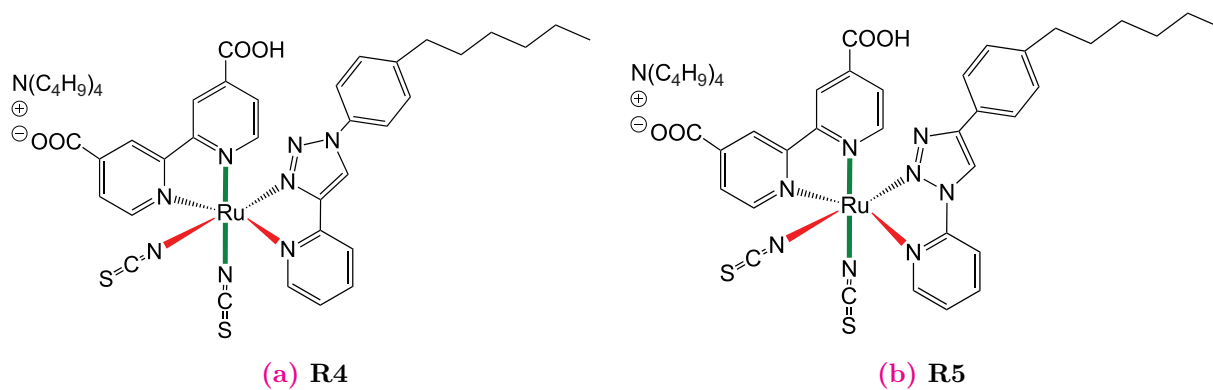

(a) **R4**

(b) **R5**

Figure A.6: Sensitizers functionalized with Triazole antennas as chelating ligands

List of Providers

Sensitizer	Provider name
N719 **Z907**	Laboratory of Photonics and Interfaces (LPI), EPFL, Switzerland
R1	Laboratory of Organometallic and Medicinal Chemistry (LCOM), EPFL, Switzerland
R2 **R3** **R4** **R5** **BTC-1** **BTC-2**	Institute of Organic Chemistry II and Advanced Materials, University of Ulm, Germany
B11 **B12** **B13** **B19**	Department of Chemistry, National Central University, Taiwan, ROC
C103	State Key Laboratory of Polymer Physics and Chemistry, Chinese Academy of Sciences, China

Appendix B

List of electrolytes

Code	Composition
Z959	1.0 M DMII, 0.1 M GNCS, 0.03 M I_2 and 0.5 M TBP in the mixed solvent of acetonitrile and valeronitrile (85/15, v/v)
Z960	1.0 M DMII, 0.1 M GNCS, 0.03 M I_2, 0.05 M LiI and 0.5 M TBP in the mixed solvent of acetonitrile and valeronitrile (85/15, v/v)
Z984	0.6 M DMII, 0.1 M GNCS, 0.03 M I_2, 0.05 M LiI and 0.5 M TBP in the mixed solvent of acetonitrile and valeronitrile (85/15, v/v)
Z946	1.0 M DMII, 0.1 M GNCS, 0.15 M I_2 and 0.5 M NBB in 3-methoxypropionitrile (MPN)
Z952	DMII/EMII/EMITCB/I_2/NBB/GNCS (molar ratio: 12/ 12/ 16/ 1.67/ 3.33/ 0.67)

Abbreviations

DMII	—	1,3-dimethylimidazolium iodide
EMII	—	1-ethyl-3-methylimidazolium iodide
EMTCB	—	1-ethyl-3-methylimidazolium tetracyanoborate
GNCS	—	guanidinium thiocyanate
TBP	—	*tert*-butylpyridine
NBB	—	*N*-butylbenzoimidazole

Acknowledgements

I wish to thank, in the first place, professor Michael Grätzel for giving me a great oppotunity to work on my thesis in LPI and for his support and guidance during my ph.d. study here. Special recognition is given to Dr. Shaik M. Zakeeruddin for preparation of dyes and electrolytes, for his valuable advices and discussions, for reviewing my works and for his kindness and patience. Without support and enthusiasm from these two, this work would not have been realized.

Great appreciation is extended to LPI staffs for their remarkable technical assistances; Dr. Robin Humphry-Baker for his numerous advices on photovoltaic and optical measurements; Dr. Thomas Möhl for his counsel on EIS measurement and its interpretation; Dr. Guido Rothenberger for sharing his exceptional knowledge on optical design of DSCs; Madame Cevey-Ha Ngoc-Le for her assistance on dye-loading experiments and Dr. Pascal Comte for preparing nanocrystalline films and for sharing his best-practice in doing so. Their expertise contributed greatly to this thesis. I am also immensely grateful to other LPI members, some of which I would like to mention here; Dr. Daibin Kuang for teaching me how to assembly the DSCs; Dr. Mingkui Wang who showed me how to make them efficient and being such a wonderful mentor, and Dr. Paul Liska for nice tricks on assembling a good DSC.

Special thanks are also due to a great help from Madame Ursula Gonthier for her administrative support – I would never forget the day she helped me out of my own apartment where I was locked in; Madame Paulou-Vaucher Pierrette from Photonics for all ph.d. program-related cooperations; Madame Francine A. Duriaux for her help on my french writings; and to all LPI colleagues who have made my life in LPI memorable; Ines Raabe – my former officemate, Supardi Sujito from electronical workshop, Magdalena, Aravind, Dr. Nok, Dr. Aswani, Qianli Chen (Lily) from EMPA, my dear friend Torben Däneke from Australia, . . . and all others. Everything we have done together during my

143

years in EPFL will always be remembered.

I owe a special thank to my sponsor, the OCSC from Thailand. I would have not been here in Switzerland without their support. To the staffs from the office of educational affairs in France for their supervision and consults, a sincere thank you.

Finally, I would like to express my gratitude to my family who supports me through thick and thin, with loves and affections. I want them to know that I love them cordially. I also thank my special thai friend, Pui, for her unlimited helps and companionships.

During my years in LPI, I have learned many things. They will always remain a big progression in my career. Apart from hardworking ambiance in EPFL, I enjoyed living in Lausanne with all those spring blossoms, summer rains, autumn leaves and winter snows. Switzerland is a land of dream, from which I could never wake up to forget...for all my life.

Lausanne, 13 Mars 2012   N. Pootrakulchote

Curriculum Vitae

Nuttapol POOTRAKULCHOTE
Nationality: Thai
Residence: Bangkok, Thailand

nuttapol.p@gmail.com

Education

Doctoral	Ph.D. Thesis, École Polytechnique Fédérale de Lausanne (EPFL), Switzerland Thesis title: Investigation on Functionalized Ruthenium-based Sensitizers to Enhance Performance and Robustness of Dye-sensitized Solar Cells
Master	M.Ch.E., Carnegie Mellon University, Pittsburgh, Pennsylvania, USA.
Bachelor	B.Sc., Chemical Technology, Chulalongkorn University, Bangkok, Thailand.

Working Experience

Engineer, Technical and research department, Thai Polyethylene Co., Ltd. Thailand

List of publications

1 *A new heteroleptic ruthenium sensitizer for transparent dye-sensitized solar cells.* Chia-Yuan Chen, Nuttapol Pootrakulchote, Min-Yu Chen, Thomas Moehl, Hui-Hsu Tsai, Shaik M. Zakeeruddin, Chun-Guey Wu and Michael Grätzel, in progress

2 *"Click-functionalized Ru(II)-complexes for dye-sensitized cells.* Ilona Stengel, Nuttapol Pootrakulchote, Pyan R. Dykeman, Amaresh Mishra, Shaik M. Zakeeruddin, Paul J. Dyson, Michael Grätzel and Peter Bäuerle, *Adv. Ener. Mater.*, in progress

3 *Ruthenium sensitizer with thienothiophene-linked carbazole antennas in conjunction with liquid electrolytes for dye-sensitized solar cells.* Chia-Yuan Chen, Nuttapol Pootrakulchote, Tzu-Hao Hung, Chun-Jui Tan, Hui-Hsu Tsai, Shaik M. Zakeeruddin, Chun-Guey Wu and Michael Grätzel, *J. Phys. Chem. C,* **2011**, *115*, 20043–20050

4 *"Click-chemistry" approach in the design of 1,2,3-triazolyl-pyridine ligands and their Ru(II)-complexes for dye-sensitized solar cells.* Ilona Stengel, Amaresh Mishra, Nuttapol Pootrakul-

chote, Soo-Jin Moon, Shaik M. Zakeeruddin, Michael Grätzel and Peter Bäuerle, *J. Mater. Chem.*, **2011**, *21*, 3726–3734

5 *A thiophene-based anchoring ligand and its heteroleptic Ru(II)-complex for efficient thin-film dye-sensitized solar cells.* Amaresh Mishra, Nuttapol Pootrakulchote, Mingkui Wang, Soo-Jin Moon, Shaik M. Zakeeruddin, Michael Grätzel and Peter Bäuerle, *Adv. Funct. Mater.*, **2011**, *21*, 963–970

6 *Molecular design of metal-free D-π-A substituted sensitizers for dye-sensitized solar cells.* L. Alibabaei, J.-H. Kim, M. Wang, Nuttapol Pootrakulchote, J. Teuscher, D. Di Censo, R. Humphry-Baker, J.-E. Moser, Y.-J. Yu, K.-Y. Kay, S. M. Zakeeruddin and M. Grätzel, *Energy Environ. Sci.*, **2010**, *3*, 1757–1764

7 *Design and synthesis of a novel anchoring ligand for highly efficient thin film dye-sensitized solar cells.* Amaresh Mishra, Nuttapol Pootrakulchote, Markus K. R. Fischer, Cedric Klein, Md. K. Nazeeruddin, Shaik M. Zakeeruddin, Peter Bäuerle and Michael Grätzel, *Chem. Commun.*, **2009**, 7146–7148

8 *New ruthenium sensitizer with carbazole antennas for efficient and stable thin-film dye-sensitized solar cells.* Chia-Yuan Chen, Nuttapol Pootrakulchote, Shi-Jhang Wu, Mingkui Wang, Jheng-Ying Li, Jia-Hung Tsai, Chun-Guey Wu, Shaik M. Zakeeruddin and Michael Grätzel, *J. Phys. Chem. C*, **2009**, *113* (48), 20752-20757

9 *Highly efficient light-harvesting ruthenium sensitizer for thin-film dye-sensitized solar cells.* Chia-Yuan Chen, Mingkui Wang, Jheng-Ying Li, Nuttapol Pootrakulchote, Leila Alibabaei, Cevey-ha Ngoc-le, Jean-David Decoppet, Jia-Hung Tsai, Carole Grätzel, Chun-Guey Wu, Shaik M. Zakeeruddin and Michael Grätzel, *ACS Nano,* **2009**, *3* (10), 3103–3109

10 *CoS supersedes Pt as efficient electocatalyst for triiodide reduction in dye-sensitized solar cells.* Mingkui Wang, Alina M. Anghel, Benoît Marsan, Ngoc-Le Cevey Ha, Nuttapol Pootrakulchote, Shaik M. Zakeeruddin and Michael Grätzel, *J. Am. Chem. Soc.*, **2009**, *131* (44), 15976–15977

11 *New efficiency records for stable dye-sensitized solar cells with low-volatility and ionic liquid electrolytes.* Dong Shi, Nuttapol Pootrakulchote, Renzhi Li, Jin Guo, Yuan Wang, Shaik M. Zakeeruddin, Michael Grätzel, and Peng Wang, *J. Phys. Chem. C,* **2008**, *112* (44), 17046–17050

12 *Energy-level and molecular engineering of organic d-π-A sensitizers in dye-sensitized solar cells.* Mingfei Xu, Renzhi Li, Nuttapol Pootrakulchote, Dong Shi, Jin Guo, Zhihui Yi, Shaik M. Zakeeruddin, Michael Grätzel, and Peng Wang, *J. Phys. Chem. C,* **2008**, *112* (49), 19770–19786

13 *New organic sensitizer for stable dye-sensitized solar cells with solvent-free ionic liquid electrolyte.* Dong Shi, Yiming Cao, Nuttapol Pootrakulchote, Zhihui Yi, Mingfei Xu, Shaik M. Zakeeruddin, Michael Grätzel, and Peng Wang, *J. Phys. Chem. C,* **2008**, *112* (44), 17478–17485